UNIVERSITY OF TRENTO

Dipartimento di Fisica

Light induced engrams in in-vitro neuronal cultures

DOCTORAL THESIS

Supervisor:

Prof. Lorenzo Pavesi

PhD candidate:

Clara Zaccaria

April 2022

Alla mia famiglia, perché le sfide sono motivo di crescita.

A Edoardo, perché è questione di priorità.
A Mattia, per essere sempre venuto in soccorso.
A Davide e Nicolò, per la condivisione di gioie e dolori.
A Beatrice, per le scadenze e i milioni di consigli.
Ad Asiye, per gli esperimenti fino a tarda sera.
Al Trento SPIE student chapter, per le tante avventure.

Contents

Chapter 1

Introduction

The human brain is made up of billions of interconnected neurons. Beside them, many other cells regulate the brain functionality, supporting neurons and regulating the signalling to many different parts of our bodies [1, 2]. In the last centuries, the research made a lot of progress in understanding the brain complexity, from the studies on neuronal communication to the implications of different processes in brain pathologies. Nevertheless, we still have to understand its behaviour, in order to unveil the mechanisms governing many of its functions. Many attempts were made to design and develop platforms able to record neuronal activity and/or interfere with it, exciting or inhibiting specific cells [3–9].
As what regards in-vivo studies on animals, in depth brain measurements must be performed via implantation of probes. These systems must satisfy several requirements such as small cross sectional dimensions in order to minimize tissue damage, thermal perturbations must be minimal for both tissue and animal safety, and spatial resolution should allow recording and interacting with specific neuronal assemblies [10]. Most of these problems can be overcome with the use of optical probes, taking advantage of a technique such as optogenetics, that makes the cells sensitive to light illumination. The use of fluorophores and genetically expressed indicators let the monitoring of brain activity with cell specificity, high spatial and temporal resolution. Year after year, these techniques have been improved to be compatible with in-vivo measurements, with high spatial resolution, and 3D simultaneous multi-site excitations and recordings can be performed [3–5, 10–20]. However, due to the complexity of an in-vivo brain, it is difficult to study the very elementary processes: these can be better investigated in simple 2D cultures in vitro, where the number and types of cells is under control.

Leveraging on the biological research in neuroscience, since the half of the XX, *artificial intelligence* went through a big development. This novel computation paradigm tries to mimic neurons and neuronal networks in order to create *intelligent* algorithm and/or devices able to solve tasks given some inputs. The name artificial intelligence is actually a rather vague term that accounts for "any device that perceives its environment and takes actions that maximize its

chance of successfully achieving its goals" [21]. Indeed, this discipline spans from the algorithms developed in the homonym branch of computer science and information technology, to the cerebral organoids recently developed in biotechnology. Artificial intelligence, beside its application in several fields relevant in human life (among others: automation, information search, document classification and analysis, commercial and financial transactions, military sector, machine translation, mobility, medicine, judicial sector, public administration, security, social behaviour, language... [22–24]), can be useful to understand how neuronal networks work and how still unknown biological processes occur [25–29]. Artificial neural networks can be developed in algorithms as well as in hardware devices, in which, after the training of the device, specific goals can be achieved.

Then, putting together the biological necessity of studying specific processes in vitro 2D cultures and the possibility to implement artificial neuronal networks in hardware devices, the ERC BACKUP project was conceived [30]. This interdisciplinary project started in 2019 at the University of Trento under the lead of Prof. Lorenzo Pavesi. It aims to create a hybrid platform in which biological neuronal networks communicate with artificial ones. The project is developed in two main branches: a computational and photonic part, in which physicists and computer scientists aim to develop novel artificial neural network architectures using integrated photonics; a biological part in which physicists, biologists and neuroscientists take advantage of photonic chips to optogenetically excite/inhibit neurons plated on the surface, in order to study biological processes such as memory formation or epilepsy. Eventually, if neurons are then plated on neuromorphic chips, with the support of an electronic circuitry, the artificial network could be trained to recognize specific signals coming from the biological network and decide how to act on inducing excitation or inhibition in specific locations. This hybrid platform could be then engineered to be used also in-vivo, to replace malfunctioning brain sectors or supporting specific areas in several diseases. This idea brings a novelty in the area of brain-machine interfaces: devices of this kind are already under development, but they mainly use electric stimulation/recording and the elaboration of the data is performed electronically and via software [7, 31–34]. The use of integrated photonics would bring speed, low power consumption and larger bandwidth in data collection and in the device response; moreover, using optogenetics, the device could interact specifically with the desired cells.

My PhD work was carried out within the BACKUP project, on the boundary between its two branches. More specifically, my goal was the development of a photonic platform able to optogenetically excite in-vitro neuronal cultures, in order to induce memory formation. I have worked along two directions: a) the design and characterization of a photonic chip for optogenetic applications; b) the setup of a light projector integrated to a confocal-super resolution microscope, able to optogenetically excite in-vitro neuronal cultures.

The thesis is organized as follows:
Chapter 1: Introduction. The contextualization of the thesis is presented, together with the aim of the work;
Chapter 2: Ethical implications. The ethical implications of the studies of neuronal network and the development of brain-machine interfaces are presented;
Chapter 3: Biological background. This chapter aims to present the biological framework in which this work was carried on: neuronal communication, memory formation and the main experimental techniques are illustrated;
Chapter 4: Photonic chip. In this chapter is presented the photonic chip realized for optogenetic excitation of neurons, from the design of the chip to its integration in a portable system for biological experiments;
Chapter 5: DLP. The second setup is presented: a digital light processing device (DLP) is integrated in a confocal-super resolution microscope. The system will be described, from the integration of the DLP in the microscope, its characterization, to its usage to induce neuronal excitation.
Chapter 6: Inducing in-vitro neuronal engrams. In this chapter, I will show the use of the DLP system to optogenetically induce an in-vitro memory. Data on successful strengthening of neuronal connections are presented.

The biological samples used in this work have been prepared by Beatrice Vignoli and Asiye Malkoç.

The BACKUP project received funding from the European Research Council (ERC) under the European Union's Horizon 2020 research and innovation programme (grant agreement No 788793).

Chapter 2

Ethical implications of AIs

The advent of artificial intelligence (AI) and especially its applications in diverse sectors of human life, has many implications in several fields, such as ethics, neurobiology, medicine, law study, sociology and philosophy [35]. Starting from the awareness that it is nowadays an interdisciplinary matter, a workshop on the issues raised by the use and the implementation of artificial intelligence and its applications took place in December 2020. Organizers were the ERC-AdG Backup Project [30] and the BioLaw Project [36] of the University of Trento, and the Bruno Kessler Center in Information and Communication Technology (FBK-ICT Center) [37]. During this workshop, titled "Neuroni artificiali e biologici: etica e diritto" many implications of AI were presented from a physical, juridical, philosophical, ethical, and sociological point of view, underlying challenges and opportunities in these new technologies. Since I participated in the writing of a white paper on the outcomes of the workshop discussion [38], I will present here my personal view of the problem.

The development of AI algorithms started in the second half of the 20th century and includes many different techniques. Among others, a specific approach in *machine learning*, namely *deep learning*, achieved much success thanks to the exponential increase of computational power. These algorithms train themselves to process data, learn from them, gaining accuracy and capabilities. Deep learning algorithms are based on artificial neural networks, which are ensembles of nodes, arranged in different ways, which imitate the behaviour of biological neurons. As in the human brain, an input is processed to give an output. This output can then be compared with the expected one and by iterative processing the network can be trained to work correctly. However, these processes are usually not funded on causality, rather than on statistical correlation models, whose logic and working mechanisms can not be fully explained: this is why they are often regarded as *black boxes*. Moreover, these algorithms can sometimes be affected by a biased training that can lead to systematic errors and prejudices when used in decision procedures [39]. These algorithms are nowadays coming out from the scientific laboratories where they were developed and are more and more present in our everyday life. Among the problem of biases, also social problems must be considered: there is the risk

that just the companies that can have access to the big resources can develop AIs and benefit from them, exacerbating the inequalities already existing in our society. This discrimination would be even more important when dealing with medical applications of AI: just the richest could afford AI devices. Moreover, in the case of automation, for example in transport, or, even worse, in military applications, who has the responsibility over their possible errors? Do AIs devices have a juridical identity? To overcome all these social problems, a proper regulation is needed: much has already been done at the European and international level, but finding the right way to regulate all the social and juridical aspects involved in AIs, is difficult to find [38]. Most of the time, case by case must be considered for proper regulation. Then comes also the ethical and philosophical problems: are AIs used just for medical treatments, or also for human enhancement? Do we have to find a new definition of a human being? If we have artificial neurons, can we still consider ourselves "free" in "our" decisions and thoughts? Can one day cerebral organoids develop real intelligence and must they be subject to rigorous oversight? [40, 41]

These problems are just some of many, but they give an overview on how complicated and delicate is talking about AIs in our society. Often all these problems hide all the advantages that AIs can bring. First of all, improvements that AIs are bringing in scientific research are undeniable. Just to mention some examples, recently, using machine learning it was developed a new program by Deep Mind, AlphaFold2, which is able to predict the folded structures of proteins [26–28]; in 2013, lab grown cerebral organoids were developed, which can resemble real brain structures, opening an incredible prospective for the study of many brain related pathologies [29]. Moreover, brain-machine interfaces using AI algorithms can help in many diseases and disabilities [7, 31]. It is well known that algorithms can compute better than humans in specific tasks: for example, automation in transports can decrease the number of accidents caused by human distraction. The fear of a dominance of machines over humans is still science fiction, and neural networks and organoids are far to develop a self awareness, since it is not already known what consciousness is. Despite all these advantages, people are still cautious and skeptical about dealing with AI.

This scepticism can be overcome, if a proper education on AIs and their functioning is given to people: this is the crucial aspect that must be considered, to deal with present and future challenges. As well presented in chapter "*Availability, Emotion, and Risk*" of Kahneman's "Thinking, Fast and Slow" [42], people make judgments just by their emotions, ignoring many logic and statistics that could lead to more objective answers to specific questions. So, how to find an agreement between the public and the experts about such delicate topics as AIs? Kahneman, citing the psychologist Paul Slovic, proposes an interesting approach: "*When experts and the public disagree on their priorities*, he says, *Each side must respect the insights and intelligence of the other*". Indeed, scientists must consider that we are not living in an *unthinking society* and that people's concerns about certain applications may involve aspects that scientists did not think about. It is then very important that experts, companies, and the population can discuss together in order to find a

proper regulation of new technologies. Actually, despite the interdisciplinary nature of these technologies, there is a lack of understanding also between the different actors. Thus, it is of primary importance to create a dialogue first of all at the academic level. Science can be divided in disciplines, but in the real world this division does not exist: interdisciplinary approaches are really important to identify and formulate correctly the problems to face. In parallel, a first approach to computer science and AIs must be introduced since school, because ignorance on how new technologies work can lead to problems, fear and also dangers in everyday life. Indeed, the debate between the public and experts is useless if there is not a clear definition and knowledge of the concepts involved. A real awareness of AIs can lead to a more conscious use of these new technologies, with all the benefits that they can bring to society. The involvement of all the parts can bring to a new ethical approach, more inclusive, contextual, and creative.

Therefore, the research here discussed has to be disclosed to the general public in advance, as we did in a short video [43].

Chapter 3

Biological background

3.1 Neurons and synaptic communication

The nervous system of our body is made up of trillions of cells that are strongly interconnected and control different parts of our bodies [1, 2]. For the sake of this work, let's focus on the central nervous system, and on the functions and characteristics useful to understand this research.
Since the Nobel prize won in 1906 by Golgi and Ramòn y Cajal, the brain has been thoroughly studied in its structure and physiology. The brain is mainly formed by two kinds of cells: neurons, which are the essential units for the signal transmission, and *glia*, an ensemble of many different cells that support neurons in different ways. There are many kinds of neurons, with different structures and roles. They are generally formed by a cell body and many processes that branch out from it, named dendrites and axons (figure 3.1). Dendrites are responsible for receiving information by other neurons and, on their surfaces, present some small protuberances, called *spines*, whose characteristics depend on the age of the neurons and on the signals received by the cell [44–48]. Axons are instead responsible for the transmission of the signals to other neurons.
Across the membrane are located the so-called ionic channels, which are made of different proteins that make the channel selective for specific ions, with different permeabilities. The flux of ions through these channels changes the voltage between the inner and the outer part of the cell. This membrane potential in a non excited cell is called *resting potential* and is set at -70mV. The value of the membrane potential depends on the gradient of ions concentration inside and outside the membrane, which is affected by the different permeability of ionic channels to the potassium (K^+), sodium (Na^+), and chloride (Cl^-) ions, as described by the Goldman-Hodgkin-Katz voltage equation [1, 2]. A change in ions concentration induces a variation of the membrane potential, i.e. an electrical signal. This signal can be weak and propagate only for a short distance. In this case, we talk about *graded potentials*. When more graded potentials sum together and reach the *trigger zone* of the neuron - a region located in the first part of the axon, rich of Na^+ channels -, an *action potential* can occur.
A change in membrane polarization is called depolarization, if the voltage difference decreases, or hyperpolarization, if the voltage difference increases. Depo-

larization typically occurs in excitatory neurons, while hyperpolarization occurs in inhibitory ones. Action potentials are big and fast depolarizations of the cell membrane that propagate for long distances and bring signals between neurons. When graded potentials sum up in the trigger zone to a threshold level of -55 mV, Na^+ channels open and a flux of positive ions enters the cell trying to reach the equilibrium potential for Na^+ ions, which is +60 mV. But as soon as the potential becomes positive, also K^+ channels start to open in order to balance the internal flux of positive ions with the emission of K^+ ions. Since K^+ channels have a slower kinetic compared to Na^+ ones, the maximum permeability to K^+ is reached when Na^+ channels have already started to close, after a peak of +30 mV. While K^+ channels remain open, the voltage keeps becoming more and more negative, going beyond the resting potential, down to -90 mV. This hyperpolarization is called *undershoot*. Eventually, K^+ channels start to close and the potential returns to the resting value of -70 mV (Figure 3.1). The overall process takes some milliseconds. The amount of time in which Na^+ channels are closed, is called *refractory period*, in which another action potential can not be induced in the cell: this ensures that an action potential in a cell can not occur until the previous one is not ended.
The signals coming from other neurons arrive in dendrites, are elaborated in the cell body and, if an action potential occurs, a new signal propagates along the axon. Indeed, the axon is rich in Na^+ channels that open gradually starting from the first part of the axon, down to the final parts, due to the local currents of Na^+ ions caused by action potential, as described before. Axons are enveloped in the Schwann cells, which are 1-1,5 mm long; the interstices between these cells, named Ranvier's nodes, allow the communication with the extracellular medium, and, thus, the flux of ions through the axon's membrane. Schwann cells work like insulators along the axons, speeding up signal transmission.

The end parts of the axons, where the information passes from one cell to another, are called synapses. The cell that brings the signal is called pre-synaptic, while the one that receives it is called post-synaptic. In between pre and post synaptic regions there is the so-called *synaptic cleft*. There are two main kinds of synapses: the electrical one, in which the signal passes along the synapse through junctions, and the chemical one, in which substances are released by the pre-synaptic cell in response to depolarization and bind to specific post-synaptic receptors.
In order to be able to study memory formation, let's focus then on the general mechanisms of chemical synapses. This kind of synapses are structurally recognisable because they release *synaptic vesicles*, which contain neurotransmitters, located near the membrane. When an action potential induces depolarization on the presynaptic element, local calcium ionic membrane channels are forced to open and the following increase of Ca^{2+} concentration induces the opening of synaptic vesicles and the release of neurotransmitters in the synaptic cleft (Fig. 3.2). Neurotransmitters spread in the synaptic cleft and reach the postsynaptic membrane, where they can bind to different kinds of receptors. These can be classified in two categories: *ligand-gated ion channels*, when the binding to the neurotransmitter induces its opening and, thus, the beginning of a postsynaptic electrical response; *metabotropic receptors*, when binding induces other molecular events that can indirectly modify the status of other ionic channels on the

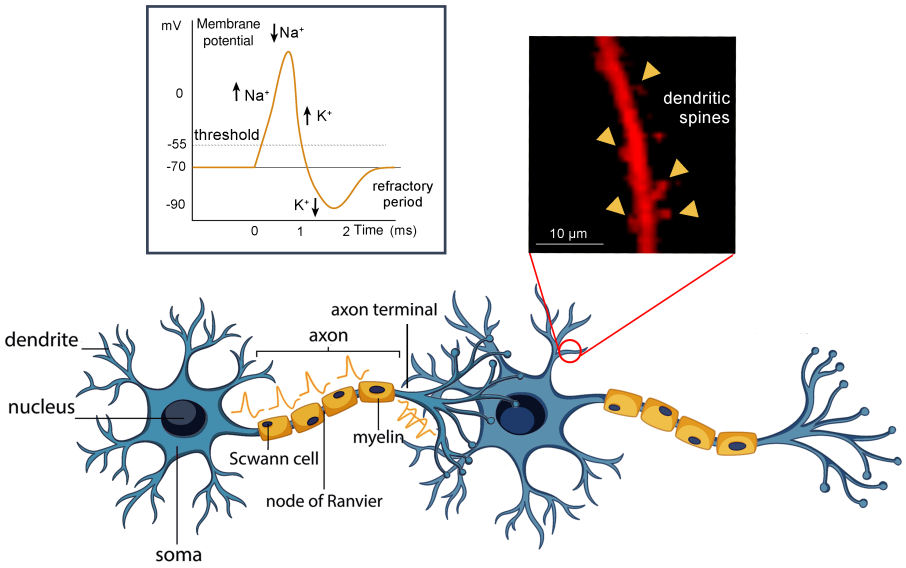

Figure 3.1: **Neuronal communication.** The sketch summarizes the main morphological parts of neurons. The insets show an action potential (with arrows indicating the opening and closing of channels), and an image of dendritic spines taken with a confocal microscope. The images of neurons were taken from [49].

postsynaptic membrane. In any case, in both cases, an ionic current will be generated on the postsynaptic membrane, and thus a postsynaptic potential - excitatory on inhibitory - can occur. Neurotransmitters that are floating in the gap either are quickly picked up again from the presynaptic part, thanks to specific membrane carriers, or become inactive thanks to specific extracellular enzymes. In this way, the communication between the synapses ends.
The peculiarity of synapses is that they can change their functional, molecular and structural properties depending on their previous activity: this process is called *synaptic plasticity*. When many graded potentials arrive with high frequency (20-50 Hz) one after the other (*tetanic stimulus*), their sum can go over the threshold and start an action potential which will be more intense, the more the input signals. The release of neurotransmitters is proportional to the intensity of the action potential and to the subsequent increase of Ca^{2+} concentration in the pre synaptic compartment. This fast release of neurotransmitters is then limited by the availability of vesicles. If after a short amount of time another stimulus arrives to the synapse, it will evoke a bigger response to the stimulus compared to the situation before the tetanic stimulus, because the recent amount of Ca^{2+} facilitated the machinery involved in the carriage and release of vesicles. The process just described is called *neural facilitation* and lasts for seconds to minutes. If synaptic activity keeps going, changes in the postsynaptic compartment can occur, leading to the so call *Long Term Potentiation* (LTP). In this case, glutamate neurotransmitter is involved. Glutamate has two main postsynaptic receptors called AMPA and NMDA. The latter receptor is a ligand-gated ion channel that opens when bind to glutamate, but at resting potential it is also blocked by a Mg^{2+} ion that obstructs the channel. This ion

can be expelled only by depolarization. When the presynaptic compartment releases glutamate, the neurotransmitter binds to AMPA receptors, which act like Na^+ ionic channels, and to NMDA receptors. The flux of Na^+ depolarizes the cell and let the expulsion of Mg^{2+} ion from NMDA receptors, which open and let the entrance of Ca^{2+}. These ions activate secondary processes in the cell that result in structural changes in AMPA receptors, an increase in their conductance, an increase of AMPA amount in post synaptic membrane and the proteic synteses of new ones (Fig. 3.2). After a tetanic stimulus, if proteic synthesis occurs, synaptic potentiation continues for hours and days.
If instead, a lower frequency stimulus continues for tens of minutes, Long Term Depression (LTD) can occur: this happens when the concentration of Ca^{2+} is so low that the opposite mechanisms are activated and the number of AMPA receptors decreases.

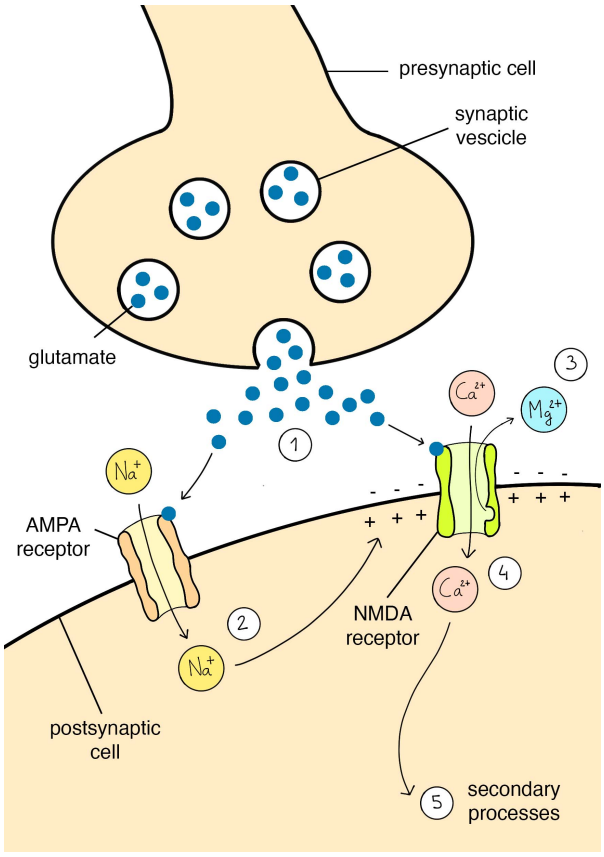

Figure 3.2: **Synaptic communication and LTP.** An action potential on the presynaptic cell stimulates the release of the neurotransmitters in the synaptic cleft by the synaptic vescicles. In the case of long term potential, the involved neurotransmitter is glutamate (1). It can bind to AMPA and NMDA receptors on the postsynaptic membrane. (2) The binding with glutamate induces AMPA receptor opening and a flux of Na^+ occurs. The following depolarization of the cell led to the opening of the NMDA receptor with the release of the Mg^{2+} (3) and the influx of Ca^{2+} (4). The increase of calcium concentration in the cell activates some secondary processes that lead to changes in the postsynaptic cell.

3.2 Experimental methods for interacting with neurons

Several techniques were developed through the years to induce and/or measure neuronal activity. These techniques can be gathered in three main categories: electrophysiology, pharmacology and optical.
The first one exploits the cell electrical potential. By using electrodes in contact with the culture, it electrically excites neurons and/or measures their activity. One electrode is brought into contact with the cell to be measured, while a second one is kept in the surrounding of the cell as reference ground [2]. This technique, called *patch clamp*, makes it possible to measure temporal voltage or current changes in the sample. These measurements can be performed both in in-vitro cultures and in in-vivo experiments. However, this method of interaction with neurons often lacks spatial resolution, direct contact with the cell is needed and is exposed to artifacts [50–52].
The second method is based on the use of suitable drugs to influence the neurons activity. The main counterpart is that sometimes they act on different types of cells indiscriminately and, therefore, are not cell-specific neither have any sort of spatial resolution.
In the case of optical methods, different techniques were implemented to interact with neurons [53]: in 1970s it was developed a technique based on voltage-sensitive organic molecules. They are introduced in neuronal membranes and are coupled to fluorophores whose signal depends on the voltage through the membrane. These molecules can be externally applied or genetically inserted in cells [54–57]. Beside voltage sensitive dyes, a variety of other fluorescent indicators were developed to detect the variation of concentration of intracellular specific ions, like sodium, chloride and calcium or pH variations. Calcium indicators, in particular, are widely used in neurobiological research [58–61]. All these fluorescent indicators went beyond toxicity and cell-specificity problems with the introduction of fluorescent proteins (FPs) that can be genetically expressed by cells, both in in-vitro and in in-vivo experiments. These proteins can change fluorescence intensity following a conformational change, or even spectral properties, using Förster resonance energy transfer (FRET) between two FP variants.
The optical reporters described so far enable the recording of neuronal signals. In 2005 was introduced a new technique, named *optogenetics*, that makes possible to excite or inhibit neurons using light. It is minimally invasive, with both high spatial and temporal resolution, as well as with high cell specificity [62–65]. This technique consists in the transfection (i.e. nucleofection) or infection (via viral vectors) of neurons with membrane proteins called *channelrhodopsins* (ChRs). These are a family of seven-transmembrane, light-responsive proteins that are composed by a protein called *opsin* bounded to a photosensible molecule called *retinal*. These special proteins are encoded by opsin genes found in prokaryotes, algae and fungi. Upon photon absorption, the retinal photoisomerizes from an all-*trans* configuration to the 13-*cis* configuration. After the stimulus the retinal thermally returns to the all-*trans* state [51,53]. This isomerization of the retinal triggers a sequence of conformational changes of the opsin, collectively referred as photocycle. Each channelrhodopsin is characterized by a specific photocycle, and different light temporal patterns can induce different

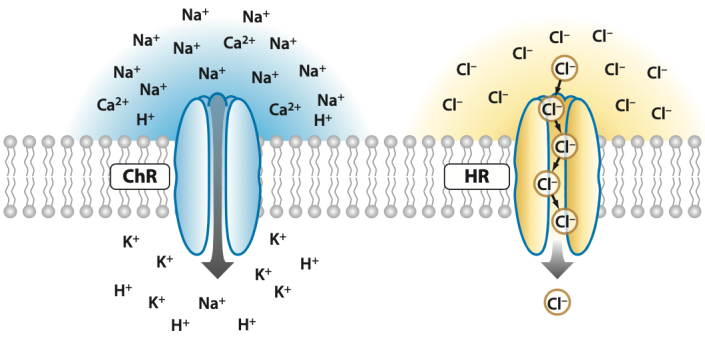

Figure 3.3: **Two optogenetic tools.** Channelrhodopsins conduct cations and depolarize neurons upon illumination (left); Halorhodopsins conduct chloride ions into the cytoplasm upon yellow light illumination (right). Reprinted by permission from Marketplace^{TM}: Annual Reviews, Inc., Annual review of neuroscience [51]; permission conveyed through Copyright Clearance Center, Inc."

effects on the protein response and on the illuminated cell [66–71, 71–73]. Moreover, proper light intensities are required to not induce phototoxicity: this aspect depends on the specific experimental setup and sample in study [67, 74, 75]. Channelrhodopsins act like ionic channels in the neuronal membrane: upon absorption of photons, the channel opens and lets fluxes of ions that can iper or depolarize the cell, inducing respectively excitation or inhibition of the neuron. Generally photosensitive proteins that induce activity inhibition are named Halorodhopsins (HR) (Fig. 3.3). Nowadays a lot of channelrhodopsin have been engineered with different use, spectral properties, photocycle topology, ion selectivity and kinetic time constants [76, 77]. The first one to be implemented in neurons were channerhodopsin-1 and 2 (ChR1, ChR2) that can be activated with blue light, but a big list of ChRs have been implemented with operating wavelength up to 700 nm with different kinetic constants. [51, 65, 78–82]. Channelrhodopsins can be used in in-vivo or in in-vitro systems and in combination with different fluorescent reporters of neuronal activity [51, 67, 83–93].

3.3 Memory

Memory is the ability of the brain to get, store and recover information from experience [94]. In 1904, the zoologist Richard Semon first identified memory as the encoding of information in *engrams*, defined as a simultaneous complex of excitations that induce changes in the brain [94–96]. In 1949 the psychologist Donald O. Hebb proposed that memory is the result of the strengthening of synapses between neurons that were simultaneously excited [94, 96, 97]. These neurons form, then, a cell assembly that can be considered as the neural substrate for the engram [94]. We can define engram as an ensemble of activated cells, molecularly or structurally modified by an experience; moreover, engram cells can be reactivated by subsequent presentation of the same excitation stimulus [96] (Fig. 3.4).

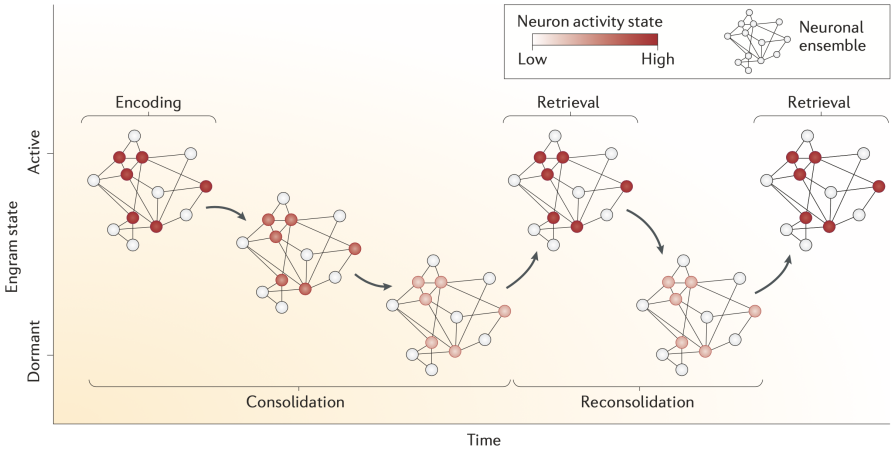

Figure 3.4: **Formation of an engram.** The formation of an engram consists in the strengthening of connections between collections of neurons that are active (red) during an event. Consolidation further strengthens the connections between these neurons, a phase in which the engram enters a mainly dormant state. Memory retrieval returns the engram back to an active state. If consolidation is not performed, engram connections are lost and amnesia occurs. Reprinted by permission from Springer Nature: Nature Reviews Neuroscience, [94]; permission conveyed through Copyright Clearance Center, Inc."

Engrams can be conceived and studied at different scales and levels of analysis. Considering the whole brain, several brain regions can be involved in the same engram [98]. Going down to neuronal level, we can consider the cells with strengthened connections as part of an engram. However, these changes involved in neurons are synapses related, so we can even talk about a synaptic engram. Eventually, changes also occur at nuclear levels, with transcriptional and epigenetic changes [94, 96, 98, 99]. In the last decades, several studies were performed at all these levels, from behavioural experiments to neuronal firing and synaptic transmission, taking advantage of new experimental techniques. Moreover, it was found that memory is not related only to neurons, but it must be considered that also glia cells play an important role in memory formation, supporting neurons with specific production of neuroactive molecules (termed *gliotransmitters*) [100, 101].
Focusing on the cellular level, let's define what is known about neuronal and synaptic engrams. Decades after Hebb's studies, empirical studies showed that learning and long term potentiation alter spine morphology: as already explained in section 3.1, long term potentiation increases the intracellular Ca^{2+} concentration thanks to NMDA receptors, and an increase in number and conductance of AMPA receptors follows. After learning, it was also observed an increase in synaptic dimensions and number [102–105]. In a second phase, hours after the first stimulations, the structural changes in synapses are maintained by protein synthesis of AMPA receptors [99, 106–109]. All these aspects were investigated thanks to advanced microscopy techniques, measurements and pharmacological or molecular manipulation. Recently, techniques like immediate early gene (IEG) labeling and optogenetics let the tagging and further study

of engram cells. IEGs, like *c-fos* and *arc* are produced during neuronal activity and can then be used as markers of excited cells [110]. For example, IEGs can be used with Tetracycline (Tet) technology: Tet-controlled transcriptional activation is a method of inducible gene expression in which transcription can be turned on or off in presence of antibiotics like tetracycline or doxycycline. So, combining this technology with IEGs promoters, activated neurons can be tagged with temporal specificity given by the presence or absence of antibiotic [111, 112]. If these neurons are then equipped also with channelrhodopsins [113], they can be specifically reactivated after learning, studying memory retrieval. Tagging specifically learning-activated cells enables the discrimination between engram and non engram-cells, and to study their differences in signals amplitude, AMPA receptors, and dendritic spine density. In this way, the correlation between LTP induction and memory was definitively confirmed and was demonstrated that the reactivation of engram cells induces memory recall [8,9,111,114–117]. These techniques are getting more and more specific, for example *SynActive* (SA) strategy permits the expression of proteins specifically in potentiated synapses: Channelrhodopsin-SA allows the expression of opsins in engram-specific synapses, opening the doors to new experiments about the study of synaptic engrams [118]. These techniques helped to find many molecular and structural processes involved in memory formation.
However, how cells and synapses are recruited in engrams, and which are the mechanisms underlying information storing, has not yet been unveiled. Indeed, there is evidence that these mechanisms are not random, but coincides with the expression of molecules, such cFos and Arc, and transcription factors such as *CREB* [119, 120].
If we consider that memory is stored in synapses rather than in neurons, single neurons can participate in many memory engrams. Also in this case, the enrolment of synapses in engrams seems not to be random. For example, if a synapse is potentiated, the probability of potentiation of nearby synapses (within 10 μm) is higher than in more far ones; this happens because some molecules expressed in the potentiated synapse reach also nearby ones. These and other processes lead to the formation of a specific engram and play a role in network formation and remodelling. All these aspects have been studied in vivo, in different brain sectors, by considering a high number of different neurons that communicate through different brain areas [117, 121].
However, to study these processes at a more basic level, a bottom-up approach is needed. If we start from a small neuronal network, we can study and manipulate them with ease. Therefore, in this thesis I propose the realization of two experimental set-up to create memory in simple 2D in-vitro neuronal cultures, exciting and inhibiting neurons. These kinds of systems can be useful to study the processes involved in the enrolment of specific synapses in engrams, the role of neurons as nodes in multiple memories and the role played by glia cells in memory formation [100, 101].

3.4 Hybrid neural interfaces

In order to study the brain and the related neuronal network activities, many attempts were made to design and develop platforms able to induce and record neuronal activity [3–9]. We can refer to these technologies as *hybrid neural inter-*

faces. For in-vivo applications, in depth brain measurements must be performed via implantation of probes: these systems must satisfy several requirements such as small cross sectional dimensions in order to minimize tissue damage, thermal perturbations must be minimized for both tissue and system safety, and spatial resolution is fundamental to record and interact with specific neuronal assemblies [10]. By using both electrical excitations and recordings through electrodes implantations, as well as optogenetics, many different hybrid neural interfaces were developed to implement probes that perform optical excitation of neurons and simultaneous electrical recording [4, 5, 10, 12, 14, 17, 18]. Nowadays 3D simultaneous multi-site excitations and recordings are possible [3, 5, 7, 10, 11, 13–16, 18–20]. In these studies, the optical excitation of neurons is performed with optical fibers, or with probes with integrated μLEDs arrays and diffractive gratings. These probes enable the study of many brain functions associated, for example, to behavioural experiments or brain diseases [7].
Despite these advancements, there are many biological processes, like memory formation or network behaviours, that still need studies at a more elementary level. For this, a different kind of hybrid neural interface must be implemented. It should be able to illuminate single neurons (or even specific parts of them) in 2D neuronal cultures, and read their responses, in an electrophysiological or optical way. In this thesis, I will focus on two main approaches of light illumination: a 2D culture can be illuminated either using light coming from the microscopes, using external and bulky - but tested, reliable and versatile - technologies like spatial light modulators (SLM), digital light projectors (DLP) or micro LED arrays systems [6,122–124], or implementing new compact platforms in which neurons are directly in contact with the illumination platform, that can be for example a photonic chip or LED arrays [92,125]. In the latter system, the excitation platform can also be an electrode matrix (Micro Electrode Arrays, MEA) [93]. In both systems, the reading of neuronal responses can then be performed using electrophysiology and/or fluorescent indicators.
MEA chips are the more widely used platforms to electrically excite and record neuronal network activity, and many efforts were made to make these platforms efficient to study electrical neuronal culture signals [126–131]. Nevertheless, MEA systems have one main drawback, which is spatial resolution: when a neuronal culture is plated on the surface of a MEA chip, the electrodes will detect changes in the electric field that come from the responses of multiple cells around the same electrodes. Nanotechnology in principle allows the production of small electrodes, but the size is mainly limited by the noise of the system during the reading of signals and charge capacitance at the interface during excitation. For these reasons, the minimum electrode diameter is typically 10 μm, which is about the size of the neuronal body. Moreover, these systems have limitations like unpredictable current pathways, electrical artefacts, non-cell-specificity, and often, due to electrical artefacts, it is not possible to record signals from the same electrode used for stimulation. In contrast, the integration of optical stimulation sites in these systems can bring a gain in cell specificity, spatial resolution and simultaneous excitation and recording. Some attempts were made in this direction: I will focus on two examples given by [125] and [92]. In [125], Yakushenko et al. propose a device composed of an array of InGaN light-emitting diodes coupled with a custom made microelectrode array. LED emitters create on the surface of the chip a spot of about 30-40 μm. Although small μLEDs can be realized [132,133], the main drawback is that LEDs

require electrical alimentation, which makes the system bulky, and potentially hot. Moreover, the system sensed electrical artifacts due to light crosstalk. All these aspects were solved by Welkenhuysen et al. [92]. In this case, the system consists of a photonic chip with periodic grating emitters, with an integrated MEA (a system called *multi electrode optrode array* (MEOA) by the authors). In this case, the recording electrodes are placed in the same plane of the light emitters, one near the other, in order to avoid light artefacts. Moreover, light coming from gratings is directional and confined, ensuring that electrodes are not exposed to light. Starting from this idea, in this work I will present the design of a photonic chip with aperiodic gratings able to focalize and shape light in a specific plane. Moreover, I will also present a DLP system implemented on a confocal and super resolution microscope set-up. These systems were designed and tested to form engrams formation and to study memory. However, these platforms are extremely versatile and can be used to study different brain functions and pathologies, among which memory and amnesia are just two examples.

Chapter 4

Photonic chip

4.1 Integrated optics and waveguide propagation

Since its first conception in the 1960s, integrated optics went through a big development as an alternative to open space optics and conventional electrical integrated circuits. Integrated optics consist of miniaturized optical integrated circuits realized with different materials. The main advantages of integrated photonic circuits compared to electronic ones are the low power consumption, small size, light weight, and the possibility to use different wavelengths. In addition, in silicon platforms, they can be realized with the same fabrication methods of electronic circuits, which integrated photonics CMOS compatible.
Light in a photonic circuit travels inside the *waveguides*, which are channels of a core material with a high refractive index, embedded in an outer material with a lower refractive index which we will refer as *cladding*. In fact, if we consider a ray-optic description of the system, if the light enters the waveguide with an angle higher than the critical one, it will be confined in the waveguide for total internal reflections at the interface between the core layer and the cladding one. Depending on the core and cladding materials, on the geometry and on the used wavelength, light travels inside the waveguide in many different distinct optical modes i.e. in different spatial distribution of the optical energy, as shown in figure 4.1 [134]. These optical modes are the solutions of the Maxwell's wave equation

$$\nabla^2 \vec{E}(\vec{r},t) = [n^2(\vec{r})/c^2]\partial^2 \vec{E}(\vec{r},t)/\partial t^2 \tag{4.1}$$

considering a monochromatic wave

$$\vec{E}(\vec{r},t) = \vec{E}(\vec{r})e^{i\omega t}, \tag{4.2}$$

where $\vec{E}$ is the electric field vector, $\vec{r}$ is the radius vector, $n(\vec{r})$ is the index of refraction, c is the speed of light and ω the angular frequency. Substituting 4.2 in 4.1 one gets

$$\nabla^2 \vec{E}(\vec{r}) + k^2 n^2(\vec{r})\vec{E}(\vec{r}) = 0, \tag{4.3}$$

with $k \equiv \omega/c$. Considering an infinite waveguide in the y direction and an uniform plane wave propagating in the z direction

$$\vec{E}(\vec{r}) = \vec{E}(x,y)e^{-i\beta z}, \tag{4.4}$$

with β a propagation constant, the solutions of 4.3, with appropriate boundary conditions at interfaces (continuity of $E(x, y)$ and $\partial E/\partial x$), are discrete sinusoidal functions of x, in the core, which decay exponentially in the cladding. These solutions are the supported modes of the waveguide [134].
As can be seen in (4.4), the electric field depends on the (x, y, z) coordinates. Generally, TE or TM linearly polarized light are used: in TE polarization the electric field (E) exists only along the yz plane, while the magnetic field (H) is in the orthogonal plane. On the contrary, the TM is characterized by the electrical field only in the xz plane. The z axis indicates the propagation direction (figure 4.1).

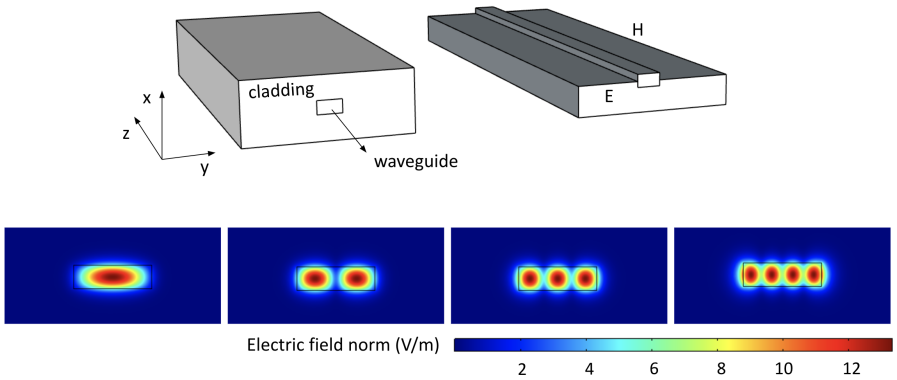

Figure 4.1: **Light propagation inside a waveguide.** In the upper drawings are represented a channel waveguide, and the exploded system with the waveguide exposed and the electromagnetic field represented in TE mode. In the bottom part are represented the first 4 modes guided by the simulated waveguide.

4.1.1 Photonic simulators

In order to design photonic circuits, methods, like FDTD (finite difference time domain) and FEM (finite element method) methods, solve exactly the wave equation through a discretization of the time domain and limiting the number of term in series expansions [135]. Beam propagation methods (BPM) assume slowly varying fields along the propagation direction, reducing the problem from second order derivative equations to first order ones. These methods require a lot computation effort and are thus quite slow for the design processes that require a large number of iterations. Some alternative and faster methods have been proposed, like a fully vectorial eigenmodes expansion and propagation tool (CAMFR, CAvity Modelling FRamework) [136, 137].
For the design of the gratings in our photonic chip, we proposed an implementation of FEM simulation with a Transfer Matrix approach, with the result of a fast and reliable computational method. This *FEM enhanced transfer matrix method* will be described in section 4.2.

4.1.2 Fiber to chip coupling

To input or to collect light signal from a photonic circuit, coupling devices are needed. These can be classified in two main types: in-plane coupling or out of

plain coupling. In-plane coupling is mostly achieved by the focusing of a beam into the waveguide core. The coupling is then accomplished by matching the input beam field and the waveguide modes that can be quantified by computing the overlap integral between the two fields. This coupling is named *butt coupling* and is usually achieved with tapered and lensed fibers with a focus diameter that is as close as possible to the cross section of the waveguide. The out of plane coupling consists in the injection or extraction of the light in the waveguide from its surface. It can be performed using external devices, like prism couplers, or integrated structures like grating couplers [134]. In both cases, the phase velocities in the z direction of both the input beam and the optical mode in the waveguide must be the same. In particular, referring to the system depicted in figure 4.2(a), the following equation must be satisfied:

$$\beta_m = kn_1 sin\theta_m = \frac{2\pi}{\lambda_0} n_1 sin\theta_m, \tag{4.5}$$

where β_m is the propagation constant, k the wave vector of the input beam, n_1 is the cladding refractive index, λ_0 the light wavelength, and θ the angle of incidence of the beam [134].
However, from the solutions of equation (4.3), it can be seen that modes will be supported by the waveguide only if $\beta > kn_1$. This, together with (4.5), would bring to $sin\theta_m > 1$, which is impossible. The prism or the grating coupler solves this in two different ways. If a beam is directed on the face of a prism with $n_p > n_1$, total internal reflection will occur at the n_p-n_1 boundary (being n_p the prism refractive index); if the distance between the prism and the waveguide surface is sufficiently small, the evanescent waves from the prism can overlap with the evanescent modes of the waveguides and coupling can occur (figure 4.2(b)).
Grating couplers instead consist tipically in a periodic corrugation of the waveguide surface which adds to the modes of the waveguide a set of spatial harmonics such that the propagation constant becomes

$$\beta_\nu = \beta_m + \frac{2\pi\nu}{\Lambda}, \tag{4.6}$$

with ν being 0,$\pm$ 1, $\pm$ 2... and Λ the period of the waveguide corrugation (figure 4.2(c)). Now, thanks to the negative values of ν, the coupling condition (4.5) can be satisfied [134]. Then, the field coupled to these harmonics will turn into one of the waveguide modes after the grating region. By reciprocity, the grating can be used also to output a signal at the specific angle θ_m. The effect of a grating on a propagating mode inside a waveguide can be described also considering each perturbation as a diffractive element that impacts on the mode by reflecting, transmitting and scattering away the light. The light scattered by all the elements of the gratings can interfere in different directions according to the geometric characteristics of the grating (that can also be non periodic). Thus, light can be coupled to a fiber if the grating is such that the overlap of the total scattered field and the fiber mode is maximized. This way to describe grating behaviour is further analysed in section 4.2.1 and in [138].

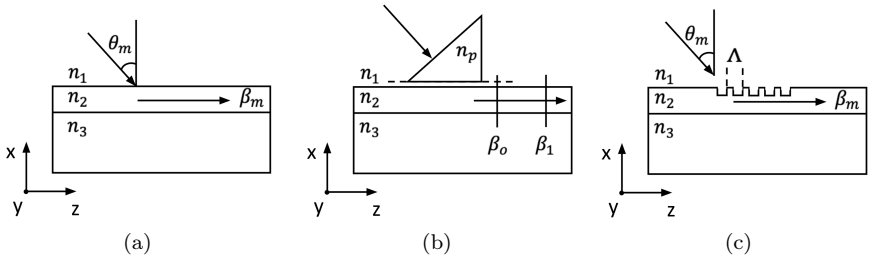

Figure 4.2: **Out of plane coupling.** The skatches represent the bare system (a), the functioning of prism couplers (b) and grating couplers (c). The arrow coming from the top left represents the input beam to be coupled into the waveguide.

4.2 Design of the photonic chip

As mentioned in section 3.4, in this work I will present the design and use of a photonic chip as an hybrid platform to excite neurons by means of optogenetics, a technique described in section 3.2.
The crucial points during the design of the chip were:

- The coupling of light inside the photonic chip, considering that this coupling must not be too bulky or cumbersome in order to perform experiments under a microscope;
- The possibility to excite either single or many neurons simultaneously;
- The ability to excite locally only one neuron, with enough intensity and with no residual excitation of other nearby cells.

Considering all these aspects, we designed the circuit shown in figure 4.3. The structures are shown in figure 4.4.

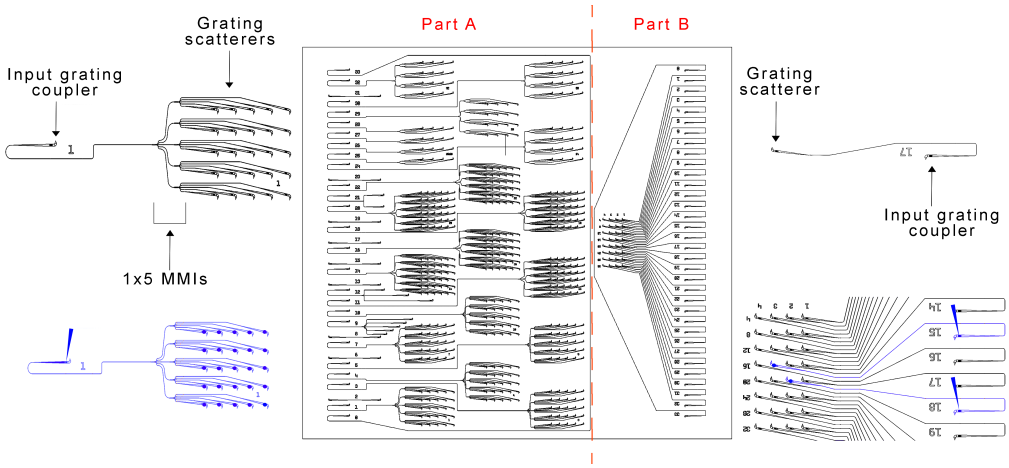

Figure 4.3: **Design of the photonic circuit.** In the figure is shown the designed photonic circuits. In part A each grating coupler addresses light to matrices of scatterers; in part B scatters are addressed singularly by the couplers.

The chip has a 5.3x4.7 μm^2 area and was designed in order to work at 488 nm, with SiN waveguides, embedded in SiO_2. Light is coupled inside the chip through grating couplers and is addressed upwards, to the surface of the chip, by diffractive grating. We will refer to these latter structures as *grating scatterers*. As can be seen from figure 4.3, the design is divided in two main independent parts: the part B is characterized by a matrix of scatterers that can be addressed singularly (i.e. each grating is connected to one single grating coupler), while part A is characterized by matrices of scatterers that are connected each to a single grating coupler. In particular, there are matrices of 4x4 scatters, with a cascade of 1x2 Multi Mode Interferometer (MMIs), 5x5, with a cascade of 1x5 MMIs, and 6x6 with a cascade of 1x2 and 1x3 MMIs. MMIs split evenly the light to the different outputs.
With this design we can perform different kind of experiments with neurons plated on the surface of the chip: with the right part, we can excite either single cells or many, addressing more scatters from different inputs; with the left part, we can, with a single input, address a matrix of scatters at once. In 4x4, 5x5 and 6x6 matrices, grating scatters are spaced 120 μm, 100 μm and 80 μm apart: depending on the culture density, the appropriate matrix can be chosen, in order to perform the desired network excitation.
The grating couplers consist of periodic gratings already designed by the fabrication company. They are arranged with a mutual distance of 127 μm - or multiples of this quantity - in order to be able to couple a 34 fibers-fiber array to all the grating couplers, simultaneously. It must be noticed that the grating couplers work with light coming at 10° angle with respect to the axis perpendicular to the chip plane. As depicted in figure 4.4, we turn the input gratings, and the waveguides bend to turn the light to the scatterers (figure 4.4). This decision was made in order to avoid possible straight light coming from coupling losses that could affect the neuronal culture behaviour during the experiments. The fiber array design is shown in section 4.4. The design and characterization of gratings scatterers and MMIs will be described in the following sections.

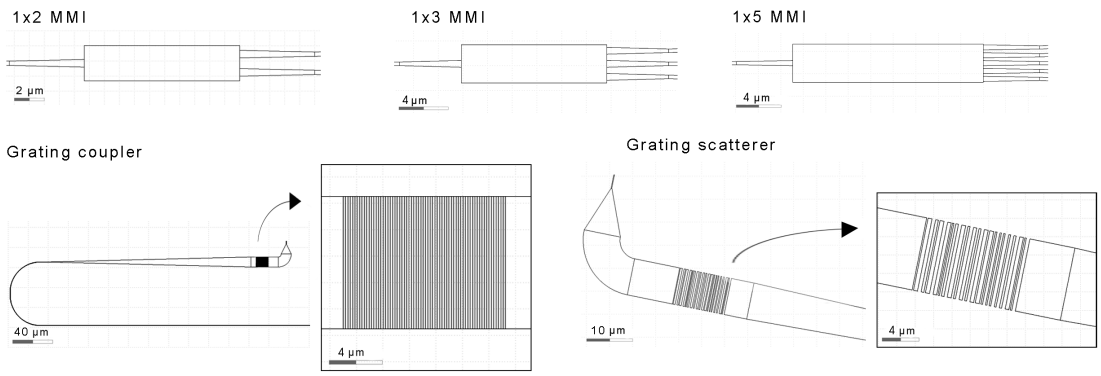

Figure 4.4: **Chip design mask.** In the figure are the details of a 1x2 MMI, 1x3 MMI, 1x5 MMI, a grating coupler and a grating scatterer.

4.2.1 Grating scatterers design

As mentioned in sections 3.4 and 4.1.1, we designed aperiodic grating scatterers with a technique called by us *FEM enhanced transfer matrix method* [138]. The goal of the design was to be able to excite a single neuronal body without affecting the other cells. Therefore, the scatterers should produce a desired light distribution at a certain height above the grating, focusing the maximum intensity in the desired place. In this way, around and above the area where the desired distribution is formed, the light intensity should be low enough to not excite other sample parts that can possibly be hit by the light. Indeed, we decided to work with cells equipped with Channelrhodopsin-2 (ChR2), which are excited by a light intensity higher than 1 mW/mm^2 [16, 62, 76, 82, 123, 125, 139]. We designed the grating in order to be able to get about 10 mW/mm^2 intensity on an area comparable to the neuronal body, a rounded shape with about 10 μm diameter.
The FEM enhanced transfer matrix method was developed by dr. Mattia Mancinelli and me with the objective to perform a fast optimization of aperiodic gratings design given a target scattered light distribution.
There is plenty of literature about grating design, both for light coupling and for the creation of directional light beams for many applications [140–152]. Many optimization techniques were used in order to find the proper geometrical parameters of a desired grating: some are based on the physical models of the system and use optimization algorithms like particle swarm, genetic algorithm or gradient-based methods; others are based on machine learning approaches, with the training of feed-forward or reservoir-computing neuronal networks over specific ranges of the system parameters. The former gives a proper physical description of the system but are computationally expensive, while the latter are fast, but act like black-boxes and are very limited by the training parameters [137, 145, 152]. In our method, we started from a FEM simulation of the system, and then we implemented a particle swarm optimization over a transfer matrix model of the system. In this way, we developed a fast physical based technique.

FEM enhanced Transfer Matrix method

In order to design the grating scatterers, we started from a simple modelling of the system. We consider a two dimensional approximation, where the grating is an interruption of a planar waveguide, with repeated sections of waveguide and cladding materials, named *blocks* (figura 4.5). In particular, we are considering a SiN waveguide embedded in SiO_2 cladding layer. As shown in figure, each block is then formed by a SiO_2 section ($l_j^{SiO_2}$ long) and a SiN layer (L_j^{SiN} long). These blocks have different lengths in an aperiodic grating, and each one transmits, reflects and scatters the light coming from the waveguide. The interference of the fields scattered by the blocks, gives the scattered light distribution by the grating.

The model is based on the following assumptions:

1. each single block acts like a single independent scatterer and the scattering light depends only on the SiO_2 length;
2. the scattering profile of the single block is calculated only once with a

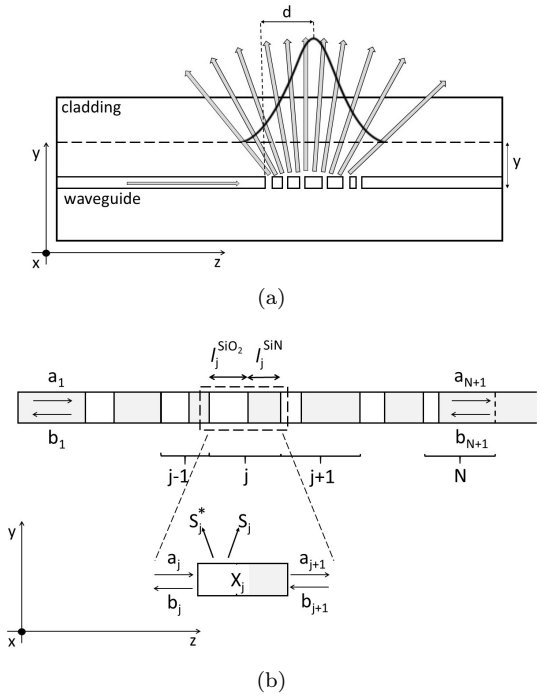

Figure 4.5: **Sketch of the system.** In 4.5(a) is shown a schematic representation of a waveguide interrupted by a grating, with the light scattered upwards; in 4.5(b) is represented the grating with its N blocks, the transmitted components of the field (a_j) and the reflected ones (b_j). Figures are taken from [138]. © 2021 IEEE.

FEM simulator, for different SiO_2 lengths;

3. the same FEM simulation is used to compute also the reflection and transmission coefficients of each block;

4. the light propagating in the waveguide is an optical mode, whose propagation losses are neglected.

Considering z as the propagation direction, once the light propagates in the j-th block, there will be a forward propagating optical mode a_j and a backward propagating one b_j as shown in figure 4.5(b). The effect of the block on the propagation can be described by a matrix X_j that links the input modes a_j and b_j with the output modes a_{j+1} and b_{j+1}, as follows:

$$\binom{a_{j+1}}{b_{j+1}} = X_j \binom{a_j}{b_j}. \tag{4.7}$$

The matrix X_j can be described by the product of two matrices: M_j, that describes the action of the SiO_2 section on the mode (i.e. reflection, scattering and transmission), and F_j, which takes into account the phase accumulated by the mode while propagating in the SiN section:

$$X_j = F_j M_j, \tag{4.8}$$

$$M_j = \frac{1}{t_{21}^j} \begin{pmatrix} t_{12}^j t_{21}^j - r_{12}^j r_{21}^j & r_{21}^j \\ -r_{12}^j & 1 \end{pmatrix}, \tag{4.9}$$

$$F = \begin{pmatrix} e^{-i\phi_j} & 0 \\ 0 & e^{i\phi_j} \end{pmatrix}, \tag{4.10}$$

In (4.9), t_{12}^j and r_{12}^j are, respectively, the transmission and reflection of the SiO_2 layer for a forward propagating mode, while t_{21}^j and r_{21}^j are the same coefficients for a backward propagating mode. Since optical reciprocity, $t_{12}^j = t_{21}^j = t^j$ and $r_{12}^j = r_{21}^j = r^j$. These coefficients depend not only on the interface, but also they take into account the influence of the scattered field on the reflected and transmitted modes. In (4.10), $\phi = n_{eff} k_0 l_j^{SiN}$, where n_{eff} is the effective refractive index of the input waveguide mode a_1, $k_0 = 2\pi/\lambda$ and λ is the wavelength. Considering a grating formed by N blocks, with the transfer matrix formalism we model their effect on the propagating modes:

$$\binom{a_{N+1}}{b_{N+1}} = X_N \binom{a_N}{b_N} = \ldots = \prod_{j=1}^{N} X_j \binom{a_1}{b_1}, \tag{4.11}$$

where a_{N+1} is the mode at the end of the grating. Clearly, the mode entering the grating is a_1=1, and b_{N+1}=0, since the grating is terminated by a waveguide that let only the forward propagating mode a_{N+1} to propagate. The solutions of this equation give a_j and b_j for any j.
As mentioned before, we can consider the total distribution of the scattered light as the interference of the fields scattered by all the grating blocks:

$$I_g(y,z) = \left| \sum_{j=1}^{N} E_j(y,z) \right|^2, \tag{4.12}$$

where

$$E_j(y,z) = a_j S_j(y,z) + b_{j+1} S_j^*(y,z) e^{i\phi_j}. \tag{4.13}$$

Since $E_j(y,z)$ and $\sum_{j=1}^{N} E_j(y,z)$ are complex quantities, one has access both to the amplitude and to the phase of the scattered fields. $S_j(y,z)$ and $S_j^*(y,z)$ are the fields scattered by the j-th block, for the forward and backward propagating optical modes.
Given the theory, one can compute the r^j and t^j coefficients and the scattered field S_j for each block with a FEM simulator (in our case we used COMSOL Multiphysics 5.3a). The field S_j^* is obtained simply by reflecting z to $-z$. These parameters are computed for lengths $l_j^{SiO_2}$ and l_j^{SiN} that can be effectively fabricated. Their values in particular change between the minimum resolution provided by the fabrication and the maximum value that can be chosen accordingly to the specific grating: the maximum value of l_{Si} must be λ/n_{eff}, so to restrict the phase change in the Si layers to 2π, while the maximum value of l_{SiO_2} must be chosen considering that the longer is the SiO_2 layer, the more light is scattered (and the less is transmitted to next blocks). These criteria for

the length ranges are not mandatory: if followed, they just save computational time and help the optimization algorithm to more easily find the solution in the parameter space. The number of length values depends on how many variables we want the optimization algorithm to explore.
Once the parameters are computed with the FEM simulation, one uses equations (4.12) and (4.13) in the loss function of an optimization algorithm in order to get the desired grating design. The accuracy of the reconstruction of the 2D scattered field profile by the Transfer Matrix method can be seen in figure 4.6, where, given a simple periodic grating, the scattered fields simulated by COMSOL is compared to the one obtained with our method, implemented in MATLAB 2019b. Small differences can be due to the scattering boundary conditions used in the FEM simulation: in this case indeed only normal incidence fields are transmitted at the boundary of the simulation domain, while for all the other incidence angles light is partially reflected.

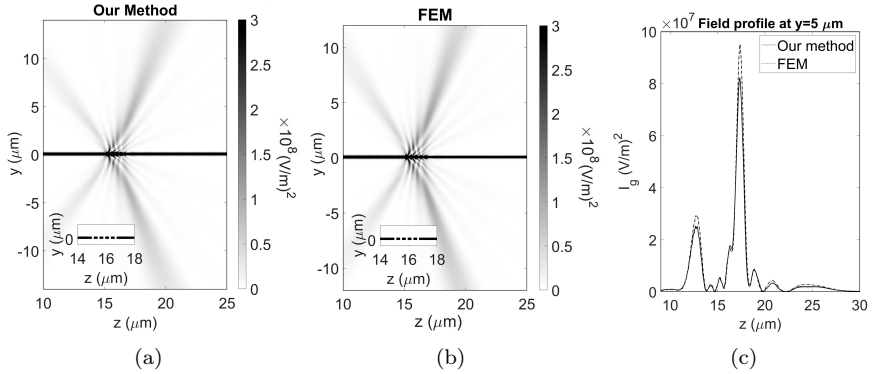

Figure 4.6: **Comparison between FEM simulation and our method.** Comparison between the scattered 2D distribution of the field obtained with our method (a) and a FEM simulation (b), in the case of a periodic grating made by N=5 blocks of 250 nm long SiN layer and 150 nm long SiO_2 layer. The SiN waveguide is 150nm high and the light wavelength is 488 nm. The dark horizontal line refers to the optical mode which propagates in the waveguide. The gray scale refers to the field intensity and is given on the right of the panel. The insets show a sketch of the periodic N=5 grating. (c) The Ig(y,z) profiles obtained with our method (full line) and the FEM simulation (dashed line) at y=5 μm are shown. Figures are taken from [138].

The use of a transfer matrix method in the optimization instead of a full FEM simulation, saves a lot of computational time. In fact, simulation methods like FEM, FDTD or CAMFR require from tens of seconds up to tens of minutes to complete a single grating simulation [136, 137, 153, 154]. These times transform to days or weeks if an optimization algorithm has to explore a wide parameter space. In our approach, a grating optimization requires only few hours on a laptop with a i5-1035G4 CPU with 8 GB RAM. For example, the optimization of the scattered profile at a given distance from a grating with N=10 blocks, takes 6 days with a FEM simulator and just 14 hours with our method. In [138] we show the successful use implementation of our method for different desired shapes of the scattered field. Moreover, this method can be used also to implement grating couplers design.

Optimization of the grating for the bio-chip

For the sake of designing grating scatterers in our photonic chips, we optimized a grating to produce a blue spot of the dimension of a typical neuronal soma (about 10 μm) at a distance that matches the position of the neurons on the chip surface. In this case, the waveguide was a 150 nm high SiN waveguide (n=2.0354) embedded in a SiO_2 domain (n=1.4688), being the working wavelength 488 nm. The domain was supposed infinite in the simulation, according to the fact that the refractive index of SiO_2 is not much different from the refractive index of the watery solution that will be present in the experiments above y=2μm. 8 values were chosen for l^{SiO_2} and l^{SiN} in 150-400 nm and 150-450 nm ranges respectively. The number of blocks was chosen to be N=20 and the light polarization was set to transverse electric (TE). We wanted the spot to be formed at a distance of y=5 μm from the waveguide. This distance was chosen considering that the SiO_2 layer on the top of the grating was 2μm thick and that a neuronal body is about 10μm thick: therefore, every distance from the grating plane between 2μm and 12μm would ensure the cell excitation. Computed the scattering parameters by a FEM simulation, we implemented a particle swarm algorithm to optimize the scattered profile at y=5 μm [145, 152, 155–157]. For each iteration, the distribution profile ($I_g(y,z)$) was computed, normalized and compared with the target distribution (I_g^T), a gaussian with a FWHM of about 7 μm

$$I_g^T = e^{-(\frac{z-z_c}{w})^2}, \tag{4.14}$$

where z_c is the z position of the desired distribution, and w=4.24. Beside l^{SiO_2} and l^{SiN}, also z_c was left as a free parameter between 14μm and 21μm (the first block of the grating started at 15 μm). The cost function Ξ of the optimization algorithm was defined as the standard deviation of the obtained distribution $I_g(y,z)$ from the desired one $I_g^T(y,z)$ plus the transmitted $T = |a_{N+1}|^2$ and reflected $R = |b_1|^2$ light from the grating, i.e.

$$\Xi = \sqrt{\int_{space} (I_g^T(y,z) - I_g(y,z))^2 dydz} + R + T. \tag{4.15}$$

Since we are interested in the shape of our scattered distribution, both $I_g(y,z)$ and $I_g^T(y,z)$ are normalized to 1, while the two last terms are introduced in order to minimize the waveguide transmission and reflection, i.e to maximize the scattered light from the grating. In this way, the power transfer efficiency from the waveguide to the neuronal body is maximized. After the optimization, it was obtained the grating shown in figure 4.7(a), for a total length of about 11.5μm, with R=0.009 and T=9x10^{-5}. In figure 4.7(a) the structure of the grating is represented in white, and the line at y=2μm accounts for the thickness of the SiO_2 layer above the grating. The green square represents a neuronal body 10 μm long and thick, positioned over the grating. In figure 4.7(b) is shown the profile of the scattered field at y=5 μm, compared to the target distribution: it can be seen that the field distribution resembles well the desired gaussian shape. Then, the spot created by the grating scatterer can be obtained by the multiplication of the fields propagating along z and x directions. The field along z is the one calculated by our method, while the field distribution along x results from a FEM based mode solver, considering a waveguide with the same

materials and a rectangular cross section 8×0.15 μm^2. In figure 4.7(c), the spot at y=5 μm is represented.

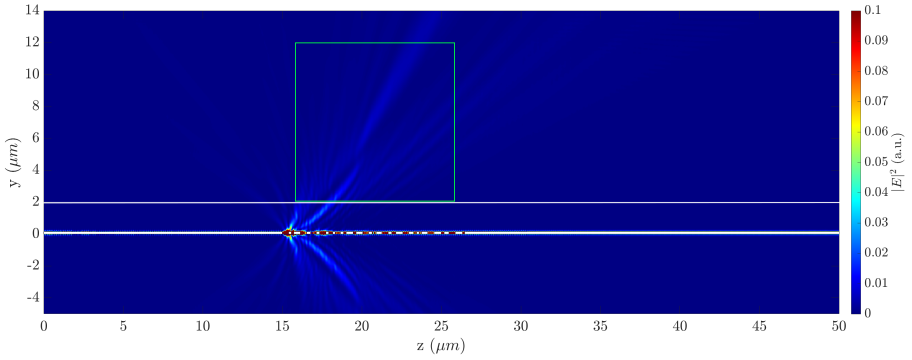

(a)

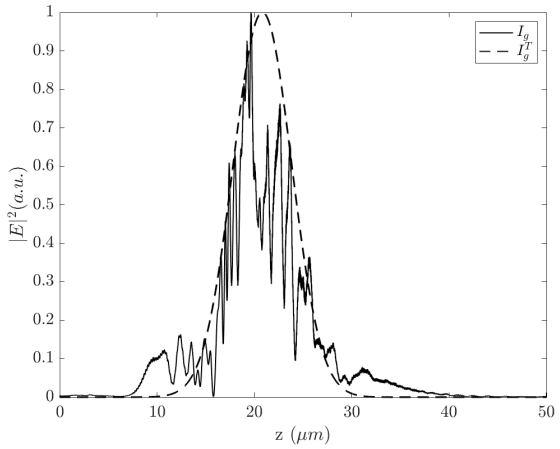

(b)

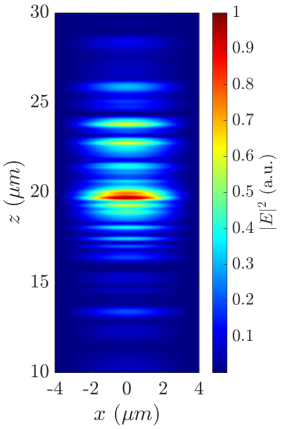

(c)

Figure 4.7: **The optimized grating.** (a) Distribution of the scattered light ($|E|^2$) in a 2D cross section of the system. The grating obtained after the optimization is represented in white, while the scattered field is represented in *jet* color map, in arbitrary units. The white horizontal line positioned at y=2μm refers to the thickness of the SiO_2 layer above the grating. The green square represents a neuronal body of 10 μm long and thick, positioned over the grating. (b) The profile of the scattered field obtained at 5 μm compared with the target gaussian distribution. (c) The field distribution created at 5 μm in the (x,z) plane.

Once the grating is optimized, we define the grating efficiency η as the percentage of the input power that is diffracted in the spot. If the integrated optical intensity on the spot is I_{spot}, and the overall scattered intensity is I_0, then

$$\eta = \frac{1}{2}(1 - R - T) \cdot I_{spot}/I_0. \tag{4.16}$$

Here, the 1/2 term accounts for the symmetric up and down scattering (see Fig. 4.7(a)), the term $(1 - R - T)$ accounts for the input light which is reflected

or transmitted by the grating, while the last term considers the fraction of scattered light that is actually concentrated in the spot. I_0 is calculated as the line integral of the scattered light at y=1 μm in order not to overlap with the evanescent field of the waveguide mode, while I_{spot} is the integral of the scattered profile on a z interval equal to a window of $10\mu m$ centred in z_c, at y= 5 μm. The efficiency of the optimized grating was 37%.
Then, the same grating was simulated with COMSOL Multiphysics in order to check the validity of our method, with the same domain used for our simulation. In this case the value of the efficiency calculated as in (4.16) is indeed 36%, near to the expected one. Comparing the 1D field profiles in figure 4.8, it can be seen that at y=2 μm the field distributions are really similar, while they differ a bit at y=5 μm, but still keeping an overall width of about 10 μm. We then also performed a FEM simulation with a domain that resembles more the system during the experiments: in the simulation cladding was added a Si layer under the bottom SiO_2, and water is considered for y>2 μm. The results are shown in figure 4.8: first of all, looking at the 2D scattering maps, our method is able to simulate the grating scattering as the FEM simulator. However, it can be seen both from the 2D map and from the 1D field profiles at y=2 μm and y=5 μm, that the presence of water above y= 2μm changes slightly the scattered distribution, as expected. Since the presence of the interface SiO_2-water induces more interference in the SiO_2 domain, it was not possible to compare the efficiency of the system in the two situations with the formula (4.16). We then computed the efficiency (η) calculating the integral of the poynting vector $\vec{P}$ along a 10μm line, orthogonal to the main scattered beam, and normalizing it to the input power P_0 used in the simulation:

$$\eta = \frac{\int_{line} \vec{P}(zy)\vec{n}(zy)dzdy}{P_0}, \tag{4.17}$$

where $\vec{n}$ is the versor of the system, considering the 2D simulation. η gives the percentage of the energy flux that crosses the line. Considering this, the efficiency in the case of the SiO_2 domain increases from 37 % (using (4.16)) to 42 % (using (4.17)): this is due to the fact that we are now considering the scattered field along a line orthogonal to the main beam, not only on the horizontal plane at y= 5μm, as in equation (4.16). Moreover, the choice of the y position for the calculation of I_0 affects the η value in (4.16).
The presence of the water above y=2μm changes the efficiency from 42% to 48%. This increase can be due to the reflections on the SiO_2-water boundary, which recouple light to the grating which is in turn scattered again, creating an additional contribution to the scattering intensity. From this calculation we can say that the approximations we did for ease the design of the grating scatterers are not negatively affecting the system. As can be seen in figure 4.7(a), since the symmetric perturbation of the waveguide (full etch), the scattered light goes half up and half down. Thus, the maximum efficiency is 50%. Comparing the 2D scattering maps between our optimized grating and a periodic grating, it can be seen that thanks to the optimization we are able to spatially focalize also along the direction of propagation of the scattered field (figure 4.9). All considered, the designed grating scatterer has both a good spatial focalization and a good efficiency.

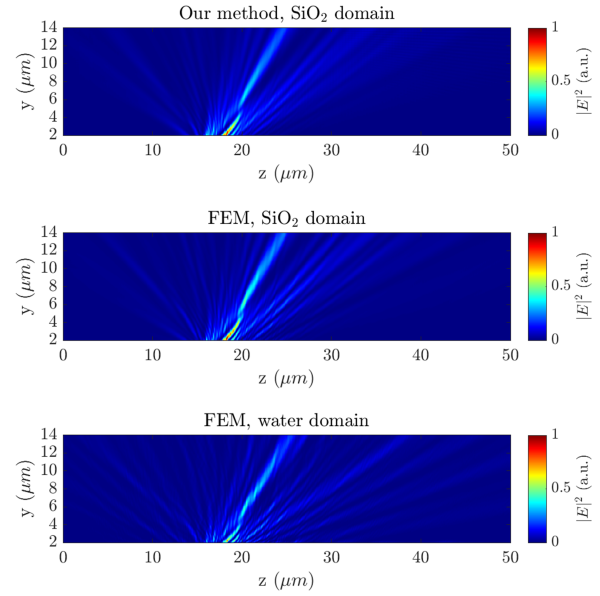

(a)

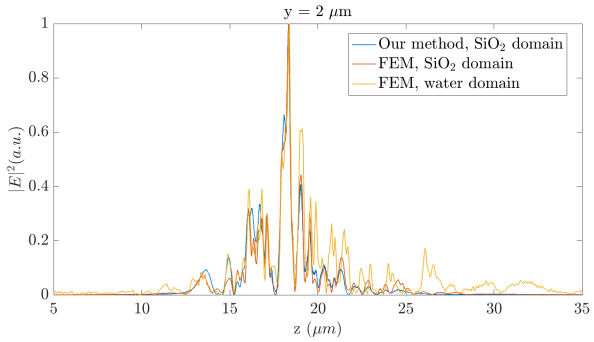

(b)

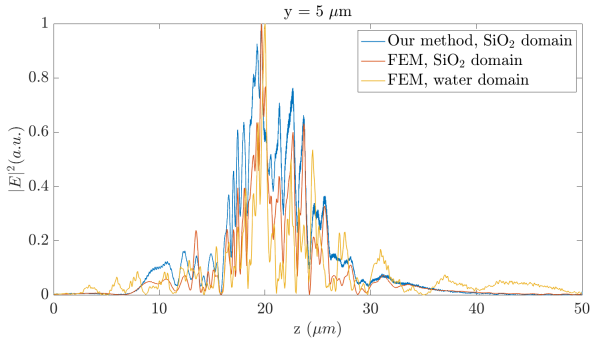

(c)

Figure 4.8: **Simulation of the grating scatterer.** (a) 2D scattering maps in the yz plane, between y= 2 and 14 μm, in the case of our method, a FEM simulation with Comsol Multiphysics and still a FEM simulation but considering water instead of SiO_2 in the simulation domain for y>2 μm. (b) 1D profiles for the three cases at y=2μm and (c) y=5μm.

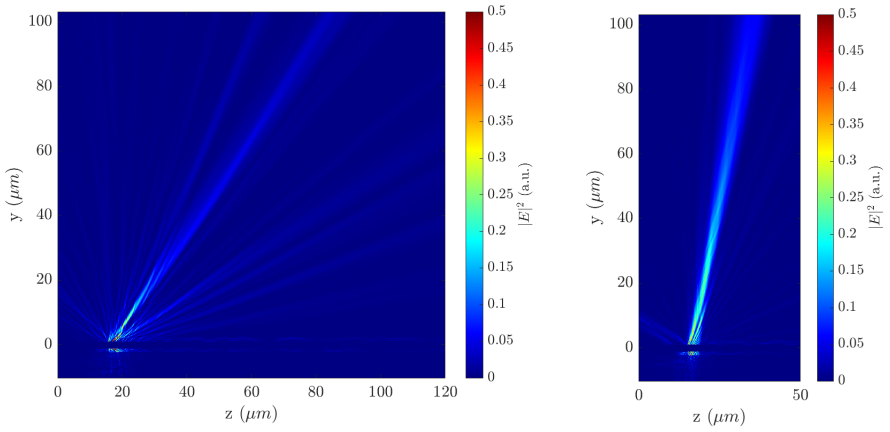

Figure 4.9: **Comparison with a periodic grating.** (a) Scattering of the optimized grating considering water for y>2 μm, up to 100 μm. (b) The scattering, in the same domain, from a periodic grating with l_{SiO_2}=185 nm and l_{SiN}=178 nm.

4.2.2 MMIs design

The Multi Mode Interferometers (MMIs) are passive optical structures usually used as power splitters or combiners, which means that N inputs can be turned into M outputs. An MMI is essentially a planar waveguide (body of the MMI) that can support multiple modes. The light coming from a thinner input waveguide excites the modes inside the MMI body. These modes propagate through the MMI and the field at the end of the structure can be computed with modal propagation analysis. Following this theory, if the MMI supports M modes, the propagating field can be expressed as

$$E(x,y,z) = \int_{m=0}^{M-1} a_m E_m(x,y) e^{i\beta_m z}, \tag{4.18}$$

where a_m is defined as

$$a_m = \int_{\infty}^{\infty} E(x,y,0) E_m^*(x,y) dxdy \tag{4.19}$$

i.e. the overlap between the input field and the field distribution of the m-mode [158]. Moreover, the concurrent propagation of the different modes give rise to an interference pattern that creates multiple images of the input field with a characteristic beat length. Changing the geometrical parameters of the MMI structure it can be chosen a specific length for which M images of the N inputs can be coupled to an output waveguide [159].

In our case, we wanted a single input to be evenly split in M=2, 3 or 5 outputs. I have to thank my colleague Davide Bazzanella for the simulation and design of all the MMI structures used in the photonic chip. In particular, he implemented in MATLAB the simulation and optimization of the MMIs, starting from a dataset created with the FEM simulator COMSOL Multiphysics. First of all, he generated a collection of field profiles for different rectangular waveguide

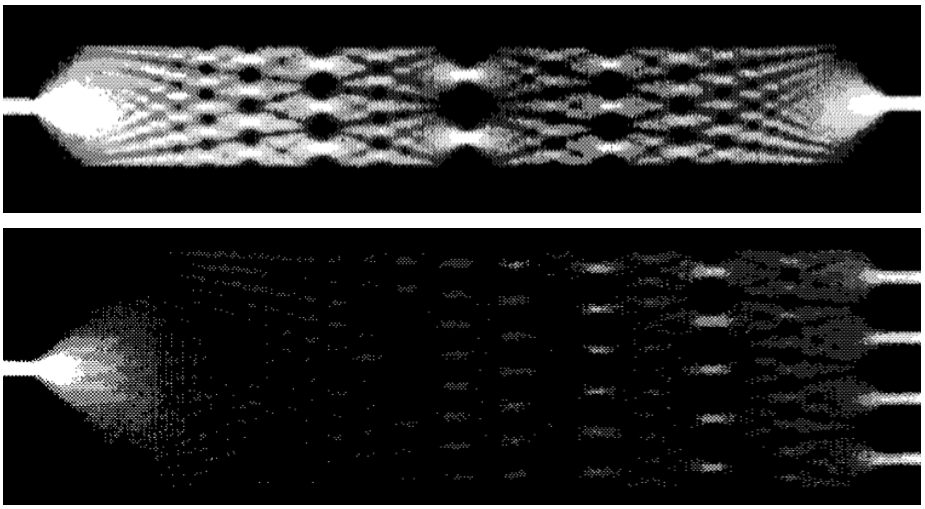

Figure 4.10: **Self-image effect.** A 1x1 and 1x4 MMI simulation images, taken from [159]. © 1995 IEEE.

widths. Then, he used them to implement the field propagation theory inside a genetic optization algorithm, with the goal to maximize the transmission of each channel. The algorithm evaluates the performance of the system for parameters such as the input waveguide widths and the width of the MMI (to reduce the parameters, the output waveguides width was fixed as equal to the input ones); the genetic algorithm optimizes for the best length of the MMI structure (along z axis) and the best position of the input and output ports along the MMI's width (x axis). Then, the best configurations were chosen depending on the largest coupling to the output waveguides and on the length of the structure. The 1x2, 1x3 and 1x5 MMIs designed with this technique were inserted in the photonic circuit design.Their experimental characterization is discussed in section 4.3.1.

4.3 Characterization of the photonic chip

After receiving the SiN chips, fabricated using the IMEC SiN-Photonics BioPIX150 technology, we assembled an experimental set-up with visible sources to allow the passive testing of the photonic circuits. The setup consists in a laser source, an optical line, an alignment stage where the chip is placed, and a visible Optical Spectrum Analyzer (OSA, YOKOGAWA AQ6373B) (Figure 26). The source is an in-fiber supercontinuum laser (FYLA SCT500 SN0719-1) which has a 1.5W power within the full spectrum (400 nm - 2400 nm). More specifically, the light coming out from the laser is filtered with a low-pass filter and directed with a mirror to a polarizer cube in order to select a linear polaritazion, that can be modified with $\lambda/2$ and $\lambda/4$ waveplates. Then, the light arrives to the lens of a collimator that couples the light to an optical fiber, which, in turn, is connected to a tapered fiber on the alignment stage. The alignemnt stage is formed by two 3-axis stages that can hold fibers for both bottom coupling and grating coupling (Fig. 4.13). The sample is positioned between two alignment stages, as can be seen in figure 4.13(a). For this characterization, we cut the

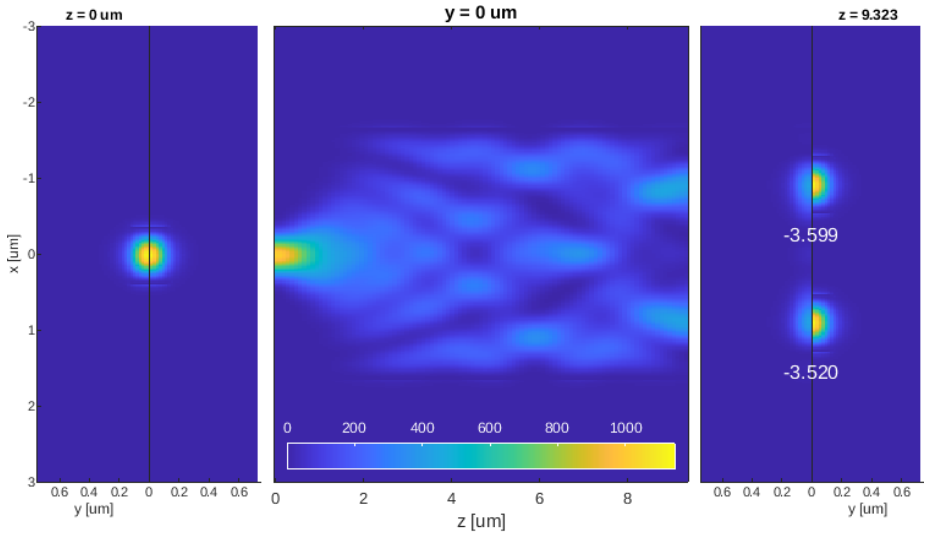

Figure 4.11: **MMI simulation.** From left to right, the input field profiles, the field propagation in the $z - x$ plane and the output field profile are shown. Specifically, the left half of the first plot is the input field profile, while the right half is the field profile at the input of the MMI. Both maps represent the top half of the section only, assuming symmetry around the horizontal plane. The second plot is the field propagation on the horizontal plane at $y = 0$. Similarly to the input, the third plot represents the field profile at the output of the MMI in the left half and the excited field profile at the start of the output waveguides. The two white numbers represent the transmission values in dB.

chip removing grating couplers, in order to align to the chip in butt coupling (Fig. 4.13(b)). The light coming from the test structures is then collected with a cleaved fiber that can be angled to different angles. The signal is then analized by a visible OSA. The combination of the supercontinuum source and the OSA, let the characterization of the transmission from the optical structures in a broad spectrum: in particular we focused our attention in the range 483-534 nm. As can be seen from figure 4.12, in the optical line a flipping mirror enables to introduce in the optical line also a second laser source. Moreover, a 1x2 switch, with one output to the input fiber and one to the OSA allows the collection of the input spectrum, when needed. This setup was used to perform the experimental measurements for the characterization of MMIs and grating couplers.

4.3.1 MMIs

First of all, MMIs were tested, with TE polarization. Taking advantage of the test structures in the chip, the output light from a 1x2, a 1x3 and a 1x5 MMIs was measured. In these test structures, the output consisted in coupling gratings, with a nominal coupling angle of 10°. The setup of the measurement is shown in figures 4.12, 4.13(a) and 4.13(b). For each output of the MMIs, first the input spectrum was collected and, then, the output spectrum. The output spectra (O) are normalized to the input one (I) and, for each MMI, every curve

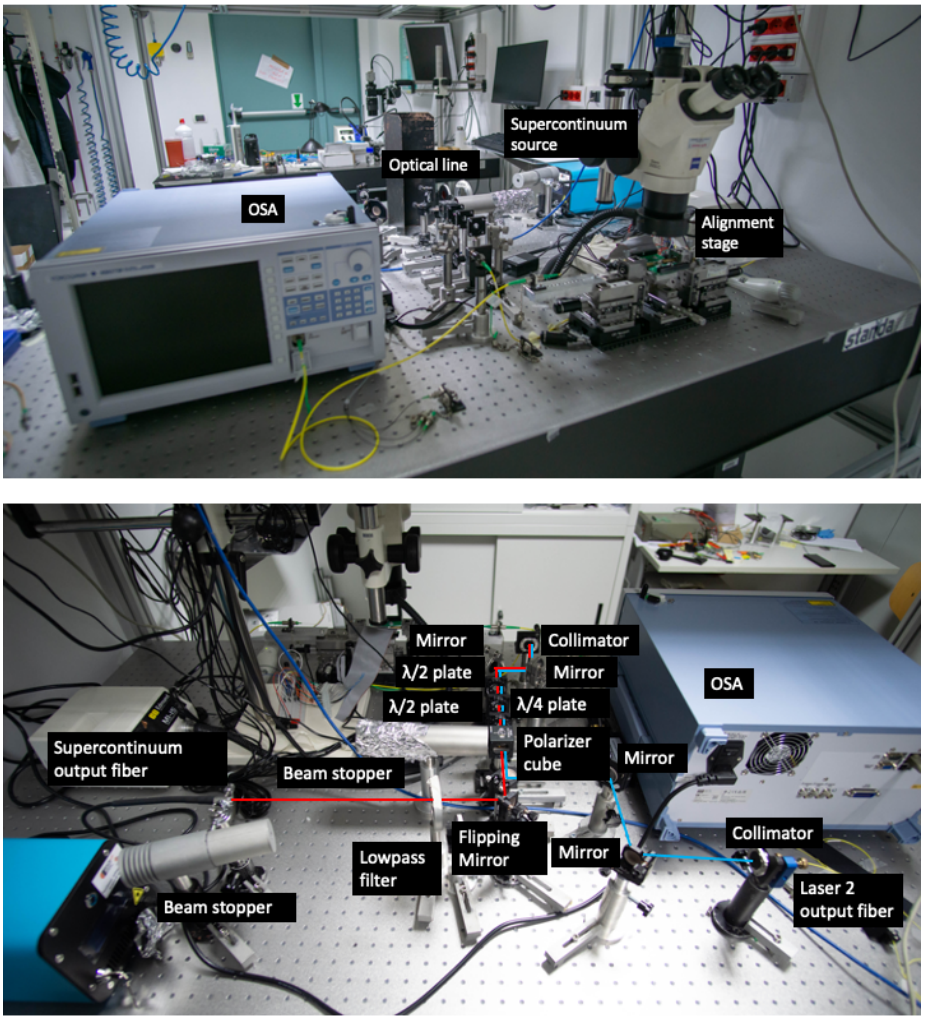

Figure 4.12: **Experimental setup.** In the photos the experimental setup used for the characterization of the passive optical components in the photonic chip is shown.

is normalized to the sum of all the outputs (Σ). Data are shown in figure 4.14, where, for each MMI, the acquired spectra and the $\frac{O/I}{\Sigma}$ values in the range 483-534 nm and between 484 nm and 492 nm are shown. The results are summarized in the table 4.1, where the averages between 486 nm and 490 nm and their standard deviation for 1x2, 1x3 MMIs and 1x5 are reported. The MMIs are well balanced for the 1x2 and 1x3 cases, while for the 1x5 case a slight disequilibrium is observed. These results are confirmed by the photos shown in figure 4.15: the 6x6 matrix, created with 1x2 and 1x3 MMIs is well balanced, while the 5x5 matrix, created with 1x5 MMIs, do not show homogeneous scattering.

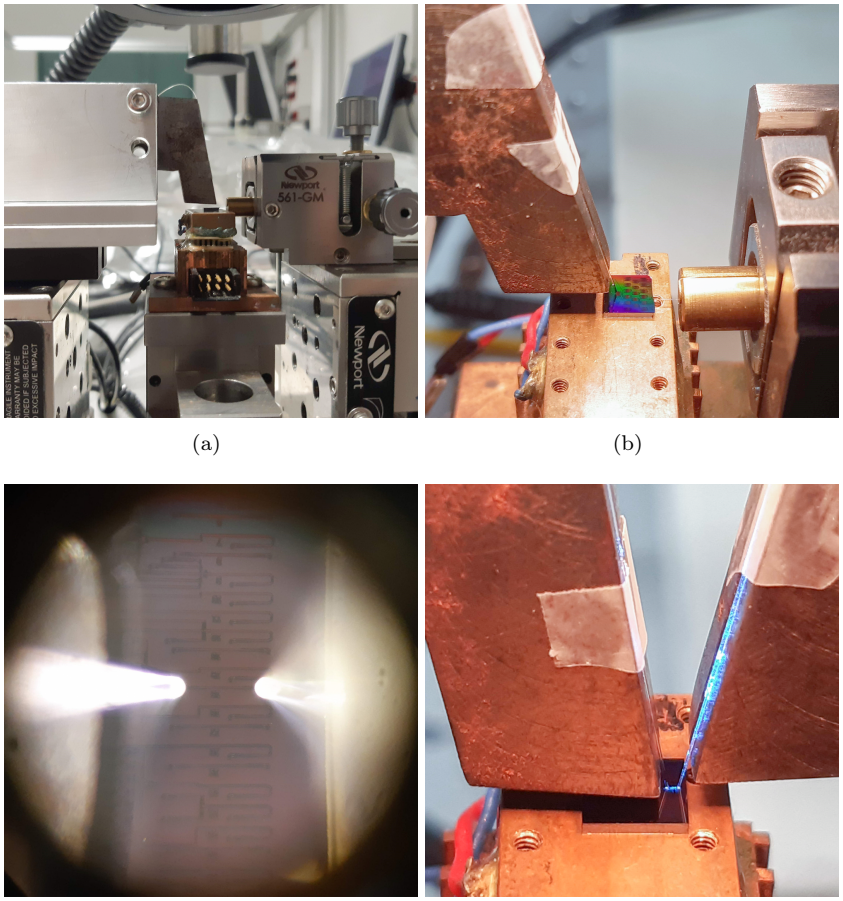

(a) (b)

(c) (d)

Figure 4.13: **Different configurations of the sample stage** In figure different photos of the sample stage taken during the characterization of the chip are shown. (a) and (b) show the configuration used for the butt coupling, while (c) and (d) show the configuration for the grating coupling. (c) is a photo taken from the microscope of the setup.

Table 4.1: **MMIs' characterization results:** the average $\frac{O/I}{\Sigma}$ values between 486 nm and 490 nm with the respective standard deviations.

Structure	Port 1	Port 2	Port 3	Port 4	Port 5
1x2 MMI	0.52 ± 0.04	0.48 ± 0.04			
1x3 MMI	0.33 ± 0.05	0.36 ± 0.08	0.32 ± 0.03		
1x5 MMI	0.11 ± 0.04	0.37 ± 0.05	0.1 ± 0.01	0.29 ± 0.03	0.12 ± 0.02

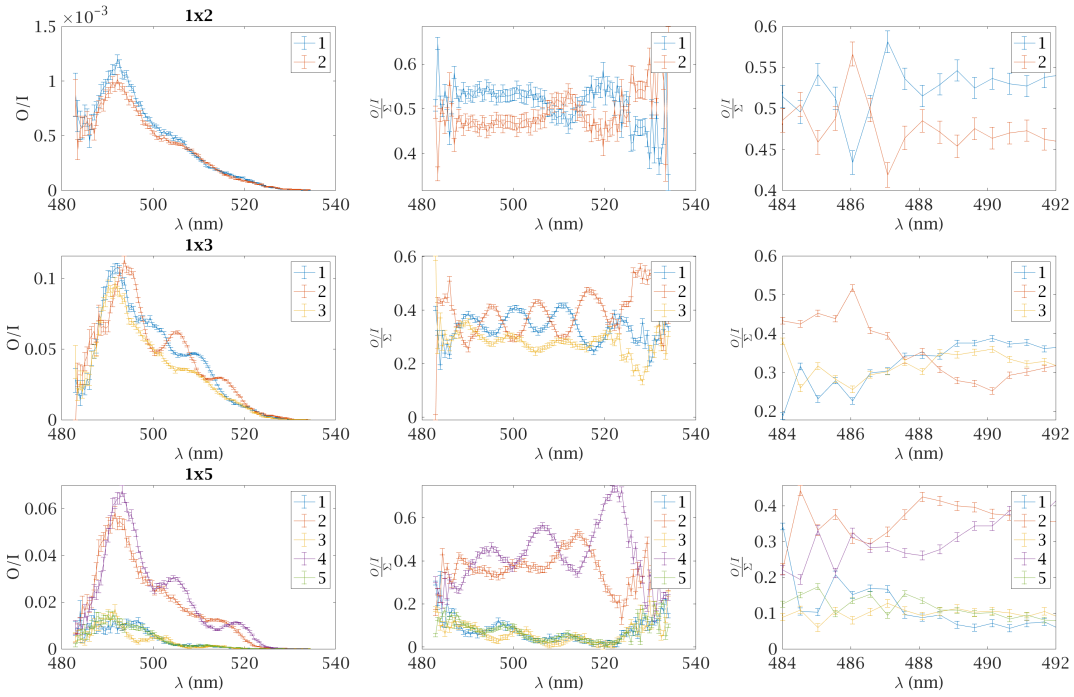

Figure 4.14: **Experimental characterization of MMIs:** For each MMI, the normalized spectra collected from each port, the curves normalized by their sum ($\frac{O/I}{\Sigma}$) and a zoom around 488 nm are shown.

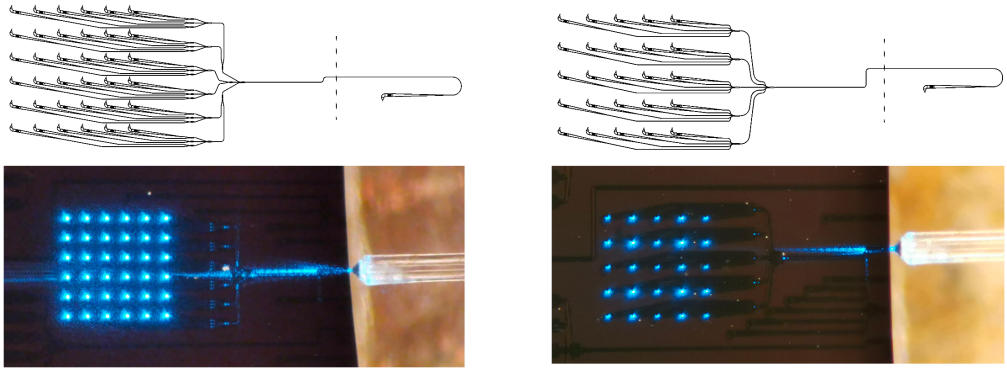

(a) 1x6 MMI

(b) 1x5 MMI

Figure 4.15: Photos of 1x6 and 1x5 MMIs, with the respective schemes. The dashed lines represent the cut positions.

4.3.2 Grating couplers

Grating couplers were characterized in order to estimate the coupling losses. We performed two measurements on coupling gratings with a blue light laser (Cobolt 06-MLD - 488 nm), one in butt coupling with a tapered fiber, and one in a test structure with two coupling gratings connected by a short waveguide. In the case of butt coupling, 9.7 dB of insertion losses were simulated, as the result of the coupling between the tapered fiber and the waveguide section. Photos of the different configurations of the setup are shown in figure 4.13. From measurements, we got a value of - 14.3 $\pm$ 0.2 dB of coupling losses.

4.3.3 Fiber array alignment

In order to be able to perform measurements on the grating scatterers and study the overall behaviour of the whole chip, more than one input coupler must be used. As already mentioned, the inputs are arranged with a pitch of 127 μm in order to be able to couple a 34 fibers-fiber array. In fact, we ordered from PLC Connection company a custom Al-coated fiber array, able to couple the light in the inverted couplers and with proper sizes, to fit with our microscope systems. Moreover, the alignment must be resistant and compatible with water media. The final use of the chip, indeed, is to excite neurons: to perform this kind of experiments, neurons are immersed in a watery solution; to look at the neuronal culture and collect possible fluorescence signals, the system must be put under the microscope. We then decided to design a system chip+fiber array in order to use a small focal length water immersion objective (Olympus UMPLFLN20XW, working distance of 3.5 mm). The schematic drawing of the fiber array is shown in figure 4.16. It is a 6x9x1.55 mm^3 quartz glass block with a polish angle of 40 $\pm$ 5° for 10° back reflection with index match adhesive that glues an Aluminium coated surface, protected by glass layer. 34 ThorLabs SM450 fibers are aligned in a v-array, fixed with epoxy and protected by a silicon layer. Each fiber ends with an APC connector.

In order to perform a long-lasting alignment, we followed the steps shown in figure 4.17. First, to lift the fiber array at the surface chip plane, a similar-thickness silicon chip is glued under the fiber array. Then, the fiber array is grabbed by a custom teflon fork-like structure: it is a tweezer that can be shrinked with a screw. This structure is mounted on a 3-axis stage. In the meanwhile, the chip is glued on the side of an about 1x2 cm^2 piece of glass and fixed on a 3-axis and a rotational stage. Then, the fork that helds the fiber array is moved until all the entrances of the fiber array are aligned to the input grating couplers. To make an active alignment, on the chip an allignment test structure was designed: the first and last grating couplers are connected by a waveguide. Therefore, one grating can be used as an input from the first fiber of the fiber array: the system is aligned when a signal is detected by the last grating (i.e. by the last fiber of the fiber array). Indeed, if the light is properly coupled to the first and last grating, it means that also all the other gratings are aligned to the fiber array. This coupling is performed by putting a small drop of water on the surface of the chip: indeed, the presence of air or water between the chip and the fiber array changes the coupling angle. Since the system will be water immersed for the experiments with neurons, it is important to ensure the coupling with water. Once the correct position is found, a drop of glue is

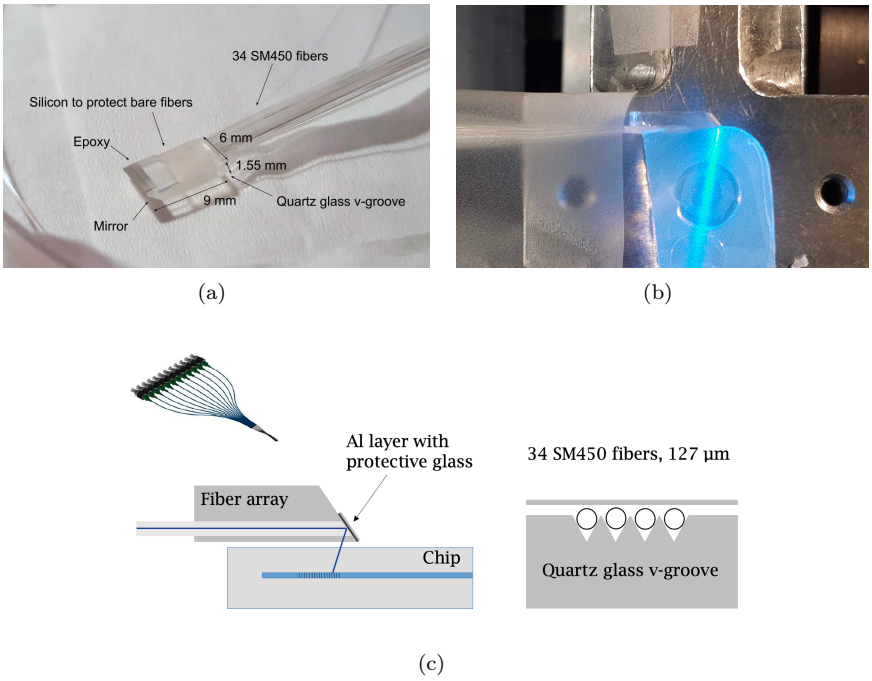

Figure 4.16: **Fiber array structure and working principle.** (a) The main parts of the fiber array block; (b) a photo of the beam coming out from the fiber array and propagating in a 2% agarose gel, used to visualize the output light beam; (c) a sketch of the cross section of the fiber array aligned to a coupling grating inside the chip, while on the right is represented how the fibers are aligned inside the fiber array.

used to fix to the glass substrate of the chip. This is very critical: every minimal movement due to vibration or stretch of the glue on the system can affect the final alignment. Once the first drop is dried, the fork is detached from the fiber array. Another small drop of glue is then inserted in the small channel between the fiber array and the chip to seal the system and avoid the penetration of biological or saline waste during the experiments. The only possible negative effect of this last procedure is that small air bubbles can be formed and affect the coupling if located exactly between the fiber array output and a grating coupler.
The glue used to fix the system was Attack (ethyl cyanoacrylate), chosen because it has low viscosity (20-80 cps), good tensile strength (2700 psi), a refractive index near to the water one (1.4), and it dries in a time sufficiently long to intervene if something happens to the alignment after the drop, and in a sufficiently short time for the experiment. Usually, for a small drop, some hours are sufficient to dry. Moreover, Attack is water resistant, ethanol resistant (ethanol is often used to sterilize components before biological experiments) and biocompatible. This last aspect will be discussed in the following section, together with other adhesives used in the packaging of the system.

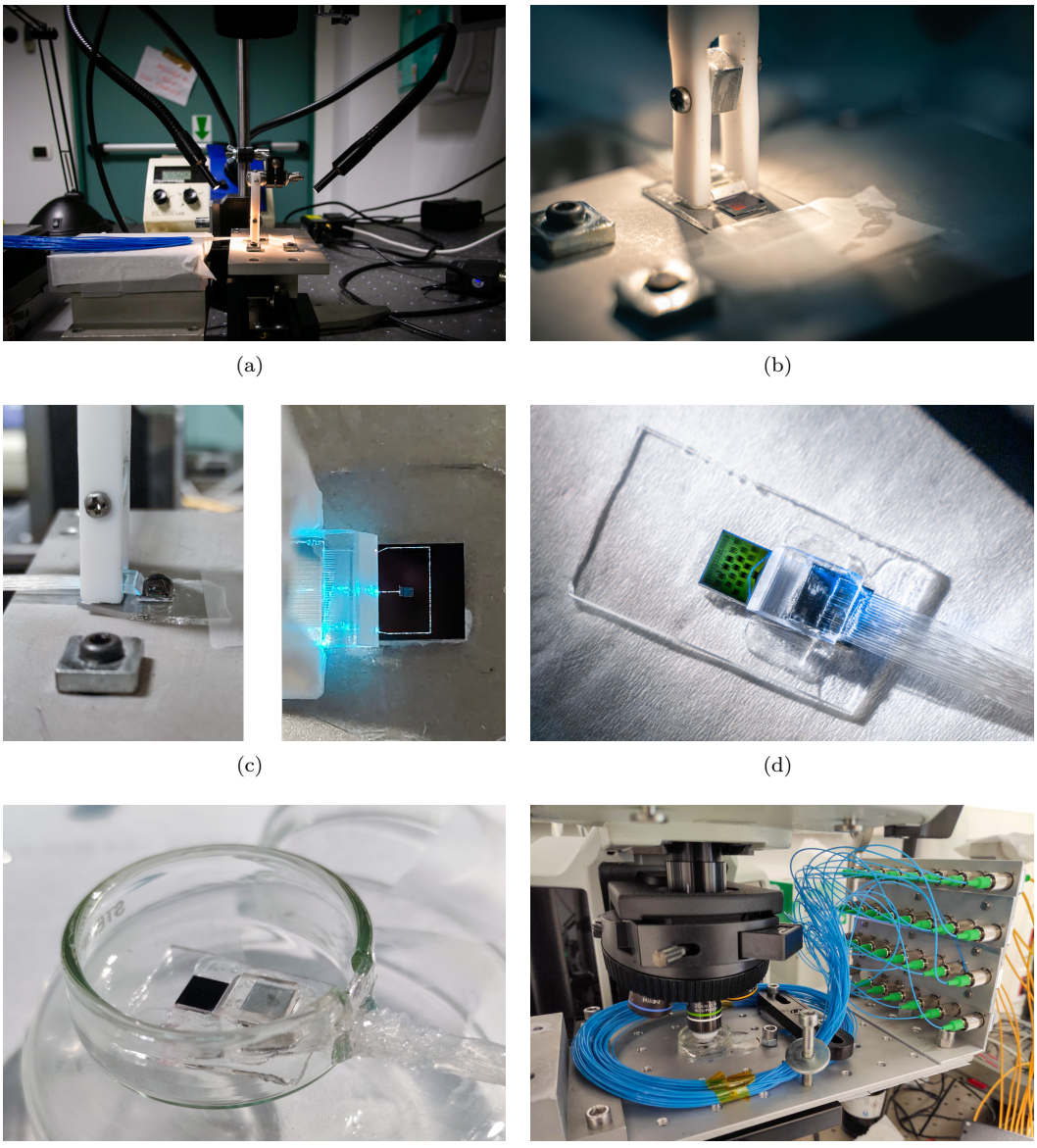

Figure 4.17: **Alignment procedure and packaging.** (a) The alignment setup. The chip is on the sample holder, while the fiber array is held by the fork, connected to a 3-axis stage, positioned behind the sample stage; (b) the detail of the fork holding the fiber array during the alignment procedure; (c) the drop on the chip and the sistem aligned, while the glue is drying; (d) the system chip+fiber array aligned, without the fork; (e) the system is inserted in a Petri dish and sealed with silicone; (f) the final package, positioned under the 20x water immersion objective.

4.4 Package

The fiber array+chip system must be inserted in a Petri dish that can contain the watery solution in which neurons will live during the experiments. Since it is known that plastic dishes can not be re-used in biological experiments because of plastic deterioration due to heat and sterilization techniques, we decided to use glass Petri dishes, with a diameter of 40 mm and walls 12 mm high. Using a small drill with a diamond tip, a window of about 5 mm is cut on one side of the Petri. In this way it is possible to insert the chip+fiber array system inside the Petri, with the optical fibers coming out from the fissure. Then, the fissure is sealed with some silicone. Between several different silicones, Elastosil E43 was chosen, since it is used also for the sealing of MEA chips. It is transparent and has good viscosity (250000 cps), enough to leak into the fissure but not spread all around the Petri; it has low tensile strength (899 psi) to not broke the fibers during handling and it cures at room temperatures in about 20 minutes.
The biocompatibility of Attack and Elastosil was tested together with other adhesives, putting a small drop of these adhesive in different dishes. In these dishes neurons were plated. After 5-6 days, we checked the status of the cells: only in the case of Attack and Elastosil the neurons survived. From now on, we will refer to this system of the chip+fiber array inside the Petri dish as *package*. The whole system is shown in figure 4.17(f). The fibers of the fiber array (blue ones in figure) end in an array of connectors in which the input laser fiber can be inserted. Multiple inputs can be used, taking advantage of fiber couplers (in figure, yellow fibers on the right are coming from a 1x8 fiber coupler). A custom platform was designed in order to anchor the system to the microscope sample stage.

4.4.1 Grating scatterers

Once the package is ready, the scattered light distribution can be characterized, in order to check the generated light distribution on the surface of the chip (*spot*). We focused on the efficiency of the system in power delivery as well as on the spatial confinement of the light on the surface of the chip.

Power delivery

The measurements of the power delivery were performed on a package where the fiber array was aligned to the single scatterers matrix side. In this package some gratings are missing because of damaged connectors. The power delivered from each single scatterer was collected by a cleaved multimode fiber with 25 μm core diameter, angled by 15° (figure 4.18(a)). The total diameter of the fiber was 125 μm. The power collected by the fiber is normalized over an area of about the size of the spot on the surface (78.5 μm^2, 10 μm of diameter) in order to estimate the intensity received by a neuron. The intensity collected for each grating output considering an input power of 42 mW is shown in figure 4.18(c). These measurements were performed in air for the sake of simplicity: with water we were not able to see correctly the position of the fiber; the presence of water in principle should enhance the coupling because of a smaller index change in the light path through silica, water and quartz glass.
The values shown in figure 4.18(c) are calculated considering the maximum

power of the Cobolt laser (42 mW): the measurements were performed at lower power, measuring both the input (P_{in}) and the output power P_{out}, in order to get a value of efficiency of the system for each grating (figure 4.18(b)). Then, this efficiency was multiplied by the maximum input power available. First of all it can be seen that the efficiency and the power delivered by the scatterers is not even: this is due to a not perfect alignment and probably to the air bubbles in the glue mentioned before. Anyway, the intensity delivered by the vast majority of the gratings is bigger than $1\text{mW}/\text{mm}^2$, which is a value sufficient to excite our neurons, as will be shown in the next chapter.
These calculations refer to the ideal case in which the fiber is collecting all the light arriving at the input facet. Actually, it must be considered that the used fiber has a numerical aperture of 0.1, which implies that most of the scattered light is not collected. Due to experimental constraints, it was not possible to angle the fiber at a level of maximum coupling. Therefore, the measurements provide a low estimate of the scattered light power.

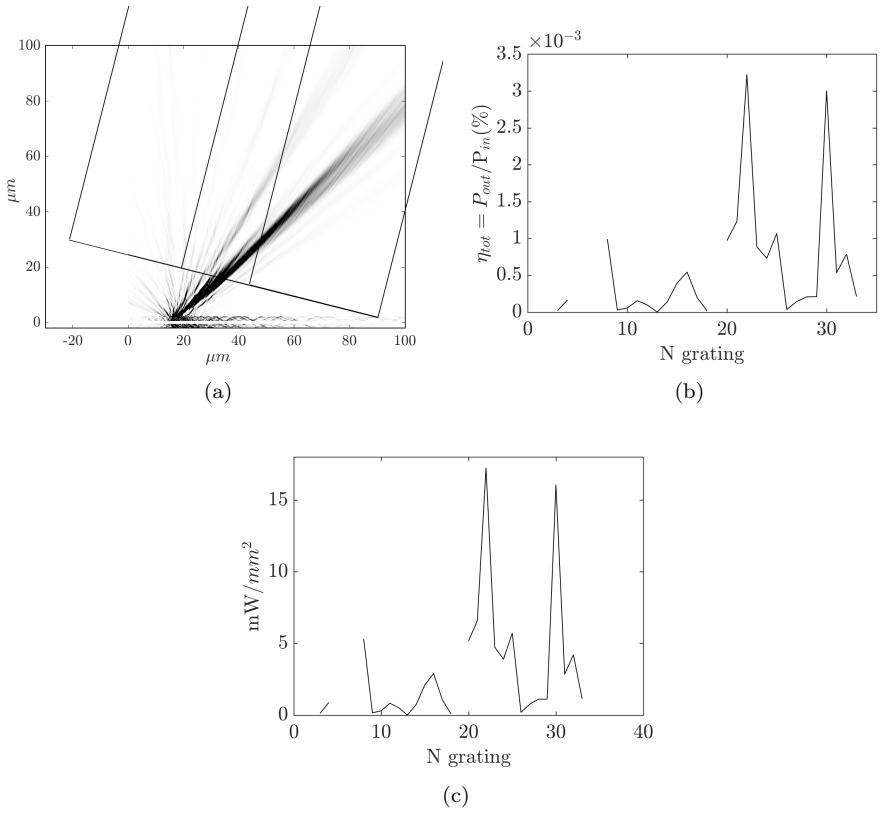

Figure 4.18: **Power calibration of the system.** (a) Sketch of the measurement system: the 2D profile of the scattered light is shown, and the fiber is representated at an angle of 15°. (b) The efficiency of the system measured for each scattering grating. (c) The intensity, computed on an area of 10 μm diameter, exiting from each scatterer.

Spatial confinement of light

To excite selectively single neurons, light must be confined in the desired place, in order to avoid the excitation of nearby cells. We thus performed the characterization of the distribution of light diffracted by the scatterers, comparing it with the FEM simulations. To do so, we analysed the spots created by the gratings under the microscope, with water inside the Petri dish, in order to resemble the scattering during the experiment. We used a 60x (LUMPLFLN60XW, NA 1, WD 2mm) objective, which has a numerical aperture (NA) big enough to detect at least the main beam scattered by our gratings: from the simulation, it is expected that the main beam is scattered with an angle of about 28°. In figure 4.19 images of the scattered light in far field are shown: figure 4.19(a) is a photo of the field scattered by the grating, inside a cube of agarose gel (3 %), with an input fiber aligned in butt coupling; figure 4.19(b) and 4.19(b) represent 2 spots created by gratings number 24 and 28 in the single scatterer matrix, seen by the microscope, with a 20x objective. It can be seen qualitatively how the light is well confined to the gratings.
To study the scattered light in the near field, we performed a stack measurement of the scattered light (grating number 32, figure 4.20(a)) at different y, acquiring 61 layers around the chip surface plane, with 1μm step. We thus analysed the acquired multi-tiff image in the following way. First of all, looking at the longitudinal profile of the spot (dashed red line in figure 4.20(b)), we computed how the width of the field was changing along the different planes. To define the width, we used the standard deviation Σ, defined as

$$\Sigma = [\langle z^2 \rangle - \langle z \rangle^2]^{1/2}, \tag{4.20}$$

where p=1,2, and

$$\langle z^p \rangle = \frac{\int_z z^p |E(z)|^2 dz}{\int_z |E(z)|^2 dz}. \tag{4.21}$$

We then identified the y=0 plane as the coordinate at which Σ value is minimum (see inset in figure 4.20(b)). Rescaling the y axis of the multi-tiff to this new 0, we could indentify the distance of the different planes from the grating, in μm. In figures 4.20(c) and 4.20(d) the simulated and measured scattered fields in the yz are shown, respectively. The two maps are similar, taking into account that the experimental resolution does not let the detection of all the interference fringes simulated and that the numerical aperture does not let the detection of rays scattered at angles larger than 48.8°. Moreover, the chip is not perfectly horizontal, due to the glue layers under it. It is worth to notice that in the measured map the focalization of the intensity is observed between 2 and 15 μm, which is where the neurons should lay.
We then focused our attention to the field distribution at y=5μm (figure 4.20(e)). The distributions are quite similar within the above cited limitations. In particular, the lateral fringes present in the simulated distribution (left), are not present in the measurement (right). In order to compare the Σ in these two distributions, we decided to calculate them within a z axis range at which the measured field is larger than 0.01. Doing so, we are sure that the presence of the not detected lateral fringes will not affect the Σ comparison. The field portions excluded in the calculation are shown in the figure as red. The Σ values got in the two cases are 3.4 and 3.3 respectively. We performed this calculation at

different planes between 0 and 30 μm, in order to evaluate the divergence of the scattered beam in the two cases. As shown in figure 4.20(f), the divergence behaviours are comparable. Then, we checked the spot reconstruction (figure 4.21(a)): also in this case, the measured spot resembles well the expected one, with a dimension of about 10x8 μm. Also their profiles along the x direction match well (figure 4.21(b)).
All considered, the realized aperiodic gratings work as predicted by the simulations, and are able to focalize the light in the desired planes as expected.

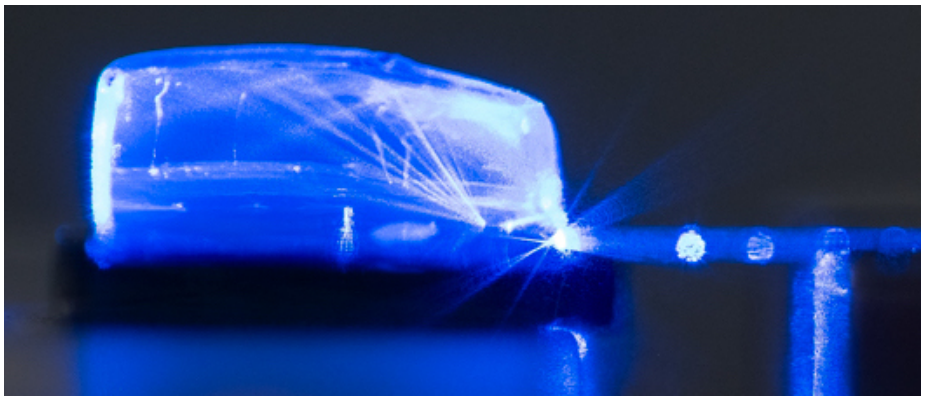

(a)

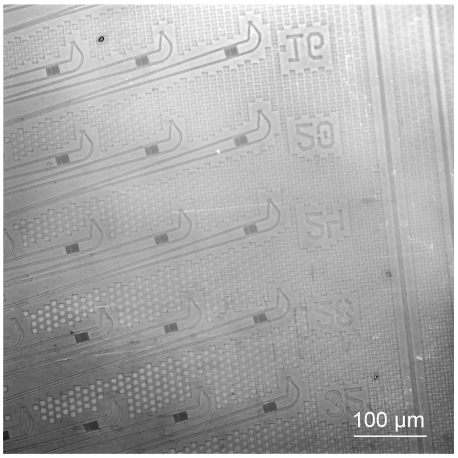

(b)

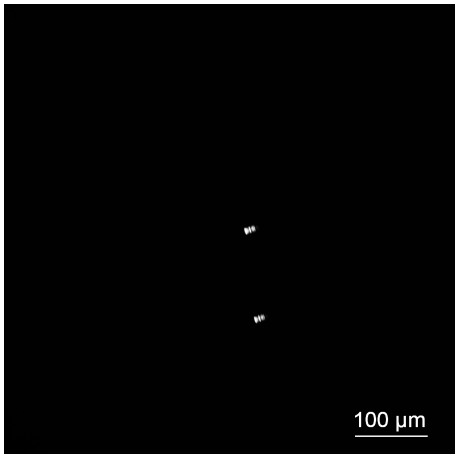

(c)

Figure 4.19: **Far field scattering.** (a) Photo of the field scattered by the grating, inside a cube of agarose gel (3 %), with a fiber aligned in butt coupling; (b) is the image taken with the microscope with a 20x objective of the single scatterer matrix; (c) shows the 2 spots created by grating number 24 and 28.

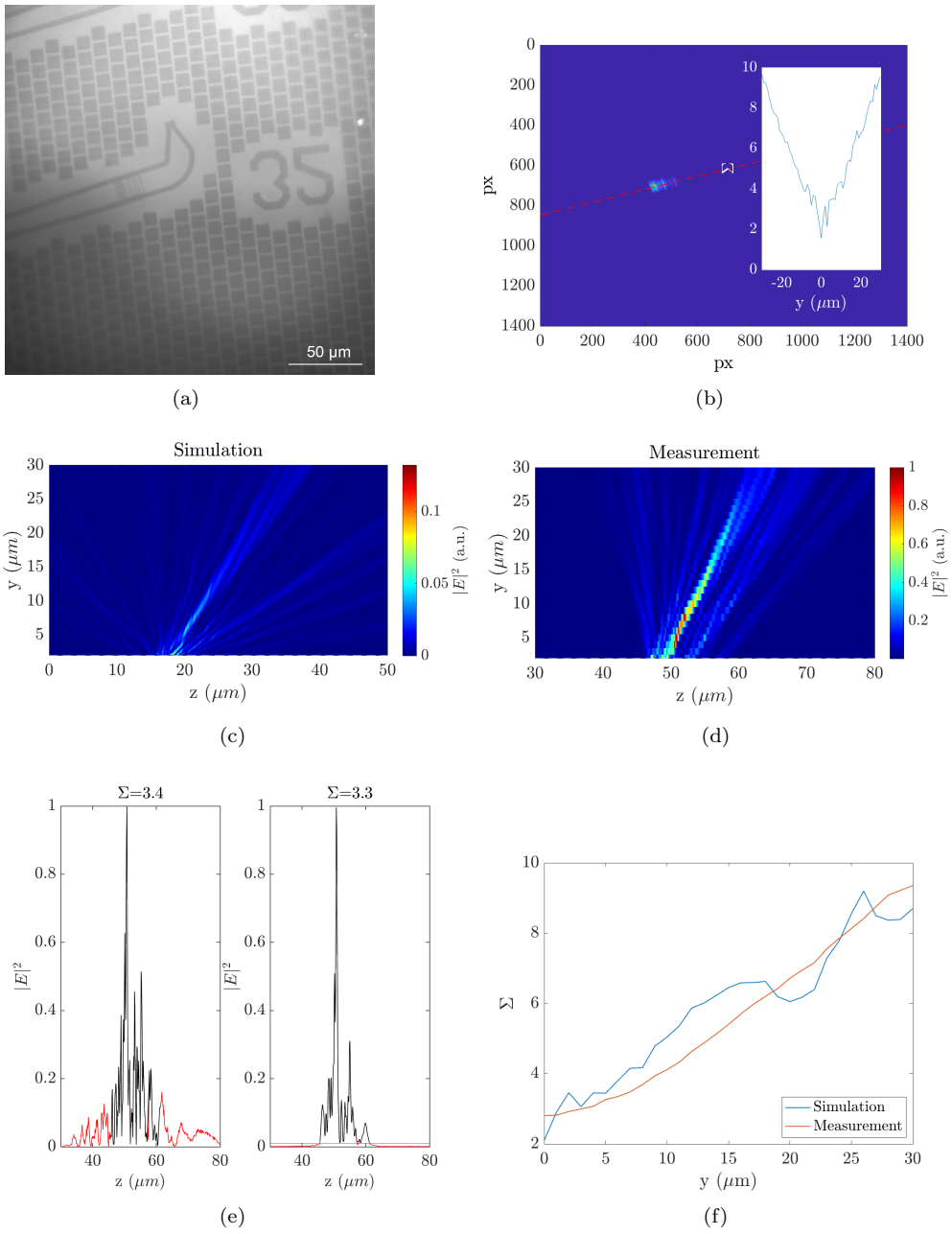

Figure 4.20: **Near field scattering.** (a) The grating on which the spot acquisition was performed, with a 60x objective; (b) One plane of the analysed image acquisition: the red line is the z direction considered in the analyses. The inset shows how Σ changes along the acquired planes; the minimum was fixed as plane y=0. (c) and (d) are the normalized scattering maps obtained in the simulation and in the measurement, respectively. (e) Field profiles along z in the simulated case (left) and in the measurement (right). Red portions are the one excluded in the computation of Σ. (f) comparison between the Σ values dependence along y direction.

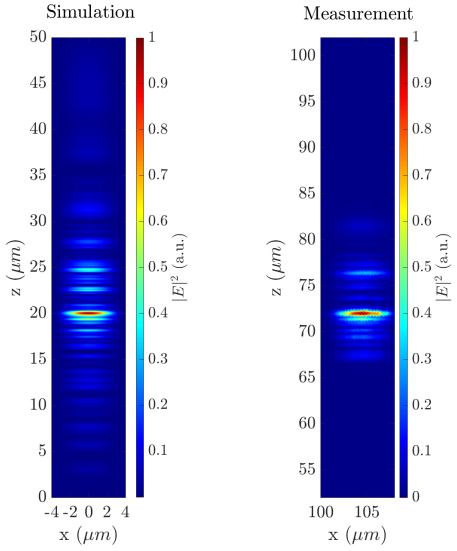

(a)

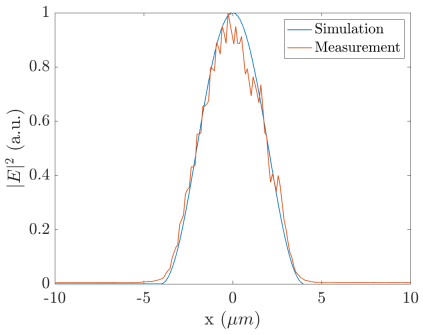

(b)

Figure 4.21: **Near field scattering.** (a) The normalized maps of the spots obtained in the simulation and in the measurement. (b) Comparison of the spot profiles along the x direction.

4.5 Package biocompatibility

To perform the experiments, neurons must be plated on the surface of the chip. Cortical neurons are prepared as described in section 5.3.1, plating them on the poli-L-Lysine coated surface of the chip. First of all we did some trials of plating neurons on the surface of bare chips, without the optical system aligned. As can be seen from figure 4.22, neurons can grow on the surface of our chips.

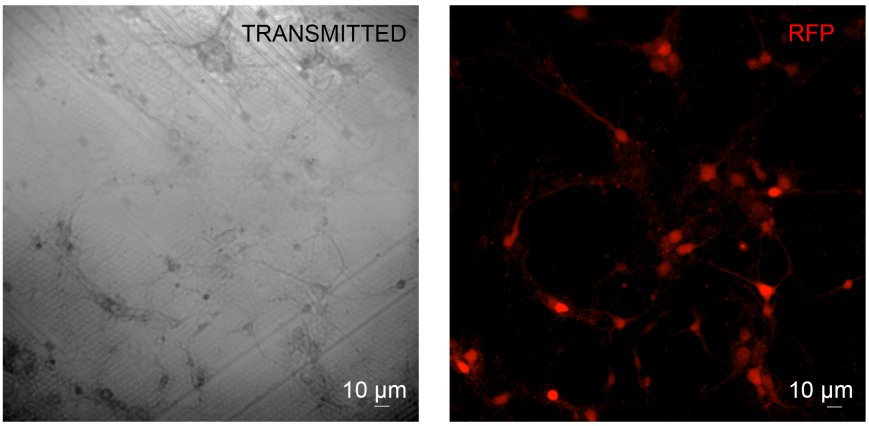

Figure 4.22: **Neurons plated on photonic chip.** Neurons plated on the bare chip after 12 days in vitro (DIV). On the left "transmitted image" taken by reflection of light on the surface of the photonic chip; for sake of visualization, neurons were also loaded with calcium indicator X-Rhod (RFP image).

To plate the cells on the chips in the whole package, we sterilized the system under UV light. Then, neurons are plated on the surface of the chip and the system is kept in sterile conditions inside the incubator (37°C, 5% CO_2) until 10 DIV. The humidity and temperature are supposed not to affect the optical system; anyway, to protect the metal connectors of the optical fibers, in the incubator all the system is shielded with aluminium wrap. At a first trial, the culture was found contaminated. We are currently performing some tests to understand the cause of this contamination: UV can in principle deteriorate the plastic parts of the system, and it can be replaced with sterilization in ethanol. Thus, we realized a second package, to be sterilized with ethanol, to check the UV hypothesis. Another possible source for contamination can be the presence of many layers inside the Petri dish: the spaces between glass, chip and fiber array can accumulate biological and saline waste, and it is difficult to clean them properly without affecting the optical alignment.

4.6 Summary and Discussion

In this chapter, the photonic platform for neuronal excitation was presented, from the design of the chip to the biocompatibility tests. The realized chip is able to create spots of blue light on its surface with the dimensions of a neuronal body, with an intensity >1 mW/mm^2, enough to perform optogenetic

excitation [16, 62, 76, 82, 123, 125, 139]. The scattering structures inside the chip consist in aperiodic gratings, designed with the *FEM enhanced Transfer matrix method* [138]. A fiber array is aligned to the chip and fixed in a portable package that allows its use under the microscope. Biocompatibility of the platform is currently under test.

There are several aspects that can be discussed about the design of the grating scatterers and the overall design of the system.
First of all we target a gaussian distribution of the scattered light during the optimization of the scattering structures: different targets could be chosen with the aim of neuronal excitation, for example a square one. The choice of the target must be done considering the optimization algorithm. In particular, if this distribution is expressed in the loss function of the optimizer, as in our case, the presence of a discontinuous distribution, like the square one, makes the optimization more difficult for the algorithm, and longer. We chose a gaussian distribution for the sake of simplicity. Nevertheless, after the design of the chip, we demonstrated that our algorithm can target as well a squared distribution [138].
To improve the overall efficiency, the symmetric scattering from the gratings can be reduced using a shallow etch configuration of the grating, instead of a full one, to force the scattering just in the upper part of the system.
In order to overcome possible contamination problems due to the deterioration of plastic parts inside the Petri dish, custom glass walls can be attached to the surface of the chip, to leave the coupling site far from the biological sample. To fabricate such a system, the photonic chip must be properly designed with a larger area, as in [92].
Waiting for the neurons to be plated on the surface of the chip, we also developed a different approach to perform neuronal excitation: the idea is to plate the neurons on cover glasses that can be placed on the chip, inside the Petri dish of the package. We performed some trials in this direction, but we were not able to record any neuronal response. Indeed, being the used cover glasses 100 μm thick, the intensity of the scattered light is very low on the new neuronal plane. At this height, the efficiency of the system, calculated as in equation 4.17, considering glass above the grating, drops down from 48%to 4%. The intensity shown in figure 4.18(c) is thus reduced to its 8%, and with it the probability to excite the neurons. However, this approach must be taken into consideration: the use of a single package for multiple cultures plated on glass coverslips ensures slower deterioration of the system and the possibility of performing many more experiments, saving a lot of experimental time.

Despite all these possible improvements, our system shows the possibility to selectively excite a neuronal cell with about 10 μm diameter body, with the proper intensity for optogenetic excitation/inhibition. The coupling with the optical fibers is robust and makes the system portable and easily coupled to a microscopy system.

Chapter 5

DLP

Waiting for the chip to be realized and characterized, we decided to begin biological optogenetics experiments on in-vitro cultures in order to set the experimental conditions using a more standard technique: the Digital Light Processing device (DLP).

5.1 Microscopy setup

The microscopy setup consists of a system provided by Crisel Instrumens Company, which includes a confocal spinning-disk module with an integrated Super Resolution module, based on structured illumination microscopy, in upright configuration. The system is equipped with 7 solid state LED sources that cover the spectrum from violet (395 nm) up to red (640 nm), arranged in the SPECTRA Light engine. As shown in figure 5.1, the light coming out from the SPECTRA (green lines in figures) is guided through an optical fiber to the super-resolution/confocal modules. Here, a dichroic filter selects the desired spectrum. Thanks to a mirror, the light is reflected down to the objective, which focalizes the light on the sample. If the sample has fluorescence indicators, the emitted light (red lines in figures) can be collected up by the objective, and, by the opposite optical path, arrives at a CMOS camera, passing through the dichroic mirror and other emission filter. The camera is a Prime BSI Back-Illuminated BSI Scientific sCMOS with 95% of quantum efficiency,with 2048x2048 pixels with $6.5\mu m$x$6.5\mu m$ pixel area. The system can be used in confocal mode, super-resolution mode or widefield (i.e. without confocal nor super resolution acquisition). For the confocal mode, there are two spinning disks with different pinhole patterns: one has 40 μm holes, and one has 70 μm ones. The disks can be inserted in the path or kept away. With spinning disk, the confocal resolution with 60x NA 1.4 oil immersion objective is $<$800nm. For the super-resolution mode there are many patterns of SIM (structured illumination microscopy) masks provided, whose interference with high frequency spatial details of the image lets the reconstruction of the final image with a lateral resolution of $\sim$120 nm and an axial resolution of $\sim$300 nm. The system is equipped with two water immersion objectives with 60x (LUMPLFLN60XW, NA 1, WD 2mm) and 20x magnification (UMPLFLN20XW, NA 0.5, WD 3.5mm), a 100x

immersion objective (UPLSAPO100XO, NA 1.4, WD 0.13 mm) and a dry long working distance 10x objective (LMPLFLN10XLWD, NA 0.25, WD 21mm). The control of the system and acquisition is performed through MetaMorph acquisition and analysis software.

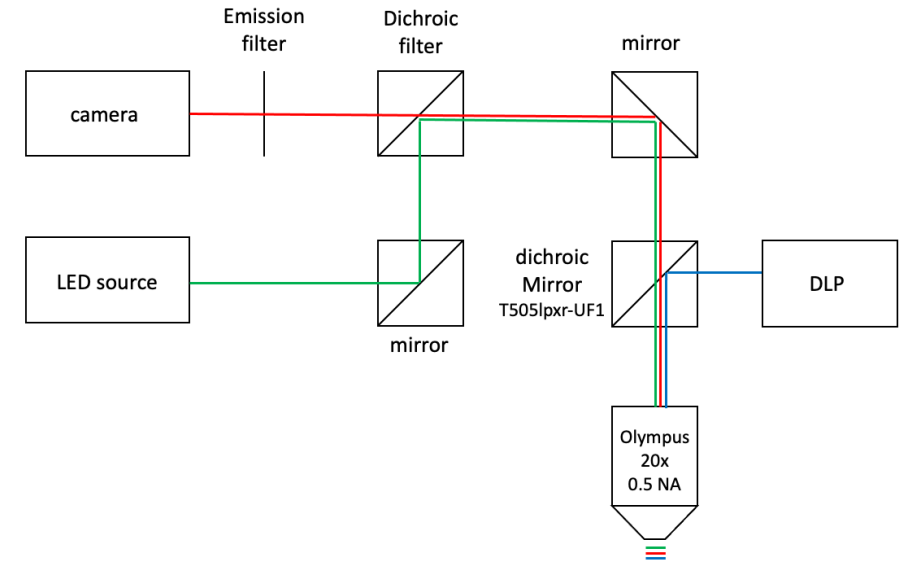

(a)

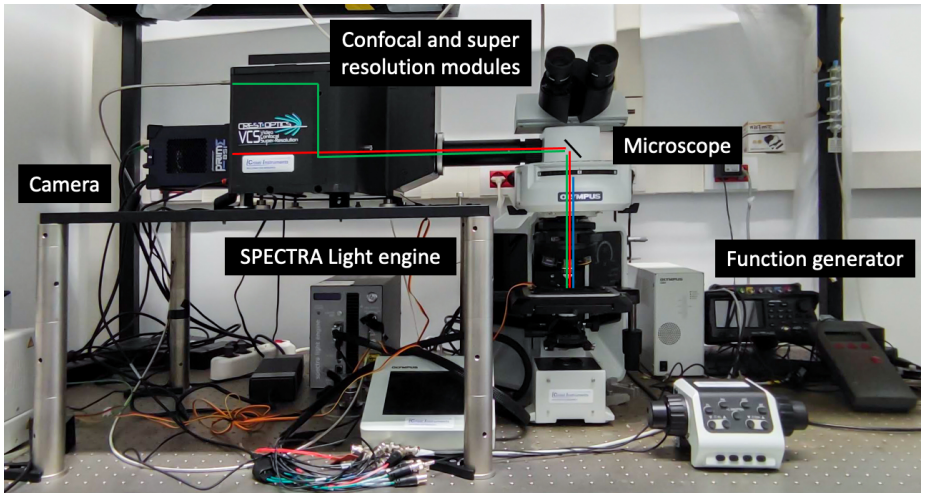

(b)

Figure 5.1: **Microscopy setup system.** (a) A scheme of the optical lines of the system. (b) A frontal view of the system. In green is represented the excitation light, in red the light emitted by the sample and in blue the light coming from the DLP.

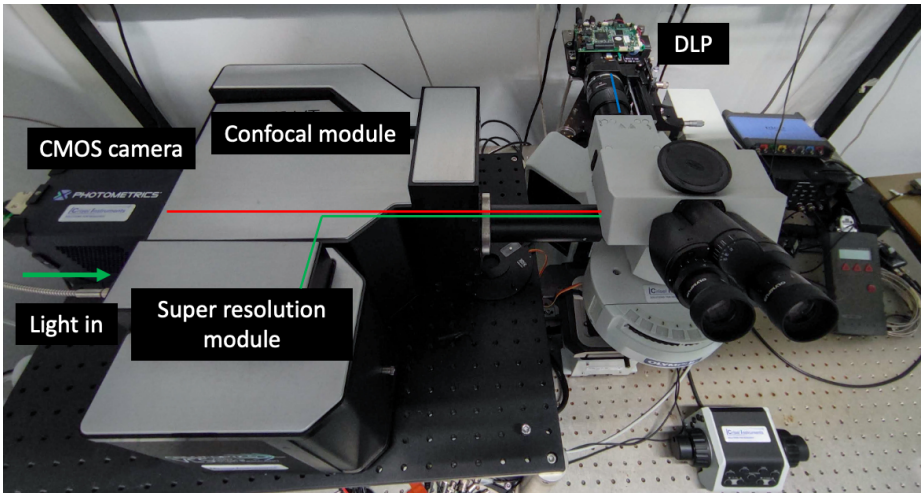

(a)

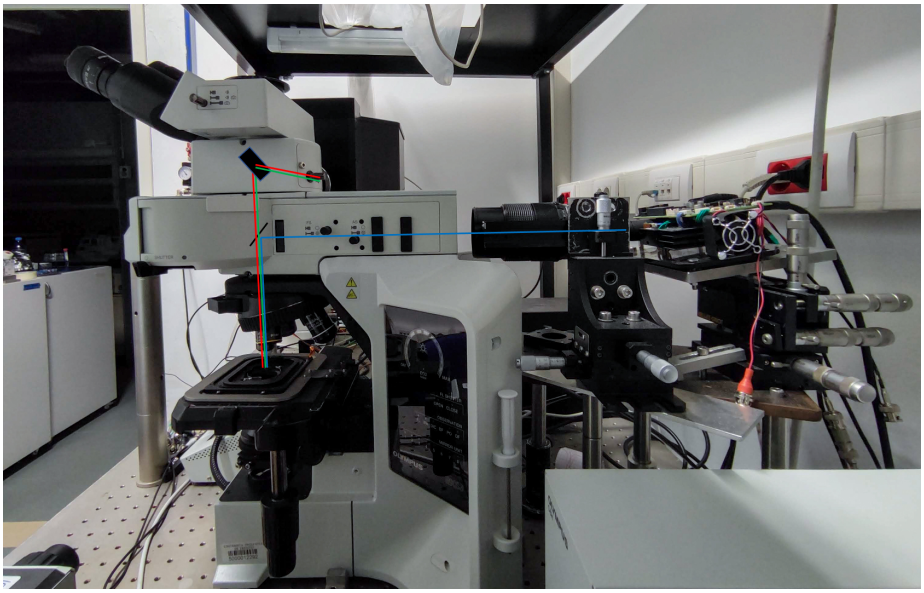

(b)

Figure 5.2: **Microscopy setup system.** A up (a) and lateral (b) views of the system. In green is represented the excitation light, in red the light emitted by the sample and in blue the light coming from the DLP.

5.2 DLP alignment and characterization

The DLP system was integrated with the microscpe set-up, taking advantage of a free entrance in the rear part of the system. The system is a DLP E4500, which includes 3 LEDs, optics, a WXGA DMD (Wide Extended Graphics Array Digital Micromirror Device) and a driver board. The light engine can produce approximately 150 lumens at 15 W LED power consumption. The blue LED (λ= 450 nm) that will be used in this work has a power of 600 mW. The light from the LEDs impinges on the DMD which has 1039680 mirrors arranged in 912 columns by 1140 rows with a diamond array configuration. Each of these mirrors has two possible inclinations that reflect the light in different directions. This system allows patternized illumination with preloaded and custom patterns that can be chosen through the DLP E4500 software. Moreover, these patterns can be pulsed in time, with both an internal or external trigger, with a minimum exposure time that goes from 235 μs to 8333 μs, depending on the bit depth of the projected image. The system supports 1-, 2-, 3-, 4-, 5-, 6-, 7-, and 8-bit images with a 912 columns $\times$ 1140 rows resolution. These images are pixel accurate, meaning that each pixel corresponds to a micromirror on the DMD. The light coming from the DLP system is collimated and aligned to the optical path of the microscope from the rear port of the system. As can be seen in figure 5.2(b), the DLP is positioned on a 5-axis stage, while a macro TAMRON 90mm AF2.5 objective is mounted on a 3-axis stage in order to collect the DLP light and create the desired image on the sample plane. The light is directed down to the sample thanks to a dichroic mirror (Chroma T505lpxr-UF1) which acts like a high-pass filter, reflecting all the wavelengths smaller than 505 nm. In this way, we can use the DLP and at the same time record signals at longer wavelengths. The alignment of the system was performed in order to obtain blue patterned illumination on the sample plane of the microscope, with high contrast and enough intensity to excite the neurons.

Image creation and loading

Images can be loaded inside the DLP's firmware, through its software. Due to the optical path before entering the microscope, only the light coming from a portion of the mirror matrix actually enters the microscope. Moreover, aberrations in the system distort the image proportions. This means that if a pattern is drawn in a 912$\times$1140 pixel image, only a portion of it will be projected down to the sample. To make the following more clear, let's focus on an example that will be useful to understand the following experiments. Suppose that we have a neuronal culture under the microscope, and we see an area of it in the field of view (FOV) of the objective. We want to excite just 2 neurons. In order to do so, we have to create an image with 2 spots exactly in the position of the chosen neurons. To create the proper image to load, the following procedure is performed. We created a standard mask with a grid with 100 pixel pitch, with numbers at each corner of the grid (Fig. 5.3(a)). When we project this image down to the sample plane, we are able to see which portion of the image is actually projected (Fig. 5.3(b)). Thus, we save this image through the microscope camera, and we upload it in a purposely developed program in MATLAB. Here, knowing the dimensions of the image and the projected numbers, we find the exact position and proportions of the FOV inside the bigger 912$\times$1140 matrix

of mirrors. Once the usable area is known, the desired pattern can be drawn inside it. In this way we can load the image of the neuronal network, draw the spot mask on it and put it in the proper position inside the bigger matrix to be sure that the spots will illuminate the desired neurons (Fig. 5.3(c)).

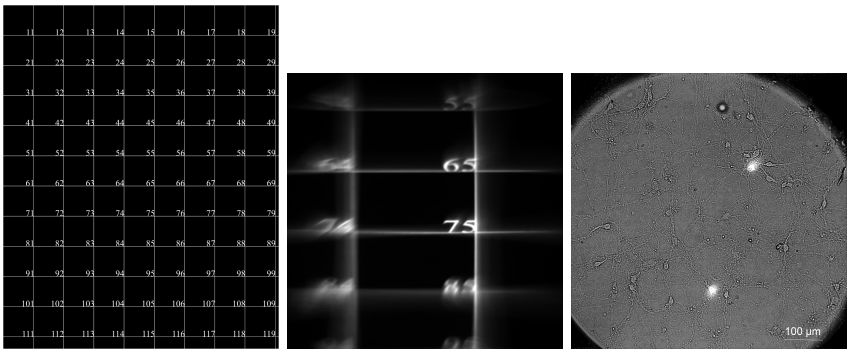

(a) (b) (c)

Figure 5.3: **Image creation.** (a) The calibration grid. (b) The portion of the grid projected on the sample plane, seen from the microscope objective. (c) 2 spots correctly located on 2 chosen neurons.

Power delivery

The optical power that arrives at the sample strongly depends on the relative alignment of the DLP and the objective, as well as on the focal length of the objective. Also, the power delivered from the LEDs can be changed, changing its driving current. The power can be measured under the microscope objectives, on the sample plane, with a power meter. Note that the 20x objective has a FOV of about 1 mm^2, while 10x objective of about 5 mm^2. Therefore, the measured values are the average values of light in the objective's FOV. In particular, this distribution is not flat, due to aberrations of the TAMRON and microscope's objectives and due to the not perfect alignment of the DLP system itself. If the distribution is not even, it means that once an operating power is selected from the LEDs, the neurons in different positions in the FOV will receive different intensity. The optogenetic excitation depends on light intensities: in our experiments we used ChR2 channelrhodopsin, which is excited with an intensity > 1 mW/mm^2 [16, 62, 76, 82, 123, 125, 139]. Clearly, the more intense the light, the more likely the neurons will be excited. But, if the intensity is too high, it can induce photoxicity and harm the cells [67, 74, 75]. Then, also a not flat distribution can be used, if light is sufficiently high; but in this way, the intensity on the maximum position can be too high and damage the culture. We tried then to correct the light distribution, compensating for the non-homogeneity by taking advantage of the possibility to load 8-bit depth images. To do so, the wide-field light intensity distribution on the sample plane is acquired: it is then loaded in the software and normalized. Once the desired pattern is created, it is normalized over the intensity: it means that the 8-bit image to be sent to the DLP will be less intense where the power delivery is higher and more intense where the opposite occurs. As can be seen in figure 5.4, in this way the light distribution is flattened.

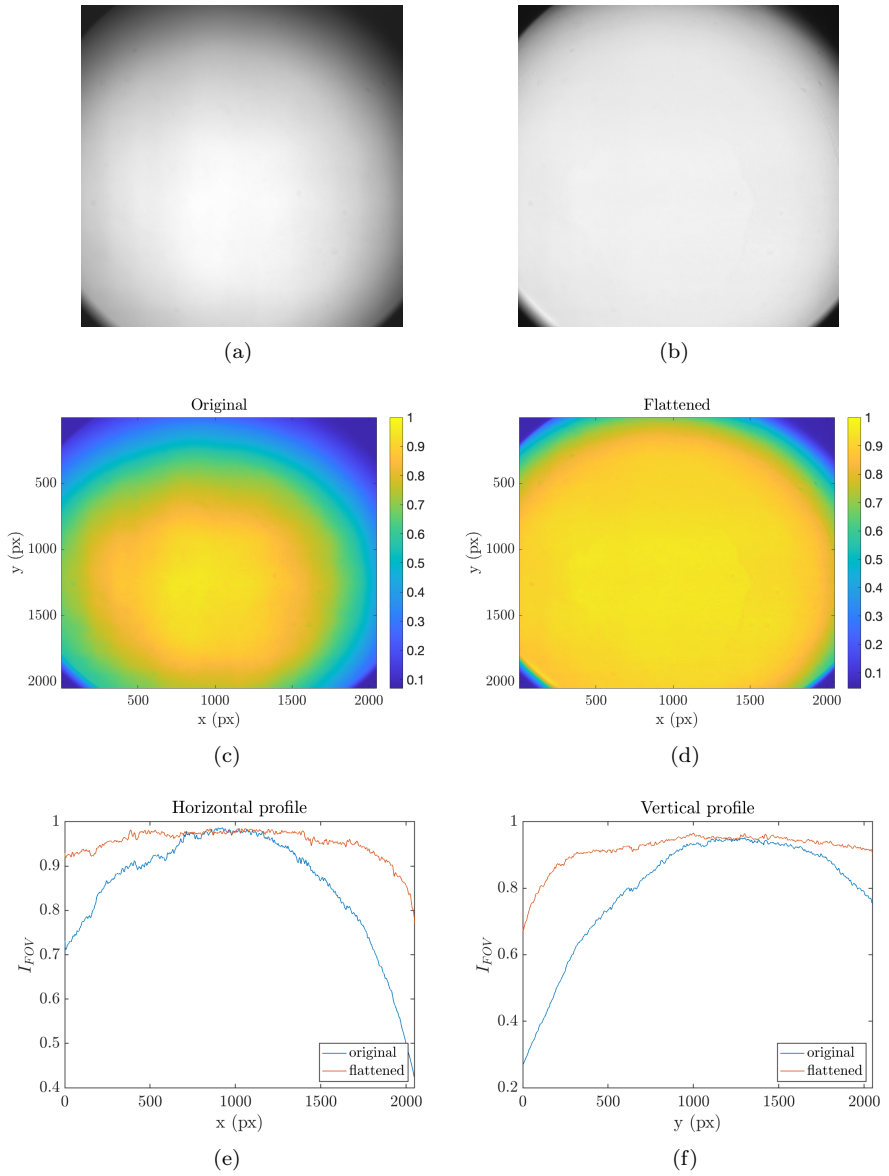

Figure 5.4: **Intensity distribution in the FOV.** (a) The intensity distribution as projected by the DLP, when all the mirrors are ON; (b) the corrected - flattened - light distribution. (c) and (d) are the normalized light distributions of the respective images of the above row. (e) an (f) are the line profiles of the light distribution at the middle of the image, in the horizontal and vertical direction, respectively: the blue curves are the original profiles, while the red ones, are those flattened.

Even if the intensity is uniform in the center part of the image, the borders are not well corrected. This is due to the fact that the DLP conversion of the 8-bit pixel values in intensity is not linear. To prove this hypothesis, we sent uniform images, each with different values of the pixels, to the DLP and we checked

the maximum projected intensity level on the acquired images. As can be seen in figure 5.5, the conversion is well fitted with a parabola: it means that the higher is the bit level, the less effective our correction will be. Anyway, at the border the intensity drops down by at most the 50% of the maximum, that is still enough to excite the neurons if a proper intensity value is chosen. Anyway, when possible, we avoided considering the neurons in the corners of the image. Once the new intensity profile is set, the average intensity is measured on the sample plane with a power meter, for different values of the LED current. To be sure that the intensity is enough in all the positions of the FOV, each time in the experiments a LED current was chosen that gives an average intensity of about 5-15 mW/mm^2.

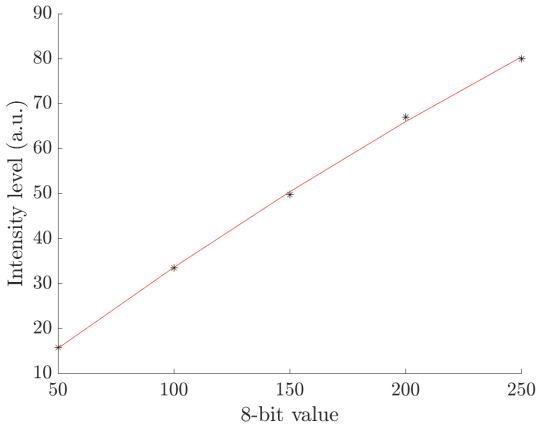

Figure 5.5: **DLP intensity conversion.** The graph shows the conversion from 8-bit values of the pixels and the projected maximum intensity, performed by the DLP. The red line is the fit performed with a parabola.

Contrast and resolution

In order to study the contrast and the resolution of the DLP system, we realized different images with single-pixel horizontal (and vertical) lines with increasing distance (10, 20, 30, 40 and 50 pixels). These images were loaded in the DLP and projected with the 20x objective on the sample plane. The sample was a silicon chip in a Petri dish, immersed in a water solution, to resemble the biological system. During the biological experiments neurons are usually plated on glass coverslips: we preferred to use a silicon chip for this characterization of the DLP system, so as to avoid the noise given by the multiple reflections that occur between the glass coverslip and the Petri dish. Indeed, we want to study the light arriving on the cells, whose body will change its transmission to the coverslip and the following diffusion. For this reason, we consider this light noise as a secondary effect on the cell, with respect to the direct light from the DLP, and we assume it as negligible.
Consider that, since DLP pixels have a diamond configuration, to create vertical or horizontal lines the system is switching ON the mirrors as shown in figure 5.6.

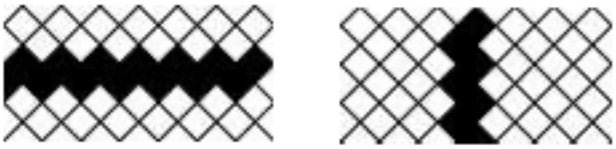

Figure 5.6: **DLP mirrors.** In the figure it is shown how vertical and horizontal lines are created by the DLP using the diamond configuration of pixels.

As can be seen in figures 5.7(a), due to aberrations of the optical system, the contrast and resolution of the image is not uniform over the FOV. For the horizontal (vertical) case, transverse profiles of the image were studied for 10 equally spaced positions in the vertical (horizontal) axis. As can be seen from figures 5.7(b), the profiles do not show perfectly sharp rectangular peaks, but they have a gaussian-like shape, with the intensity decreasing going far from the center of the line.

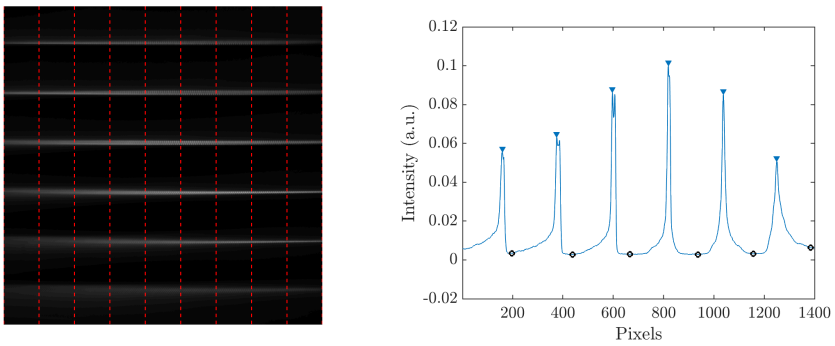

(a) (b)

Figure 5.7: **Analysis of the contrast.** (a) An example of one of the patterns analysed. The red lines represents the transverse lines on which profiles as (b) were obtained. In (b), the blue triangles represent the peaks maxima, and the black circles represent the minima.

For each peak, the contrast of the system was calculated as the ratio between the maximum of the peaks over the minimum that immediately follows (represented in figures with the black circles). This quantity gives the information about the minimum distance that must be kept between two illuminated points of the image: the nearer they are, the lower will be the contrast, since the spread of the intensity will sum, increasing the background intensity. The contrast values were calculated for all the peaks of each profile and plotted in the maps shown in figures 5.8 and 5.9, both for the vertical lines pattern and the horizontal one. In figure 5.10(a) is represented the average of the contrast obtained for each map, as a function of the distance d between the projected lines. As expected, the contrast increases with d. In particular, if the maximum values in each FOV is considered (Fig. 5.10(b)), the value of the contrast saturates for d>100 μm. This limit of the contrast is given by the background light coming from

the DLP. Given the high values of the contrast, this background is supposed negligible during cell excitation.
It can be seen that, to have a mean contrast bigger than 10, a distance bigger than 29 μm must be kept between two illuminated points. It must be considered that this value of distance is valid for the 20x objective. If a different magnification is used, this value in μm will change, accordingly.

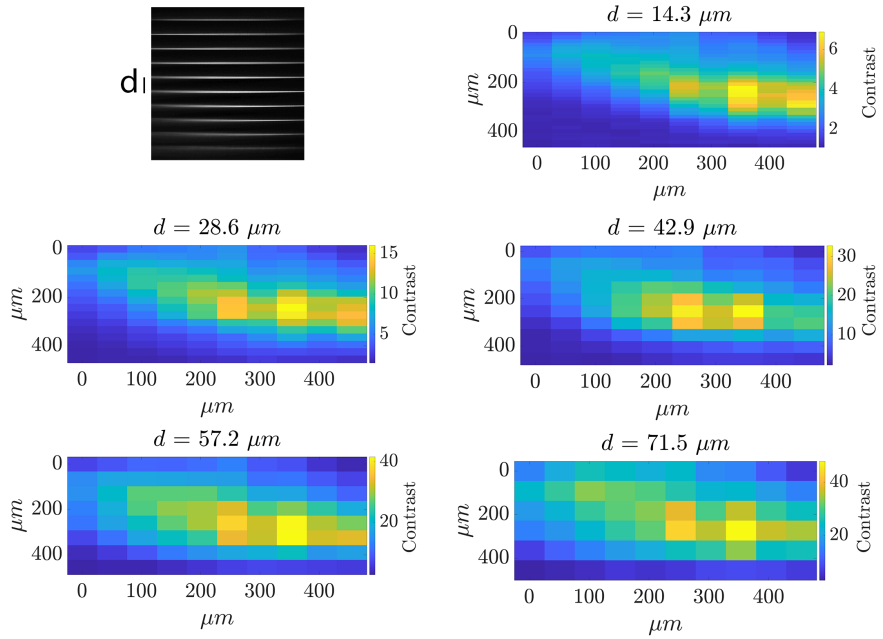

Figure 5.8: **Contrast maps - horizontal patterns.** In the image are shown the maps of contrast obtained in the FOV for the horizontal patterns, with different d distances between the lines.

Then, the same analysis was performed in order to study the resolution in the field of view. To avoid the contribution of the lower contrast at d<70 μm and to maximize the number of projected lines, we studied the patterns with d=71.5 μm and d=85.8 μm to study of the horizontal and vertical resolution, respectively. The resolution was computed as the full width half maximum (FWHM) of the peaks, after the subtraction of the baseline. In figure 5.11 are shown the maps of the resolution in the field of view for the horizontal (Fig. 5.11(a)) and vertical case (Fig. 5.11(b)). The resolution values go from 2.6 μm to 30 μm and from 4.3 μm to 36 μm in the horizontal and vertical case, respectively. We can thus say that the minimum resolution of the system is 3 $\pm$ 1 μm.

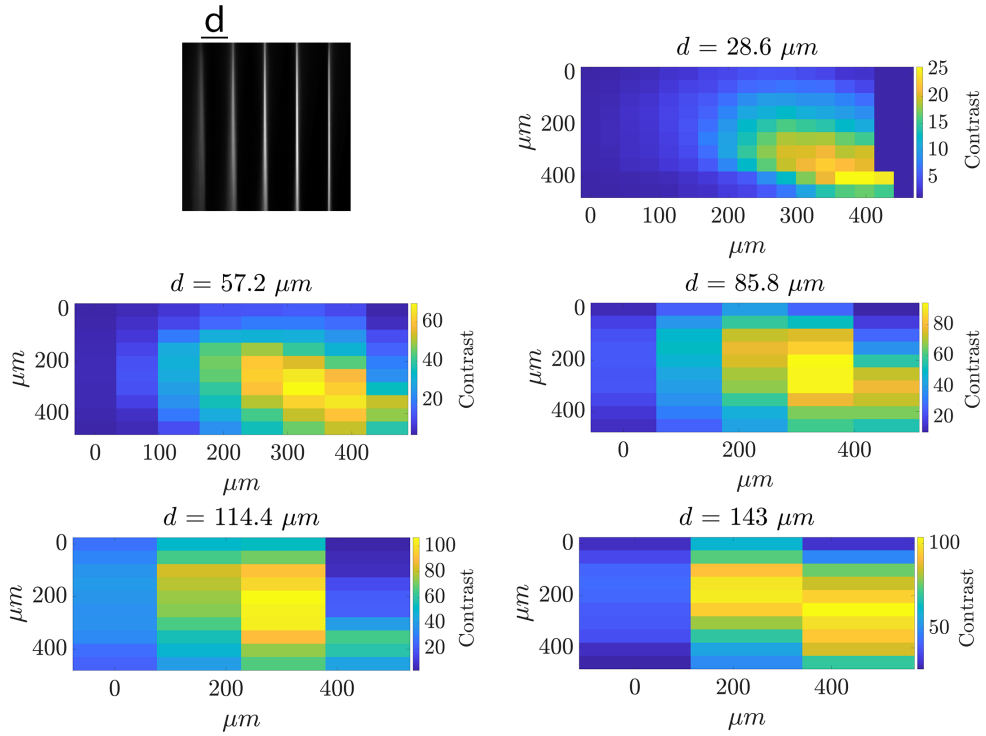

Figure 5.9: **Contrast maps - vertical patterns.** Maps of the contrast values obtained in the FOV for vertical patterns, with different d distances between the lines. In the vertical d=28.6 μm case, on the right edge are present some NaN values: these points represent peaks that were not studied because their maximum was very near to the edge of the image. Indeed in this case it was not possible to compute correctly the contrast in that specific position in the FOV.

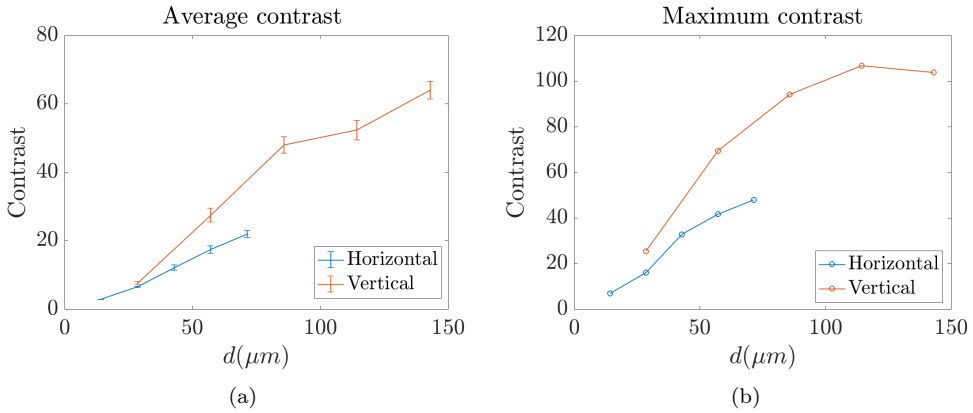

Figure 5.10: **Analysis of contrast maps.** (a) The average of the contrast values in the FOV, for the different patterns, in function of d. The error bars represent the standard errors. (b) The maximum of the contrast values in the FOV, for the different patterns, in function of d.

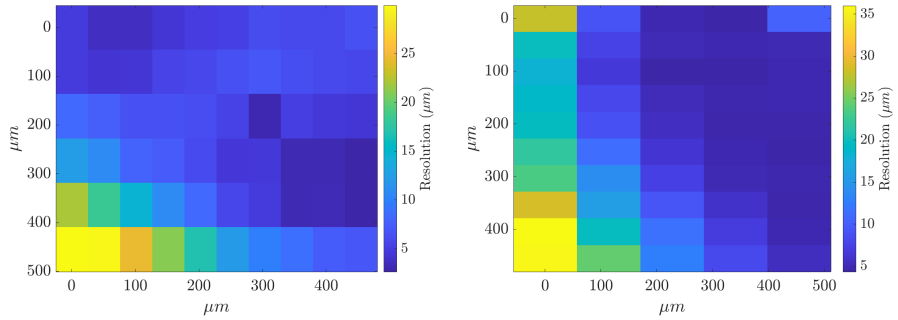

Figure 5.11: **Resolution maps.** (a) The resolution map in the field of view for the horizontal line pattern with d= 71.5 μm; (b) The resolution map in the field of view for the vertical line pattern with d= 85.5 μm;

Creating a spot pattern

In order to excite single neurons, spots can be created in desired positions. For the measurements presented in this work, we used spots of 13 pixels of diameter in the original image loaded to the DLP. To check the corresponding area of influence of the light excitation, we analysed the spots in different positions inside the FOV (fig. 5.12). Considering the maximum intensity over all the spots created, we assumed a minimum threshold of 10% of the maximum in order to obtain their area of influence. The dimensions of the obtained regions change between 58 and 144 pixels (19-47 μm with the 20x objective); their areas change between 300 and 700 μm^2.

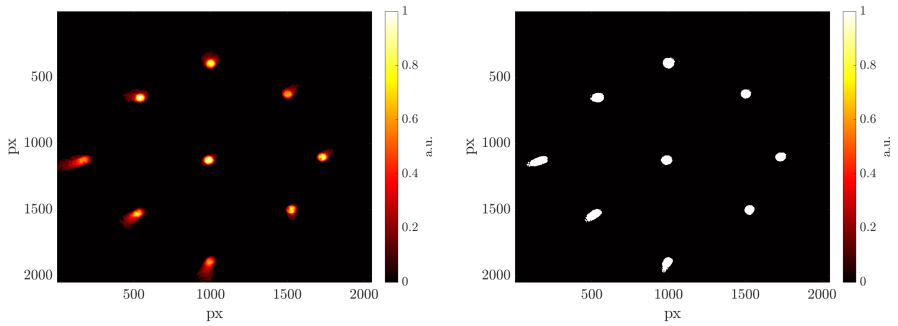

Figure 5.12: **Analysis of spot dimensions in FOV.** On the left are shown some spots projected in different positions of the FOV; on the right is shown the elaborated image with the actual regions influenced by the spots, with an intensity bigger than 10% of the maximum.

Consideration on the area of illumination

With the camera we can record a full image, using the whole sensor, or a crop. Actually, we must consider that even if a full view is used, what is seen is not

the entire FOV of the objective. Indeed, due to mechanical reasons, the optical fitting of the tube before the confocal module cuts out the outer part of the optical beam. For this reason, when the full view configuration is used, in the images black corners are visible. The visible FOV has a diameter of 800 μm and 1350 μm with the 20x and 10x objectives, respectively. This means that when we illuminate, light also arrives on neurons out of the FOV that we are imaging. Measuring the light distribution on the sample plane with a beam profiler (CinCam CMOS-1201), we can say that the unseen area is an annulus $200\mu m$ thick with 20x objective and $700\mu m$ thick with 10x objective. For this reason, when we want to illuminate the entire field of view with the DLP during the experiments, we decided not to use the entire DLP mirror matrix to project the light. Instead, we create a square confined to the visible FOV. In this way, during the biological experiments, we are sure to illuminate (i.e. excite) only the network visible from the camera. Doing so, the illuminated area will be 0.64 mm^2 and 1.8 mm^2 large, with the 20x and 10x objectives, respectively.

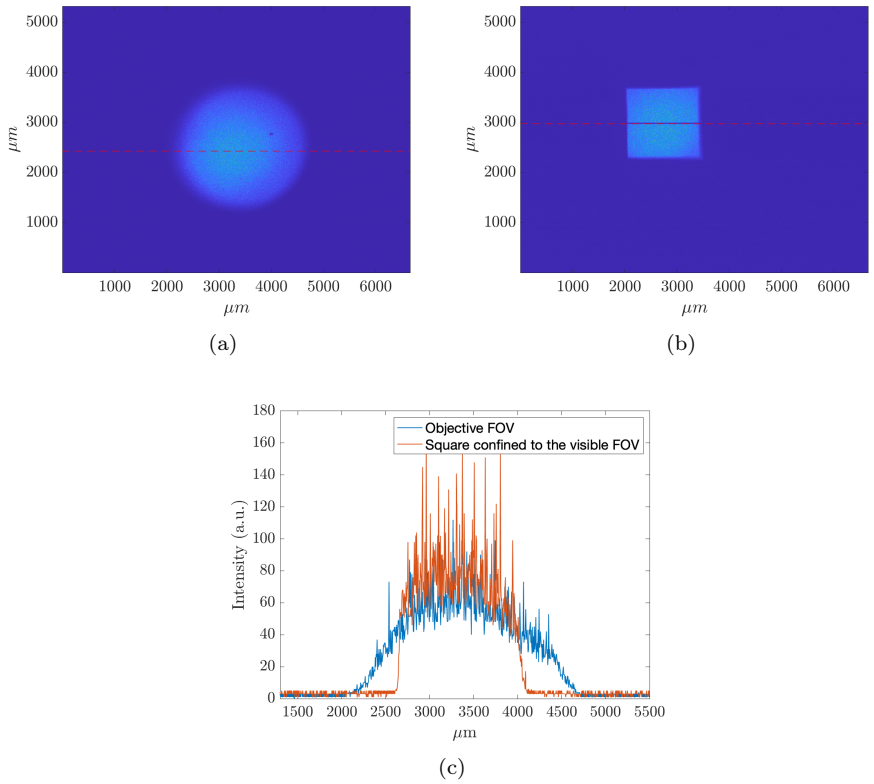

Figure 5.13: **Measurement of the area of illumination.** The light distribution measured with a beam profiler (CinCam CMOS-1201) under the 10x objective, in the case of the illumination with all the DLP mirrors (a) and in the case of the projection of a rectangle that matches the dimension of the FOV visible form the microscope setup camera. (c) The comparison between the profiles along the red lines of figure (a) and (b).

5.3 Neuronal excitation through DLP

Once the DLP system was aligned and characterized, we performed the first experiments in order to optogenetically excite the neurons. In these sections I will explain the main experimental procedures to perform neuronal excitation and the reading of the neuronal activity through calcium indicator fluorescence.

5.3.1 Cell preparation

Cortical and hippocampal neuronal cultures were prepared from wild type mice (C57Bl6) embryos at 17.5 embryonic days (E17.5 days). Cortices and hippocampi were dissected from embryonic brains and incubated for 20 min at 37°C in Trypsin/EDTA 0.25%. Cells were dissociated with a plastic pipette, collected by centrifugation (800 RPM, 5 min) and resuspended in Neurobasal supplemented with B27-supplement and Penicillin/Streptomycin/Glutamine, plated on poli-L-Lysine coated glass coverslips and infected with adenoviral vector pAAV-Syn-ChR2(H134R)-YFP at days in vitro (DIV) 4-5. We performed the experiments starting from 10 - 11 DIV, when the network is sufficiently developed and the virus is correctly expressed in virtually all neurons.

5.3.2 Calcium experiments

To prove that the DLP system is able to optogenetically excite neuronal culture, we performed optical calcium recording. Cells were loaded with the chemical fluorescent calcium indicator X-Rhod-1AM, whose excitation and emission peaks are around 580 nm and 603 nm respectively [160–163], allowing its usage in combination with ChR2 excitation at 450 nm. X-Rhod-1AM is a membrane impermeable chemical indicator engineered with acetoxymethyl (AM) esters, allowing the passage of the dye through the membrane. Once inside the cell, esterases can cleave the AM group and trap the dye inside the cells. $Ca2^{+}$ indicators bind and interact just with free diffusible $Ca2^{+}$ ions. Calcium ions flux inside the cell and its subcellular compartments determine a large variety of functions. For example, in presynaptic terminals calcium influx triggers the exocytosis of synaptic vesicles and, then, the release of neurotransmitters; in postsynaptic terminals, calcium plays an important role in synaptic plasticity; in the nucleus, calcium signals can regulate gene transcription [61, 164]. It must be noticed that Ca^{2+} indicators act like Ca^{2+} buffers and can then impact the level and kinetics of Ca^{2+} within cells. The X-Rhod-1AM (1μM) was applied to cells in HBSS, Ca2Cl (2mM) and MgCl (1mM) bath at 37°C for 30 minutes and then washed with HBSS, Ca2Cl (2mM) and MgCl (1mM) at 37°C. 30 minutes after washing, coverslips were placed under microscope in a 35 mm dish with HBSS, Ca2Cl (2mM) and MgCl (1mM).

5.3.3 Experimental setup

In order to perform the experiments, two optical lines of excitation (580 nm for X-Rhod-1AM and 450 nm for ChR2) and one reading line (603 nm for X-Rhod-1AM emission spectrum) were needed. The different wavelengths were selected through dichroic mirrors and band pass filters as shown in figure 5.14. We will refer to the different filter configurations with the term *RFP configuration* for

the excitation and acquisition of X-Rhod-1AM signal and *YFP configuration* for the acquisition of the reporter for ChR2 infection. To avoid artefacts due to the reading of blue excitation light by the camera during the acquisition, we triggered our system as represented in figure 5.14: a BNC breakout cable gives access to different status of the camera and trigger options, among which the "Read out" output of the camera indicates that the camera is currently digitizing. Thus, we decided to connect this output of the camera to the trigger-in port of the DLP. In the DLP software we selected the external negative trigger option, with a pattern of 20 ms long pulses, with a frequency of 3Hz. First of all, we check the health of the neuronal culture in transmitted light, while in YFP and RFP configurations we check the correct infection with ChR2 and loading of X-Rhod-1AM respectively 5.15. Through Metamorph software we set up a timelapse acquisition with 1.5 Hz frequency. Doing so, when the camera finishes to acquire one frame, the DLP starts two pulses of stimulation pattern and the camera does not acquire while the DLP light is ON. The DLP pattern can be switched ON and OFF manually: for each acquisition we wait about 100 frames (=66 seconds) of background acquisition, then we switch ON the DLP pattern for 20 frames (13 seconds, 40 pulses in total) and eventually we continue recording for a total of 300 frames. Images are saved in multi-tiff format and analysed using MATLAB.

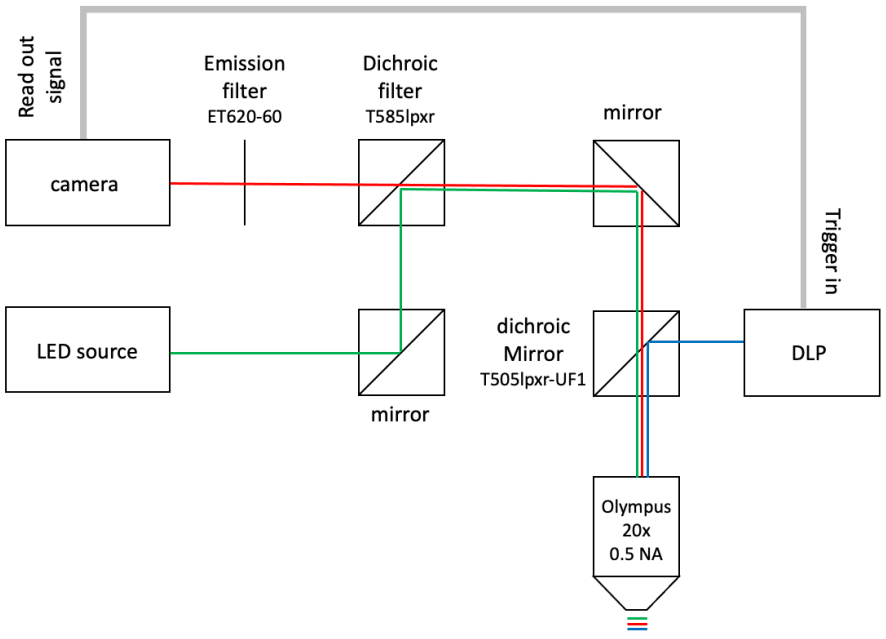

Figure 5.14: **Optical setup for calcium experiments.** To acquire the images of X-Rhod-1AM signal, we used the RFP configuration: the green LED (550 nm) excites the sample and red light is collected, filtered with a bandpass filter and brought to camera. The optogenetic excitation was performed with blue light coming from the DLP, reflected to the sample thanks to a dichroic mirror. The camera and the DLP were triggered in order to avoid artefacts in measurements.

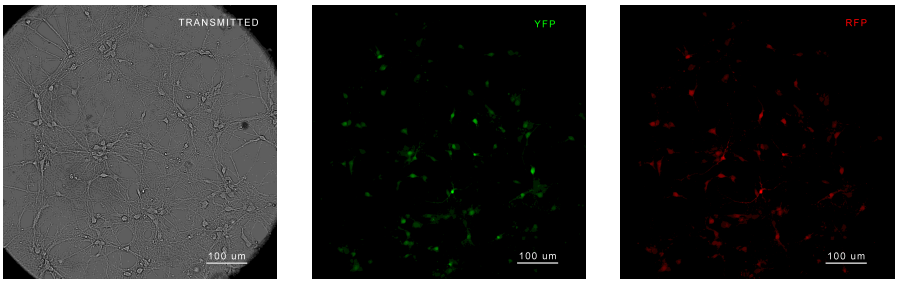

Figure 5.15: **Images of the sample before the calcium experiments.** A culture imaged with the 20x objective in transmitted light (left), YFP configuration (center) and RFP configuration (right). These images were taken without cropping the image.

5.3.4 Signal analysis

In the literature, there are many works on the analysis of calcium indicators signals to understand the neuronal network behaviour [83, 165–173]. Since in these experiments there are many neurons involved, an automatic analysis of the recorder images saves time and allows a better understanding. At base of many analysis software, there are these steps:

- automatic localization of the neurons in images;
- reconstruction of time traces of the signals and their analysis;
- possible reconstruction from signal traces of the connectivity of the network.

For our purposes, we focused on the first two points. To find neuronal soma in the images, different approaches can be used. In [170], they compare the temporal co-variation of the intensity of nearby pixels in order to identify single sources of calcium signals. The problem of this technique is that cells that do not spike can not be localized, and cells that spike together are detected as a single big cell. In [172], top-hat filtering and contrast adjustments are applied to the image. Then, *imfindcircles* MATLAB function was used to detect all circular elements inside the image for each frame, and all the masks were overlapped by an OR operation. Also more sophisticated analyses can be applied: in [165], a difference of Gaussian filters is used to distinguish the regions of interest (ROIs) from background, while in [173] it is estimated the correlation between the pixels' intensity signals within a user-defined euclidean distance. Then, there are commercial softwares like Imagej that implement many different methods [171]. Once the ROIs are found, fluorescence events can be analysed. First of all the pixels of each ROI are averaged to give a single time signal. Then, known the time window of the excitation event, the quantity $\Delta F/F_{rest}$ with $\Delta F = F_{peak} - F_{rest}$ is calculated, where F_{peak} is the maximum of the fluorescence event and F_{rest} is an average of the fluorescence values before the excitation. Different analyses can also be performed in order to subtract the baseline signal and study the temporal decay of fluorescence signals [172]. To be sure to correctly detect the signals and not simply noise, different methods can be used, like percentile based methods, wavelet transforms, machine learning methods, correlation with "standard" calcium transient waveform [167]. In [165], the rate of change in

brightness and a thresholding were used to identify calcium spikes, while in [170] built-in Matlab functions are used for spike detection and select just spikes exceeding a defined value above the average resting signal. In order to have direct control over the analysis process of the data, we implemented our own analysis in MATLAB. Automatized processes, if desired, can be stopped by the user to check the correct ROI selection and trace analysis.

Finding ROIs

After importing the multi-tiff images, we start localizing neurons in the FOV. To do this, we created an image as the average of all the frames before the excitation (Fig. 5.16(a)), and we divide the intensity range of the image in a finite number of levels (50 in our case). Then, we use these levels as a minimum threshold to create a binary image. This image presents a lot of individual areas, some correctly located above neuronal bodies, others on processes or outside the cells. Thus, on this binary image we use the *regionprops* Matlab function to get information about the regions found, like area, centroid, minimum and maximum axes, the proportion between the axes, the list of the pixels and the maximum of the intensity. Then, we impose some conditions on these parameters in order to select just the correct regions that will become our ROIs. Since we are performing this analysis for each intensity level, we filter duplicates looking at the distance between the centroids of the ROIs. Then, the user is asked to check the found ROIs and to select those that are not correct: in order not to miss neurons, we decided to use less restricted thresholds in the previous steps and leave the user to clear the found ROIs. Another way could be to restrict the conditions with the possibility that some neurons will be missing. In case a spotted illumination is performed, also the centroids of the spots are saved. In figure 5.16(b), representative centroids of the final ROIs are shown.

Trace analysis

Then, for each frame of the multi-tiff images, the pixels' intensity average of each ROI is computed in order to get the trace of the calcium fluorescence in time (Fig. 5.16(c)). The raw traces, the positions of the ROIs and the position of the spots allow to perform the desired analysis on the calcium responses of the neuronal network after a given stimulation. We used two different kinds of excitation of the neuronal networks: illumination of one half of the culture (*half-field illumination*), and spot illumination, with different numbers of spots. For both these cases, the traces were analysed in order to find the calcium spikes, compute the $\Delta F/F_{rest}$ (*intensity response*) and, eventually, classify them by their shape. First of all, for each trace, we interpolated data until the first frame of excitation. We then normalized the entire trace to this interpolation line in order to flatten the baseline. On the normalized trace we can then compute different parameters:

- $\Delta F/F_{rest}$: where ΔF is given by the maximum point in the time window of the excitation minus the value of the trace just before the start of the stimulation, while F_{rest} is the average of 50 frames before the excitation. We will refer to this quantity as *response intensity*;
- Σ: is the maximum absolute variation of the trace before the stimulus;

- $corr_{std}$: the correlation of the trace with a spike-shape trace (increase of fluorescence and then decrease to the basal level as shown in figure 5.17)
- $corr_{sat}$: the correlation of the trace with a saturated-shape trace (the fluorescence level remains high after the stimulation as shown in figure 5.17)

Looking at these values, different thresholds can be imposed in order to select which ones are responses and which ones are not. In the examples reported in figure 5.17, we decided to consider as responses the traces with a $\Delta F/F_{rest}$ >0.003 and $\frac{\Delta F/F_{rest}}{\Sigma}$ >1.5. This last condition ensures that what is considered response is higher than possible oscillations of the fluorescence before the stimulation. As shown in figure 5.17, some of our traces have a spike like behaviour, while others do not come back to the baseline level, but keep a high level of fluorescence; some others have a shape which is between these two. We think that this behaviour is mainly due to the indicator that holds calcium and does not release it during the acquisition time. Since we are interested in neuron response and not in its kinetic, we decided to consider as responses all the traces that at the time of the stimulation show a big discontinuity. Traces are then selected with thresholding. Another useful analysis that can be performed is to compute the calcium response in the image, pixel by pixel: in this way it is possible to see the response of both the neuronal bodies and the cell processes. This analysis consists in getting the calcium trace of each pixel of the image along all the frames of the multi-tiff. Then, on these traces we perform the same analysis that was just explained, and plot in a 2D image the value obtained from the trace of each pixel. In figure 5.18 an example is shown: here the response intensity value was plotted, pixel by pixel. On the left, the level of infection with ChR2 of the cells through the fluorescence intensity of YFP is shown. Of the 6 illuminated cells, one - on the bottom left of the image - seems less infected and, indeed, it does not show excitation by the spot. However, also other illuminated cells do not respond even though a high level of infection is assessed. In addition, some not illuminated cells show a signal. All these aspects will be discussed in the next paragraphs.

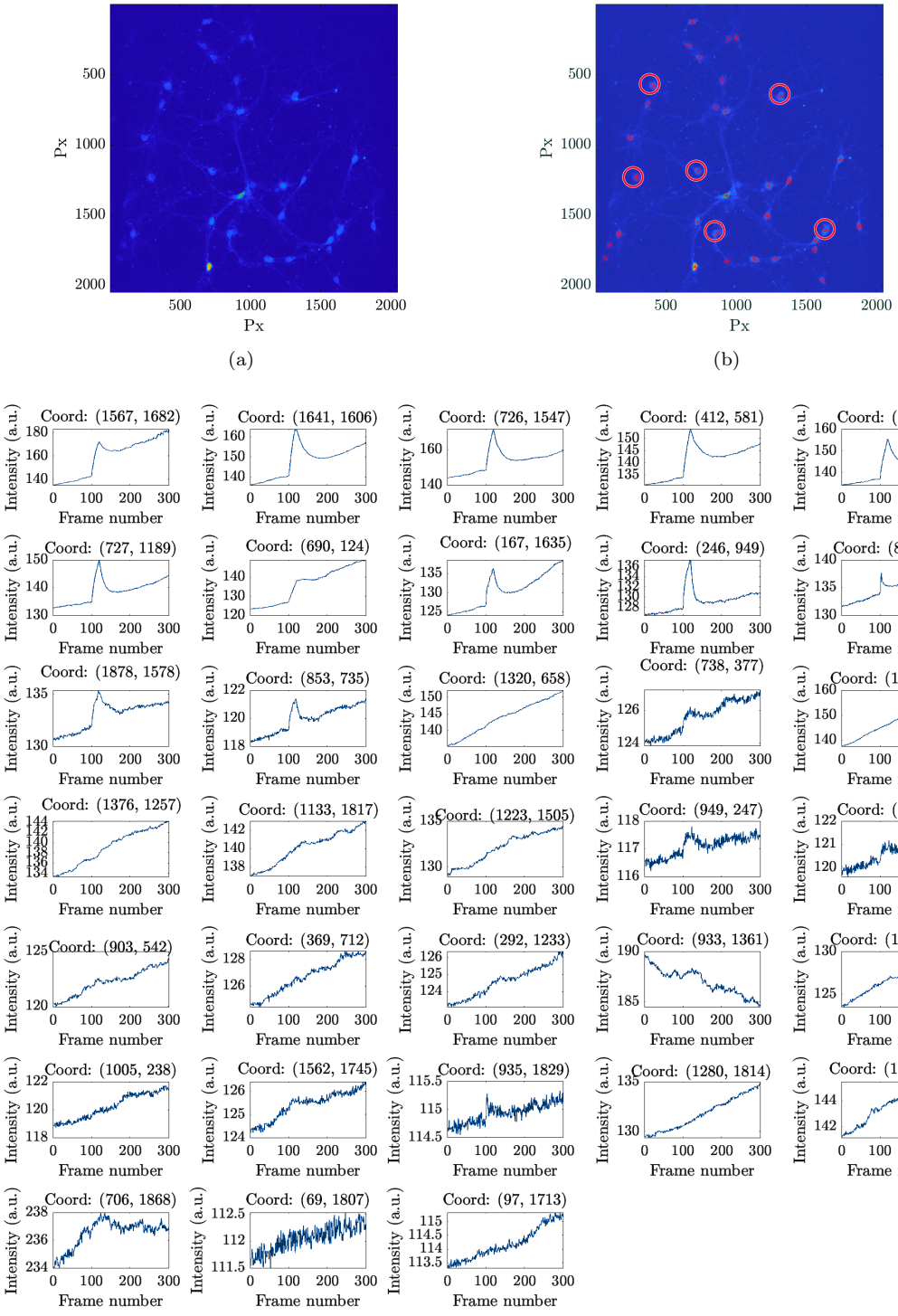

Figure 5.16: **Analysis of the acquired images.** (a) The image average of the frames before the excitation, used to perform ROIs localization. (b) The analysed image, with the centroids of the ROIs and the position of the excitation spots. (c) Raw traces extracted from the ROIs.

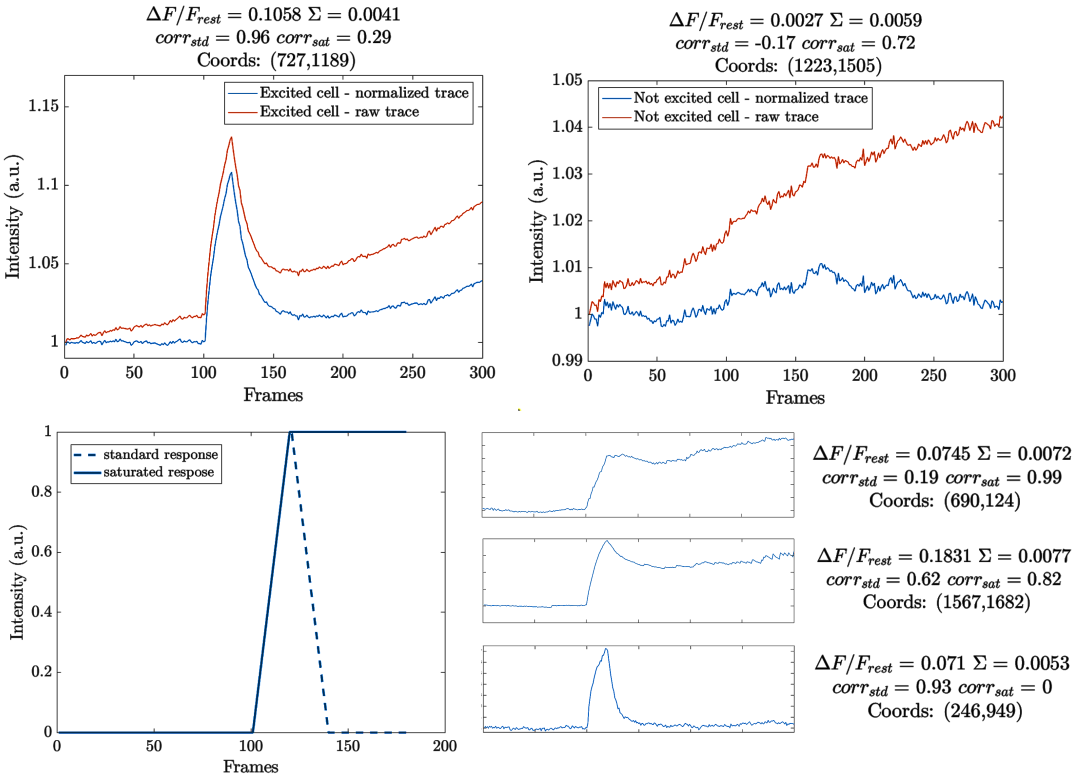

Figure 5.17: **Example of trace analysis.** In the upper part are shown the raw (red lines) and normalized (blue lines) traces of a responding and excited neuron, and one of a not responding neuron. For each trace, the values of $\Delta F/F_{rest}$, Σ, $corr_{std}$ and $corr_{sat}$ are shown. In the lower part, the reference traces of a standard (dashed line) and of a saturated (continuous line) response are shown. On the right there are examples of standard or saturated traces with the computed $\Delta F/F_{rest}$, $Sigma$, $corr_{std}$ and $corr_{sat}$ values.

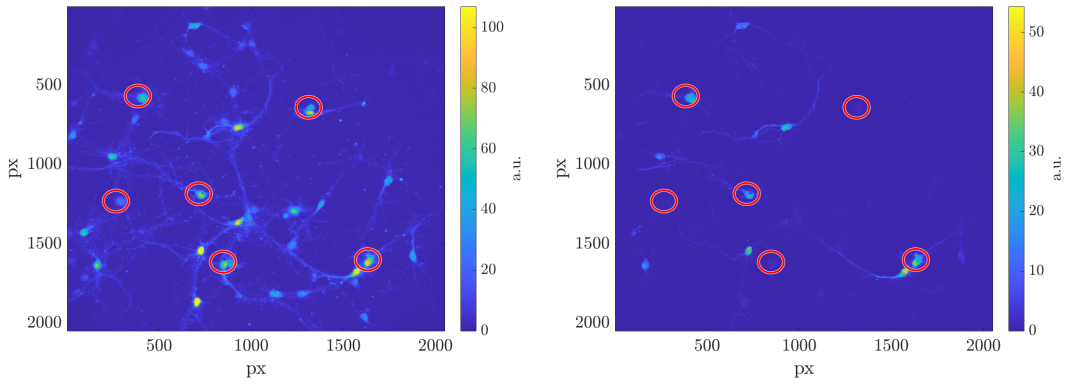

Figure 5.18: **Analysis pixel by pixel.** On the left the level of YFP indicator (i.e. the level of infection with ChR2) is shown, while on the right the response intensity ($\Delta F/F$) obtained pixel by pixel is shown.

5.3.5 Half-field excitation

To see if the neurons respond to light, we illuminated the left half of the FOV: we will refer to this pattern illumination as *half-field illumination* (Fig. 5.19).

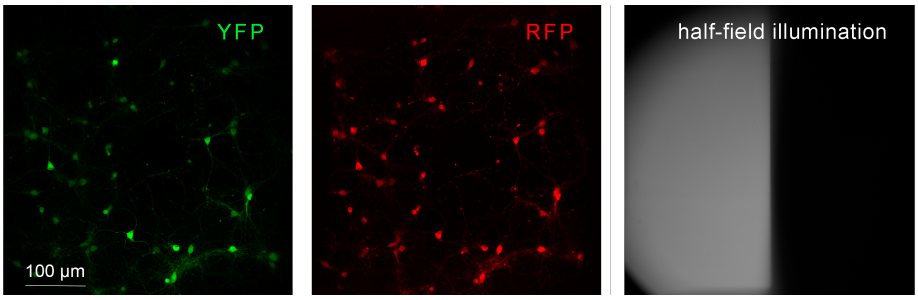

Figure 5.19: **Example of a half field illumination experiment.** From left to right the level of infection with ChR2, the presence of X-Rhod-1AM before excitation and the half-field illumination pattern are shown.

We performed the analysis described in the previous section with a threshold of 0.003 for $\Delta F/F_{rest}$, 1.2 for Σ, while no threshold was imposed for $corr_{std}$ and $corr_{sat}$. To set the intensity, we stimulated different cultures in age between 11 and 13 DIV, changing the excitation intensity from 0.5 to 30 mW/mm^2. The same analysis was performed both on the cells in the left half of the field, thus illuminated, and on the right, thus left in the dark. We then analyzed the neuronal responses in the entire FOV of the objective, comparing the number of responses got in the illuminated and dark regions, calculating the percentage of neurons that respond over all the neurons found in the respective region (% number), as well as the $\Delta F/F_{rest}$ values of the responses in the two regions. As shown in figure 5.20, $\Delta F/F_{rest}$ does not correlate with the changing in excitation intensity, while the number of responses increases up to a plateau over 10 mW/mm^2. The plateau value of the number of the responses is just above 50%: the reason why the 100% is not reached can be explained by different reasons. First of all, infection with ChR2 of the cells in the culture is not uniform, and this can affect the responses; anyhow, the rate of infection is about 80%. Furthermore, cortical cultures can be made up of multiple subtypes of neurons and ROI localization cannot distinguish between them. Eventually, it must be considered that the indicator may be insufficiently sensitive to detect tiny neuronal responses, and saturation of the indicator can occur before light excitation.

The same analysis was performed dividing cells according to their horizontal coordinates, in regions of 200 pixels, and the average values of these areas were plotted in bar graphs in figure 5.21. When the responses in the half illuminated and dark side are compared, it is clear that cells respond to the light stimulus also in the non-illuminated part. This is also observed in the pixel by pixel analysis shown in figure 5.22. This can be explained by the fact that it is not unlikely that some cells whose body is in the dark region have some processes that arrive in the illuminated part: since ChRs are expressed all over the cell membrane, cells can be excited also if parts of their processes are illuminated; moreover, since we are detecting calcium signals, it must be considered the

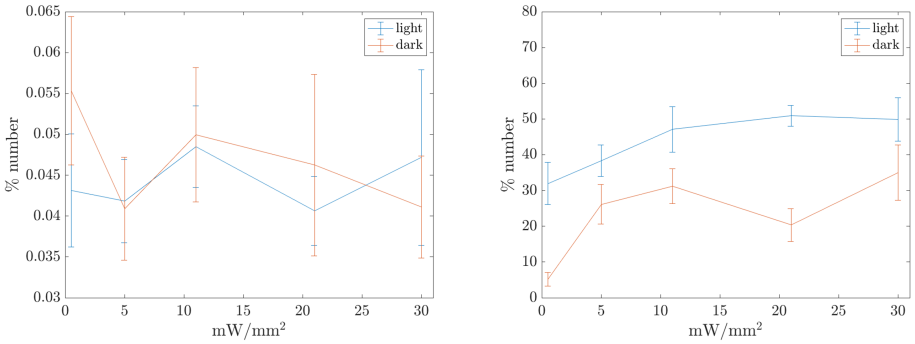

Figure 5.20: **Dependence on excitation intensity.** On the left the average values of $\Delta F/F_{rest}$ in the illuminated and dark regions at 11-13 DIV, changing the excitation light intensity; on the right, the percentage of neurons that respond on the illuminated and on the dark regions with respect to the number of neurons counted in the respective region, increasing the excitation intensity. The average was performed on N=9 FOV for I=0.5 mW/mm^2, N=9 FOV for I=5 mW/mm^2, N=13 FOV for I=11 mW/mm^2, N=7 FOV for I=21 mW/mm^2 and N=8 FOV for I=30 mW/mm^2. Error bars represent the standard error of the measurements.

possibility that the responses we see on the right follow a communication with the illuminated cells [83]. These considerations explain also the fact that in the bar graphs the difference is not sharp at the illumination boundary but decreases increasing the distance from it. The data clearly show that the number of responses is very different comparing the illuminated and dark side of the FOV. In particular, the higher the excitation intensity, the more the histogram distribution flattens.

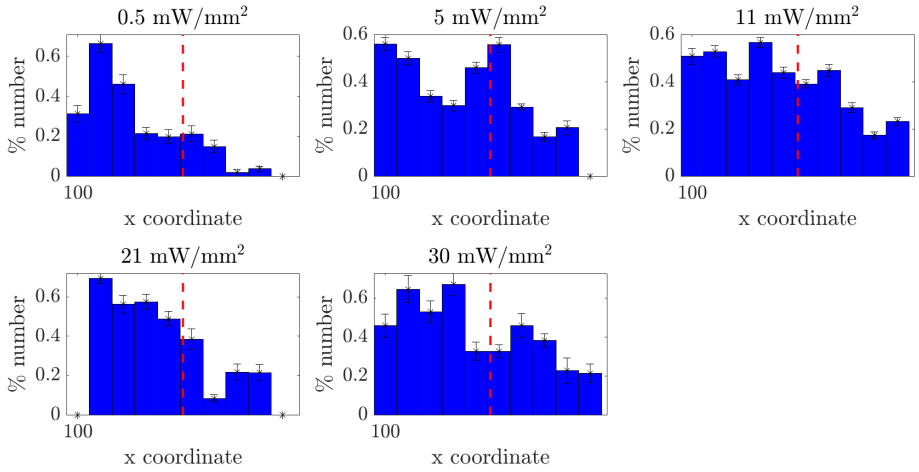

Figure 5.21: **Number of responding neurons in the FOV.** Histograms of the number of responding neurons depending on the horizontal position (x-coordinate) in the FOV.

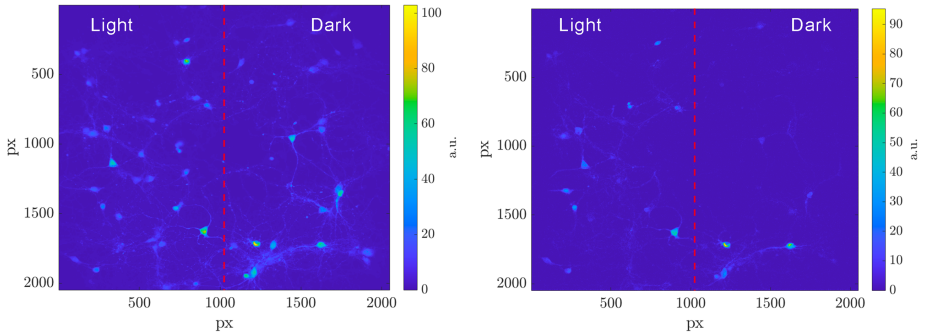

Figure 5.22: **Pixel by pixel analysis.** Example of the pixel by pixel analysis performed on one experiment: on the left is plotted the YFP level, while on the right it is plotted the response level obtained from the trace of each pixel.

To see how the development of our cultures plays a role in this distribution, measurements were performed at 0.5 mW/mm^2 on the same set of cultures at 20-21 DIV. Interestingly, as shown in figure 5.23, while at 11-13 DIV the $\Delta F/F_{rest}$ of illuminated and not-illuminated neurons were similar, at 20-21 DIV neurons in the illuminated region showed an increase in responses (even if not statistically significant). Moreover, at 20-21 DIV, the number of responses in the illuminated and dark part are very similar. At this age the network is more developed, neurons are more mature and, consequently, respond better to excitations, and are more interconnected. However, at 20-21 DIV the number of cells that survive start to decrease with consequent decreased number of recordable responses. For this reason, we chose to perform the following experiments at 10-14 DIV.

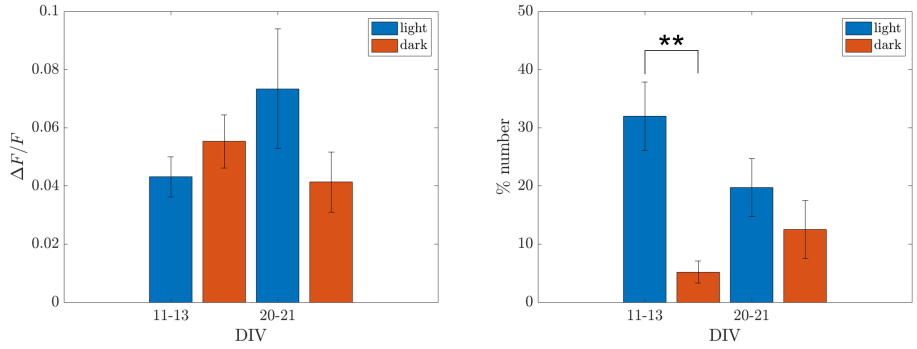

Figure 5.23: **Dependence on neurons' age.** Comparison of the average of $\Delta F/F_{rest}$ (left) and of the percentage number of responding neurons (right) at 0.5 mW/mm^2 of intensity at 11-13 DIV and 20-21 DIV, both for the illuminated and dark regions. Bars represent the average performed on N=9 FOV for 11-13 DIV and N=15 FOV for 20-21 DIV. Error bars shown in the analysis represent the standard error of the measurements. **P<0.01, unpaired T-test.

5.3.6 Single neurons excitation

We next focused our attention on single cell excitation. We performed light excitation on 11 DIV neurons using the light spots shown in section 5.2, starting from one single cell in the FOV up to 6 (figure 5.24) with about 10 mW/mm^2 of intensity. We acquired the images with the 20x objective, without any crop of the FOV. As can be seen from the pixel by pixel analysis shown in the figure, not always the illuminated neurons respond: this can be explained by the same reasons as used for the half-field illumination. Indeed, accordingly to the previous analysis, considering all the measurements performed, the 50% of the illuminated neurons responded.

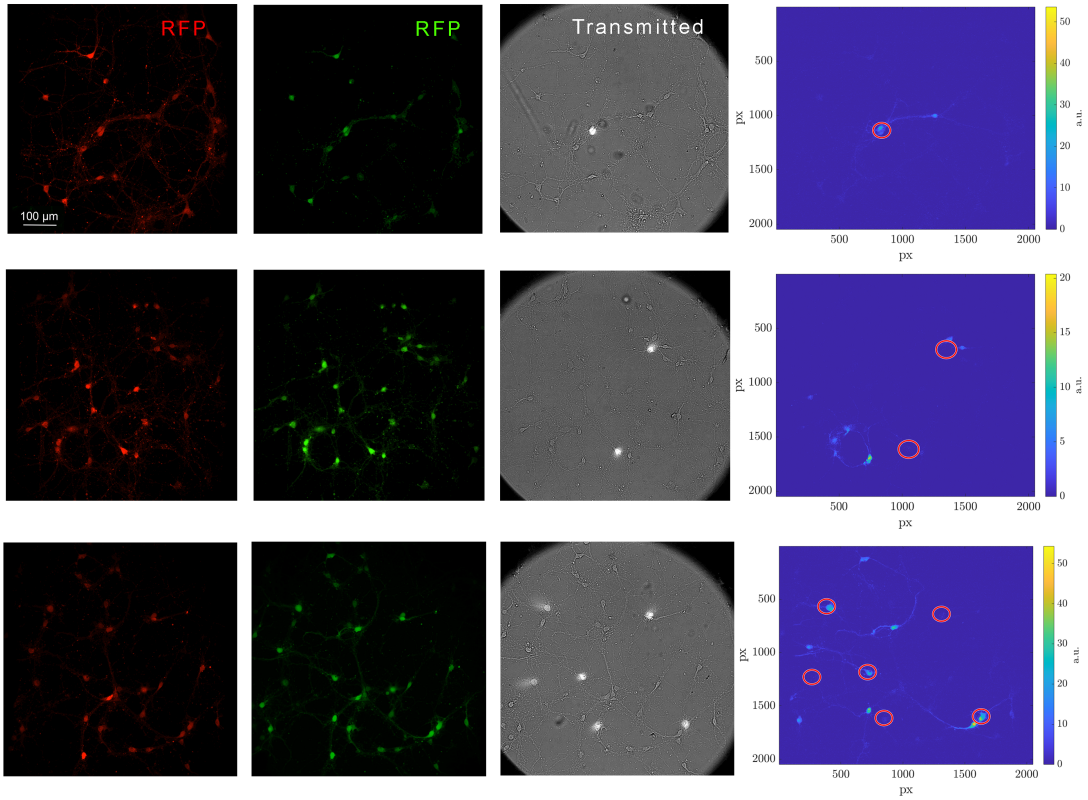

Figure 5.24: **Examples of spot excitation.** (a) Images of cultures in RFP, YFP and transmitted configuration, for the 3 different illumination patterns: 1 spot, 2 spots, 6 spots.

Interestingly, neurons that are not directly illuminated showed calcium responses too. As discussed before, these responses might be the result of the illumination of their processes that happens to come in the area of the spot, or they can be the result of neuronal communication. Pixel by pixel analysis reveals that both hypotheses are plausible. In particular, looking at the 2 spot excitation example, we can see that two neurons responded very near to the upper spot, probably because their processes were excited; nevertheless, considering the bottom spot, the responding neurons around that one are pretty

far from the spot. In this case it can be that some processes of the nearest neuron (that shows also higher response) were activated and that the other three neurons responded following neuronal communication. On the multi-tiff images the same analysis described in the previous section was performed, with the same threshold levels to select the responses. Then, for each cell under the spots, the distance between its centroid and the centroids of all the neurons that responded in the FOV out of the spot was calculated, in order to understand how far from the spots the responses of the non illuminated neurons were detected. For each FOV, we normalized the $\Delta F/F$ values to the maximum value recorded in the FOV and we plotted them as a function of the distance from the spot, after averaging the values with a binning value of 20 pixels. With the same binning we also plotted the histograms showing the number of responses at different distances from the spots. In figure 5.25(a), the data for the case of 2 and 6 spots are shown. Focusing the attention on the 2 spots data, it can be seen that in our cultures the neuronal responses were stronger near to the excited neurons and they decrease on a distance of about 600 px (195 μm). Then, since in the FOV a second spot was present, the value increases again: on average the 2 spots were 1021 $\pm$ 236 pixels distant. Considering this value, also the second slope confirms that neurons communicate up to about 195 μm. Also the histograms of the responses confirm this behaviour (figure 5.25(b)). Instead, when a 6 spot excitation is performed, the curve is flatter: since more neurons are simultaneously excited, it is no more possible to distinguish the effect of the single spots, as was happening in the case of the half-field excitation. The histogram in the case of 6 spots excitation reaches the gaussian shape that represents simply the average distribution of the distance between all the neurons in the culture. This characteristic distance of the responding neurons can be interesting for the study of the behaviour and connection of the neuronal network. Using calcium analyses many studies can be performed on the connectivity of the cultures [83, 165, 170, 172, 174]. However, since our goal is to create an engram in the in-vitro culture, we decided to prove one of the main characteristics of an engram: the strengthening of synaptic connections.

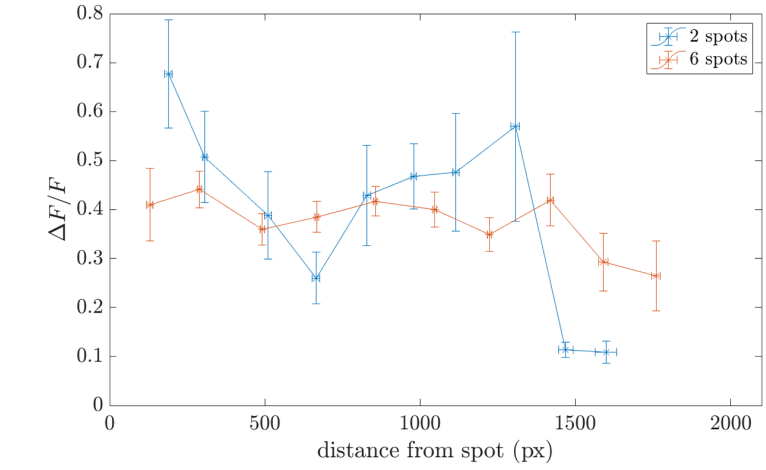

(a)

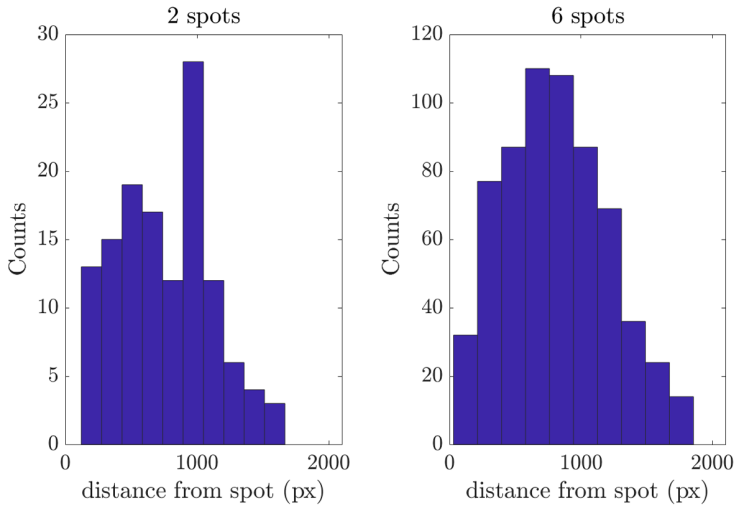

(b)

Figure 5.25: **Analysis of spot excitation.** (a) $\Delta F/F$ of the responding and not excited neurons in function of their distance from the spot, in the case of 2 or 6 spots. (b) Histograms represent the number of responding neurons at a given distance from the spots, in the case of 2 and 6 spots.

5.4 Summary and discussion

In this chapter the integration of a digital light projector (DLP) in the confocal super-resolution microscope setup was described. The DLP is equipped with 3 LED sources, providing different possible excitation wavelengths. In this work we characterized the system for the spectral region <500 nm. Blue patternized light can be projected on the sample plane with a resolution of 3 ± 1 μm with a 20x objective, and pulsed with μs resolution. Experimental measurements on ChR2-infected cortical and hippocampal cells show that the system is able to induce cell excitation, both on big areas of the culture and on single neurons. The cell response was detected using X-Rhod1-AM calcium indicator, whose spikes in correspondence of light illumination were analysed with a custom MATLAB code able to recognize cell bodies in the acquired images and analyse local calcium traces. Also a pixel-by-pixel analysis of the images was performed, which allows the visualization of the calcium behaviour also on the cells' processes. From these experiments we set our experimental conditions at 11-13 DIV with an excitation intensity of about 10 mW/mm^2, able to induce ChR2 activation [16, 62, 76, 82, 123, 125, 139]. The possibility of exciting single neurons makes this system very useful for various studies: choosing the proper temporal pattern of the light excitation, memory can be induced into the culture and the related behaviour of the neuronal/synaptic engram can be studied; another example can be the application of the system in epilepsy studies with the use of halorodopsins for neuronal inhibition.

Chapter 6

Inducing in-vitro neuronal engrams

As described in chapter 3, during memory formation *long term potentiation* (LTP), occurs in the synapses. Here, if LTP is induced, several molecules are found, such as *Arc* (Activity-regulated cytoskeleton-associated protein), an immediate early gene, whose synthesis is dependent on NMDA receptors activation [175]. We then decided to use an LTP-like pattern light illumination on neurons transfected with SynActive (SA), a new approach combining *Arc* mRNA targeting elements with a protein tag for activity-dependent protein production in spines [118].

6.1 Cell preparation

Embryonic cortical and hippocampal cells cultures were prepared from wild type mice as previously described in section 5.3.1, and transfected by nucleofection with TREp-Arc3'-NendPSDTag-Venus-HA-Arc5'UTR and CAG::rtTA-IRES-tdTomato (SA). Neurons were also infected with adeno associated virus pAVV-hSyn-hChR2(H134R)-EYFP at 2-4 DIV. At 10-13 DIV cells were treated with doxycycline (1mM for 24 hours); neurons expressing both Tomato (as a reporter for SA transfection) and YFP (as a reporter for ChR2 expression) were selected for spot light excitation. Cells were then fixed 90 min with Paraformaldehyde (PFA) 4% after stimulation and subjected to immunocytochemistry for the detection of HA-tag and/or Venus proteins in spines. The presence of HA or Venus in neuronal spines indicates that Arc synthesis happened, suggesting the successful potentiation of the cell.

6.2 LTP Experiments

In order to induce LTP on neurons, 10 trains of 13 light pulses at 100 Hz were repeated at 0.5 Hz [118]. This pattern was first of all tested on non-transfected neurons with calcium experiments, archiving results similar to the previous no-LTP pattern, confirming that neurons were excited by light. Since this kind of

pattern cannot be created directly from the DLP software, we used a function generator (Rigol DG2052) to create the pattern, that can be sent through the Trigger-in cable to the DLP, as shown in figure 6.1. If no optical acquisition during the excitation is required, then we simply create and send the pattern to channel 1 (CH1) of the function generator. If instead an optical acquisition is needed, then a different pattern is created for channel 2 (CH2), which simultaneously go as a trigger-in for the camera and as shutter controller of the LED source global shutter (dashed path in figure 6.1). TTL signals input to the global shutter synchronously toggles all currently enabled source channels on and off. The use of the shutter is needed because the only way to trigger camera acquisition with Metamorph software is to use a setting (*stream acquisition*) which, since is used for fast acquisitions, leaves the excitation light always on. Then, the only way to act over the excitation line, is to use a TTL signal on the LED shutter. In this configuration, the signal coming from CH2 triggers the camera acquisition, and simultaneously the opening of the shutter, every 6Hz. Then, after a desired number of frames (100 in our case), the CH2 channel sends the LTP pattern to the DLP. Since after each train of pulses there are 2 seconds in which stimulation light is off, the camera was imposed to acquire some frames just in between the train pulses. In this way it is possible to monitor the changes in optical signal coming from the sample during all the stimulation process, without introducing artefacts in the measurements.
To perform the experiments with SA, neurons were treated with doxycycline 1mM for about 24 hours. After this time, for each coverslip we performed the following procedure. Coverslips were moved to a 35 mm plastic dish, containing 2 ml of HBSS, Ca2Cl (2mM) and MgCl (1mM) at 37°C and doxycycline 1μM. Before doing this procedure, on the bottom of the coverslip 3 shapes (triangle, circle and square) are carefully drawn with a water resistant pen: these shapes are useful as spatial reference to find again the stimulated cells after the immunocytochemistry. The dish is then positioned on the sample holder under the microscope, and imaged with 10X or 20X objectives (these magnifications allow to image a sufficiently big neuronal network in which we can excite with spots neurons, with suitable distances among them). First of all, we calibrate the DLP on empty regions of the coverslips. Then, we check for neurons expressing SA (tdTomato) and Chr2 (YFP). Once the proper field of view is found, we performed DLP patterned illumination. We performed different experiments, with widefield illumination, 1 spot and 2 spots in 2-3 different FOVs for each coverslip. As control, we used coverslips in which doxycycline was not applied. After stimulations, coverslips were maintained in the conditioned media for 1 hour and 30 minutes, and fixed with 4% PFA.

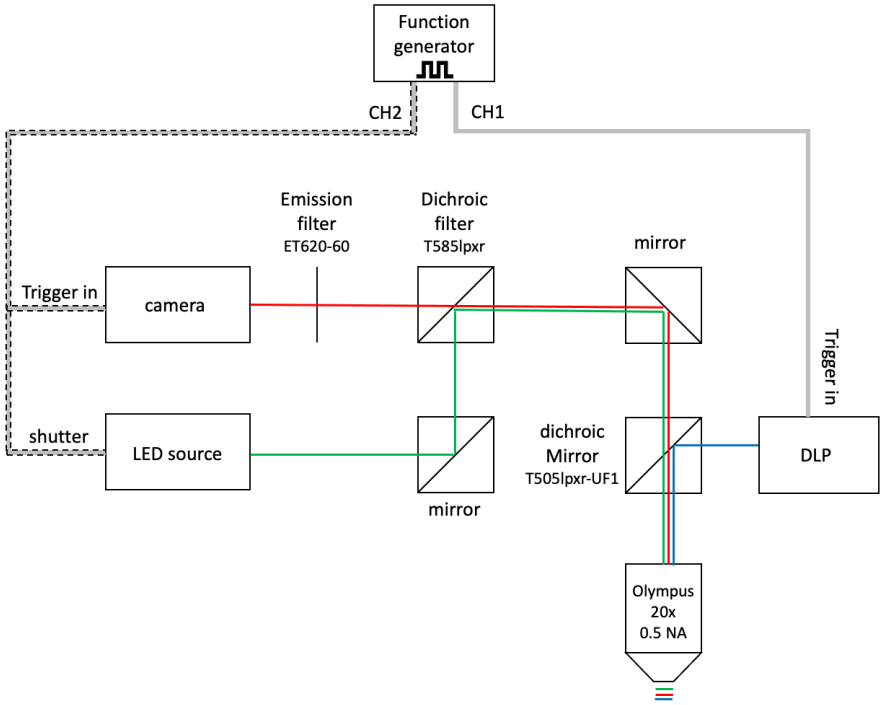

Figure 6.1: **Optical setup for LTP experiments.** A sketch of the optical setup used for LTP experiments. The configuration is the same as in figure 5.14, with the difference that the camera and the DLP are governed by two different trigger signals coming from the function generator.

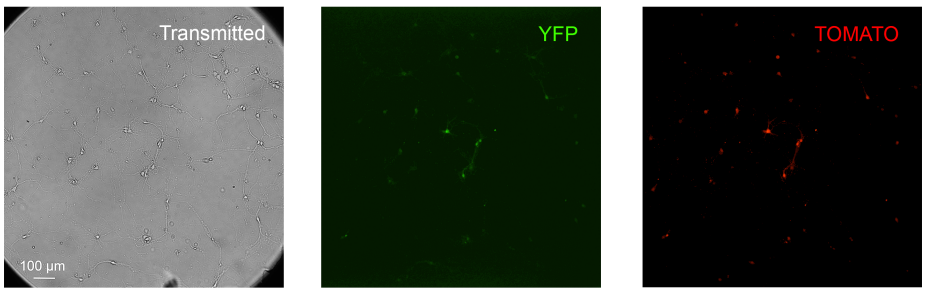

Figure 6.2: **Example ready for the experiment.** From left to right, an image of a culture taken with transmitted configuration, an image of ChR2 infection taken in YFP configuration and an image of the transfection taken with RFP configuration.

6.3 Immunocytochemistry

After illumination, cells were treated with 0,1% Triton X100 for 20 min, blocked with 3% Bovine Serum Albumine (BSA) in Phosphate Buffer Saline (PBS) for 1h and incubated overnight with primary antibodies (α-HA Abcam ♯ab9111, 1:2000; α-RFP Rockland ♯600-401-379, 1:1000) diluted in blocking buffer. Cells were washed in PBS and incubated for 2h at room temperature with secondary antibodies diluted in blocking buffer. Cells were counterstained with DAPI and mounted with Aqua Polymount (Polyscience Inc.).

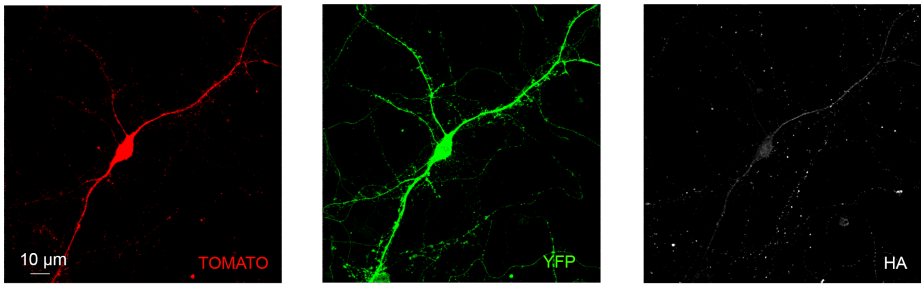

Figure 6.3: **Example of immunocytochemistry.** Representative cortical neuron at DIV 12 expressing tdTomato (red), ChR2-YFP (green) and HA (white).

6.4 Analysis and results

Confocal imaging was performed on the treated cells using a laser-scanning motorized confocal system (Nikon A1) equipped with an Eclipse Ti-E inverted microscope and four laser line (405, 488, 561 and 638 nm). Z-series images were taken with an inter-stack interval of 0.5 μm using 60X oil immersion objective (Nikon APO 60x 1.4 Oil).

Light induced LTP analysis

On the acquired images of transfected cells, a crop was performed isolating portions of processes near the cell body, within about 20 μm. Then, taking advantage of the tdTomato cellular filler, we morphologically localized the spines along the process. We considered as spine any protuberance coming out from the process without focusing on specific morphologies. The presence of HA signal (HA+ spine) was checked for each spine. We performed this analysis stack by stack to correctly localize spines. The number of HA+ spines over the total number of counted spines (N_{HA+}/N_{tot}) was then recorded. We performed this analysis on both the illuminated neurons and non illuminated neurons (control). Data were normalized to the control cells ($(\overline{N_{HA+}/N_{tot}})_{control}$):

$$\Delta = \overline{\left(\frac{N_{HA+}/N_{tot}}{(\overline{N_{HA+}/N_{tot}})_{control}} \right)}. \tag{6.1}$$

First of all, this analysis was performed on neurons expressing ChR2 excited by widefield illumination. We considered the stimulation of each field of view

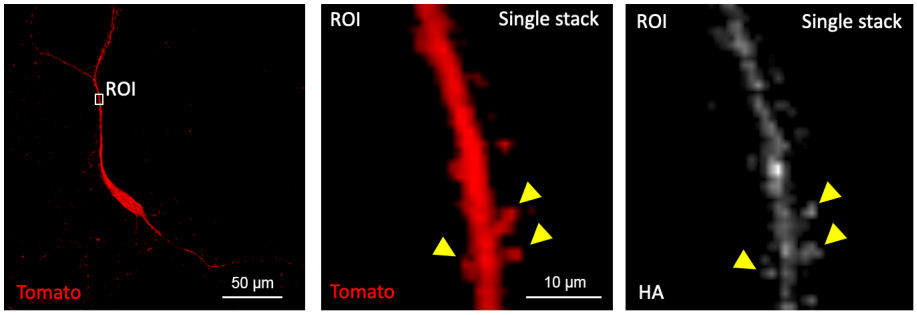

Figure 6.4: **Analysis.** The image illustrates how we localize spines along the processes taking advantage of Tomato signal. Then, HA signal colocalization is checked.

as independent experiments. Figure 6.5(a) shows the Δ values for stimulated (light) and non-stimulated (dark) neurons. Stimulated cells show a significantly increased number of HA+ spines compared to non-stimulated cells (p=0.0075). As control, we performed illumination on neurons in absence of doxycycline, confirming that in this condition HA+ spines are not increased by light-stimulation (figure 6.5(b)). Moreover, we evaluated the number of HA+ spines in coverslips treated with doxycycline without DLP-light-stimulation, in order to exclude an effect of environmental light on ChR2 or network spontaneous activity on HA expression in spines. As shown in figure 6.5(c), the values are comparable with control neurons in stimulated coverslip.

Then, we performed the same analysis on coverslips on which spot excitation was performed. In each field of view two cells were excited. HA+ spines of excited cells and of the other cells inside the field of view were normalized over those far from the experiment regions. The results are shown in figure 6.6. The cells illuminated with spots show a number of potentiated spines that is significantly increased compared to the cells far from the field of view (p=0.0018). Cells not illuminated in the field of view show Δ values comparable to controls.

Together, these results suggest that LTP-inducing light illumination with the DLP setup is able to induce spine potentiation in neuronal culture. Inducing potentiation simultaneously on 2 cells in a field of view is a first step for the creation of an engram in vitro. Next steps require the test of other properties of engrams, like NMDA/AMPA ratio, increased number of spines and eventually memory retrieval.

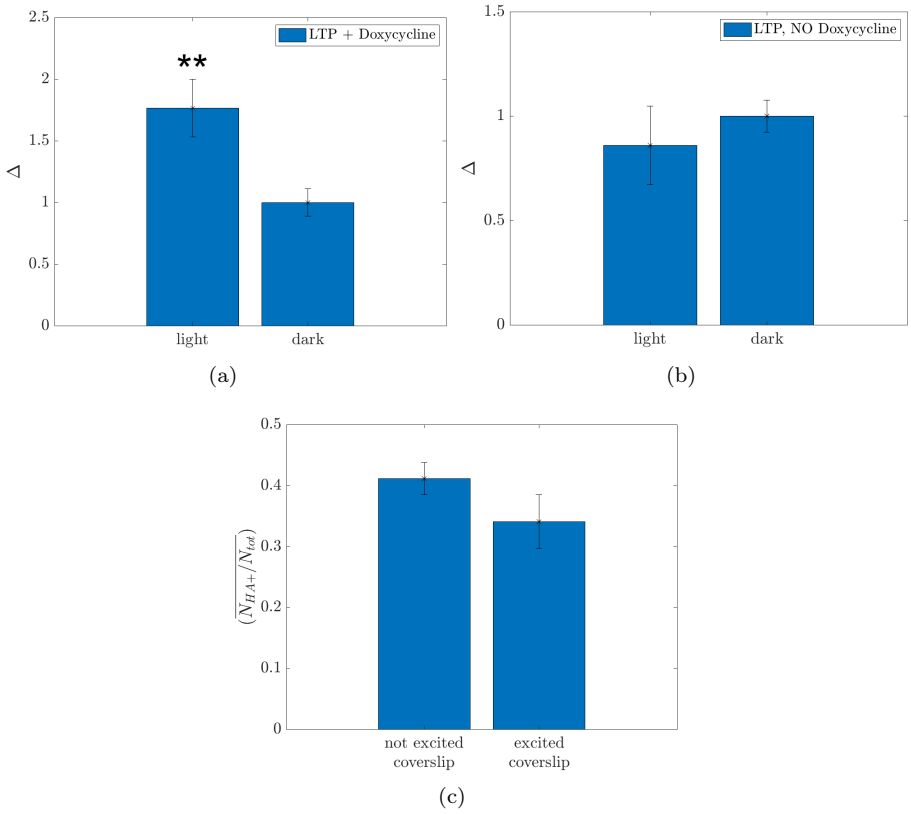

Figure 6.5: **LTP analysis.** (a) Analysis performed on coverslip excited with widefield illumination, in presence of doxycycline (N=6 FOV), using cells in dark regions as internal controls (N=8 neurons). **P<0.01, unpaired T-test. (b) Same analysis, performed on samples excited in absence of doxycycline (N light = 4 FOV, N dark = 20 neurons). (c) Comparison of N_{HA+}/N_{tot} got on cells in dark regions of excited coverslips (N=8 neurons) and cells in not excited coverslips (N=13 neurons). Data is average ± standard error.

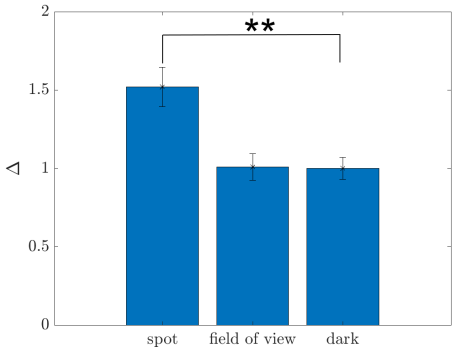

Figure 6.6: **LTP analysis on spot excitation.** The bar graph shown the Δ values got on the cells excited with spot illumination (N=7 FOV), on cells in the same field of view (N=7 FOV), but not illuminated and on cells far from the field of view (dark) (N=26 neurons). Data are average ± standard error. **P<0.01, unpaired T-test.

6.5 Summary and discussion

In this chapter, long term potentiation (LTP) was induced into neurons using the DLP setup. Cells were transfected with SynActive (SA), a new approach that combines *Arc* mRNA targeting elements with a protein tag for activity-dependent protein production in spines (HA-tag in our case) [118]. The used LTP-inducing light pattern consists in 10 trains of 13 light pulses at 100 Hz, repeated at 0.5 Hz, with a light intensity $\geq$10 mW/mm^2. After stimulation, cells are then fixed with paraformaldehyde and subjected to immunocytochemistry for the detection of HA-tag proteins in spines. We compared the number of HA+ spines over the total number of counted spines, recorded in illuminated and not illuminated cells (controls): we performed both illumination of the entire FOV and light spots on single neurons. The results show that the DLP setup is able to induce spine potentiation in neuronal culture. This opens a big opportunity to study basic principles of memory coding.

Each memory in the brain is associated to a specific cellular circuitry, in which cells are simultaneously excited, following Hebb's law: *cells that fire together wire together*. In previous works, it was demonstrated that, if long term potentiation (LTP) occurs simultaneously in cells, specific molecular and structural modifications occur in them. These cells form the *engram*, a cell assembly that holds the memory of that specific experience [94–97]. Following this definition, we induced the formation of the simplest possible engram: we optogenetically induced simultaneous potentiation on 2 neurons in an in-vitro neuronal culture. Starting from this basic engram, several studies can be performed. First of all, taking advantage of HA-tag expressed through SA transfection, we observed that not all the spines in the illuminated neurons are potentiated. This is already known from in-vivo studies: in engram cells only some spines show potentiation, a clue that lead to think about a *synaptic engram*, rather than a neuronal engram [94, 96, 98, 99, 117, 121].

In a simple in-vitro system like this, we can perform analyses difficult to be carried on in vivo, with an higher number of neurons (and spines), and other cells involved.

For example, we can understand why just that specific spines were potentiated, classifying them morphologically, and/or studying the molecular mechanism involved. Then, we can understand if there is a specific pattern in the distribution of potentiated spines (for example clusterization) or if they are distributed randomly. If this pattern is observed, which are the processes that regulate it?

Then, we can try to increase the number of stimulated neurons in the network: does the number of cells involved influence the synaptic engram properties?

Eventually, we can introduce in our neuronal cultures also other cells, like astrocytes. These cells influence synaptic communication and act like hubs, being each astrocyte in connection with millions of spines belonging to different neurons. It is already known that these cells play an important role in memory [100, 101]. In our system we can test what is the influence of astrocytes in memory encoding and how it influences the synaptic engram.

Memory can be studied testing 3 main steps: coding, recall and amnesia. We demonstrated that our system is able to induce engram formation, and is suitable to study several aspects involved in memory coding. Then, these aspects could be evaluated also in the frame of memory recall and amnesia, in order to unveil still unknown processes that regulate our mind.

Chapter 7

Conclusions and future directions

In this work, I described the development of two platforms suitable for optogenetic experiments on in-vitro neuronal cultures [30]: an integrated photonic chip, designed to excite neurons plated on its surface, and a digital light projector integrated to a microscopy setup, able to excite single neurons on the sample plane.

During the design of the photonic chip, a new computational technique was implemented, to optimize diffractive grating structures in order to obtain a specific light distribution on the surface of the chip. The optimized gratings create spots with dimensions comparable to a neuronal body, focalized on the sample plane. The measured intensity coming from these scattering structures was $> 1\text{mW/mm}^2$, enough to optogenetically excite neurons expressing ChR2 channelrhodopsin [16, 62, 76, 82, 123, 125, 139]. The spatial confinement of the scattered light resembles well the simulated one. A 34-fibers fiber array was fixed to the chip, and a portable package was designed in order to use the system under a microscope, to optically monitor the activity of the neurons following their excitation. Biocompatibility tests of the whole system are in progress to allow the growth of neurons directly on the surface of the photonic chip. However, the system could be modified also to perform experiments on neurons plated on glass coverslips, placed on the photonic chip inside the package. The use of multiple coverslips with the same package would bring slower wear of the system and the possibility of performing many more experiments, saving experimental time. This approach could be coupled with an optical recording of the neuronal activity. In addition, if neurons are plated on the photonic chip, both optical and electrophysiological monitoring of the culture can be performed, integrating a custom MEA inside the photonic chip.

The second setup I developed consists in a digital light processor device (DLP) integrated in a confocal-super resolution microscope, able to optogenetically excite neuronal cultures. The DLP is equipped with 3 LED sources, providing

different possible excitation wavelengths. In this work, we characterized the system for the spectral region <500 nm. Blue patternized light can be projected to the sample plane with a resolution down to 3 ± 1 μm with a 20x objective, and pulsed with ms resolution. Experimental measurements with X-Rhod1-AM show that the system is able to induce multiple and single neuron excitations with patternized light on ChR2 infected cultures. Then, simultaneous excitation of neurons transfected with SynActive (SA) [118] and infected with ChR2 was performed, using an LTP inducing temporal pattern with an intensity of about 10 mW/mm^2. The analysis performed through immunocytochemistry on the excited cells show that illuminated neurons present a higher number of potentiated spines with respect to the control ones. The simultaneous potentiation of specific neurons inside a 2D in-vitro neuronal network will allow the study of many basic processes that occur in memory formation, in neurons as well as in their spines.

Table 7.1: **Main characteristics of the two platforms.**

	Photonic chip	**DLP**
Wavelength	designed for 488 nm	3 broadband LED sources blue, green and red
Spatial resolution	about 10 μm, fixed	$\geq$ 3 μm, variable on the optical line
Temporal resolution	depends on laser source. In our system is 6 ns	235 μs to 8333 μs, depends on the bit-depth
Portability	YES	NO
Light pattern	single or multiple spots, fixed	any
Biocompatibility	under test	YES

Both the proposed setups have technical characteristics suitable for optogenetic activation of in-vitro neuronal cultures: spots of about 10 μm can be created, with intensity >1 mW/mm^2. The two platforms have pros and cons, summarized in table 7.1, that make them suitable for different applications. The DLP setup, being integrated in a microscope setup, is a fixed system, able to create reconfigurable light patterns, with a resolution of 3 ± 1 μm with a 20x objective, which changes with the magnification of the objectives. The minimum exposure time goes from 235 μs to 8333 μs, depending on the bit-depth of the projected image.
The photonic chip is indeed portable and can be used under the microscope, if needed. The main difference with the DLP system is that the spatial light configuration is fixed. However, if many scatterers singularly addressable are distributed over the surface, there is enough possibility to perform the desired experiments. The spatial resolution of the system is fixed and set by scatterer features. The light illumination frequency depends on the source used: in our case, the Cobolt laser can reach 150 MHz.

Hybrid 2D neural interfaces are under development, to create platforms for the study of simplified neuronal networks, both for clinical and research studies. They should be able to illuminate single neurons (or even specific parts of them), and read their responses, in an electrophysiological or optical

way. Compared to other developed platforms, like the ones proposed in [125] and [92], our photonic platform is able to achieve single neuron resolution, with a proper intensity for ChR2 excitation. In particular, the designed aperiodic grating scatters are able to focalize and shape light on a specific plane, in order to minimize the effect on the other neurons in the culture. It is a light and portable system, that does not need electronic alimentation, which would make the system bulky, and potentially hot [92, 125]. Our platform can be used under the microscope, to detect neuronal response to light excitation; in future, an electrical line could be integrated to the chip, to read neuronal electrical activity, as done in [92, 125]. Moreover, as envisioned by the BACKUP project, if the designed scattering structures are integrated inside a neuromorphic photonic chip, a compact hybrid platform would be created, where artificial and biological networks could interact. Interestingly, the neuromorphic network could be trained to recognize specific behaviours of the biological culture and intervene when necessary.

The DLP system installed in our microscope setup is suitable for in-vitro experiments on neuronal cultures with single cell resolution. This kind of sample does not not need a 3D focusing, as provided for example by spatial light modulators [176]. Even if the DLP is not a new technique itself, to our knowledge it is the first time that this kind of system is engineered to induce LTP in in-vitro neuronal cultures, to study synaptic engrams. In this work the smallest possible neuronal engram was formed, with the simultaneous excitation of 2 neurons [94–97]. In a simple in-vitro system like this, we can perform analyses difficult to be carried on in vivo, with a higher number of neurons (and spines), and other cells involved. The potentiated spines can be studied from the morphological point of view and the involved molecular processes can be characterized. These aspects can then be studied changing the number of neurons involved in the engram and also introducing in the culture different kinds of cells that can influence synaptic communication [100, 101].
The DLP system was engineered and tested in the frame of engram formation and memory study, but it must be considered that this platform, with its resolution, its 3 LED source, and the proper light deliver, is extremely versatile. It can be used with different kinds of photosensible proteins, for both excitation or inhibition of neuronal activity, for the study of different brain functions and pathologies among which memory is just an example.

Acknowledgements

I would like to thank Prof. Pavesi, my supervisor, for all the advices and the passion that he demonstrates carrying on the Nanoscience Laboratory, with all the different activities, with patience and attention.

I would then like to thank my 'co-supervisor' Mattia Mancinelli for the concrete help in the experimental activity and for teaching me the good way of writing codes.

I thank Beatrice Vignoli for the help in the biological experiments.

Last but not least, I thank Prof. Canossa for his advices.

I thank all the NanoLab, biologists and physicists, for the advices in the lab, for the good lunches, the parties and the feeling of always being at home.

Bibliography

[1] D. U. Silverthorn, *Fisiologia umana, un approccio integrato*. Pearson, 2017, 7th ed. a cura di Barbara Colombini, Carla Perego, Stefano Rifini.

[2] C. C. Vanni Taglietti, *Fisiologia e Biofisica delle cellule*. EdiSES, 2019.

[3] A. N. Zorzos, J. Scholvin, E. S. Boyden, and C. G. Fonstad, "Three-dimensional multiwaveguide probe array for light delivery to distributed brain circuits," *Optics letters*, vol. 37, no. 23, pp. 4841–4843, 2012.

[4] T.-i. Kim, J. G. McCall, Y. H. Jung, X. Huang, E. R. Siuda, Y. Li, J. Song, Y. M. Song, H. A. Pao, R.-H. Kim, *et al.*, "Injectable, cellular-scale optoelectronics with applications for wireless optogenetics," *Science*, vol. 340, no. 6129, pp. 211–216, 2013.

[5] J. Lee, I. Ozden, Y.-K. Song, and A. V. Nurmikko, "Transparent intracortical microprobe array for simultaneous spatiotemporal optical stimulation and multichannel electrical recording," *Nature methods*, vol. 12, no. 12, pp. 1157–1162, 2015.

[6] A. R. Mardinly, I. A. Oldenburg, N. C. Pégard, S. Sridharan, E. H. Lyall, K. Chesnov, S. G. Brohawn, L. Waller, and H. Adesnik, "Precise multimodal optical control of neural ensemble activity," *Nature neuroscience*, vol. 21, no. 6, pp. 881–893, 2018.

[7] A. E. Hramov, V. A. Maksimenko, and A. N. Pisarchik, "Physical principles of brain-computer interfaces and their applications for rehabilitation, robotics and control of human brain states," *Physics Reports*, vol. 918, pp. 1–133, 2021.

[8] X. Liu, S. Ramirez, P. T. Pang, C. B. Puryear, A. Govindarajan, K. Deisseroth, and S. Tonegawa, "Optogenetic stimulation of a hippocampal engram activates fear memory recall," *Nature*, vol. 484, no. 7394, pp. 381–385, 2012.

[9] S. Ramirez, X. Liu, P.-A. Lin, J. Suh, M. Pignatelli, R. L. Redondo, T. J. Ryan, and S. Tonegawa, "Creating a false memory in the hippocampus," *Science*, vol. 341, no. 6144, pp. 387–391, 2013.

[10] E. Segev, J. Reimer, L. C. Moreaux, T. M. Fowler, D. Chi, W. D. Sacher, M. Lo, K. Deisseroth, A. S. Tolias, A. Faraon, *et al.*, "Patterned photostimulation via visible-wavelength photonic probes for deep brain optogenetics," *Neurophotonics*, vol. 4, no. 1, p. 011002, 2016.

[11] A. N. Zorzos, E. S. Boyden, and C. G. Fonstad, "Multiwaveguide implantable probe for light delivery to sets of distributed brain targets," *Optics letters*, vol. 35, no. 24, pp. 4133–4135, 2010.

[12] D. R. Sparta, A. M. Stamatakis, J. L. Phillips, N. Hovelsø, R. Van Zessen, and G. D. Stuber, "Construction of implantable optical fibers for long-term optogenetic manipulation of neural circuits," *Nature protocols*, vol. 7, no. 1, pp. 12–23, 2012.

[13] K. Y. Kwon, B. Sirowatka, A. Weber, and W. Li, "Opto-μecog array: A hybrid neural interface with transparent μecog electrode array and integrated leds for optogenetics," *IEEE transactions on biomedical circuits and systems*, vol. 7, no. 5, pp. 593–600, 2013.

[14] F. Wu, E. Stark, P.-C. Ku, K. D. Wise, G. Buzsáki, and E. Yoon, "Monolithically integrated μleds on silicon neural probes for high-resolution optogenetic studies in behaving animals," *Neuron*, vol. 88, no. 6, pp. 1136–1148, 2015.

[15] R. Scharf, T. Tsunematsu, N. McAlinden, M. D. Dawson, S. Sakata, and K. Mathieson, "Depth-specific optogenetic control in vivo with a scalable, high-density μled neural probe," *Scientific reports*, vol. 6, no. 1, pp. 1–10, 2016.

[16] E. Shim, Y. Chen, S. Masmanidis, and M. Li, "Multisite silicon neural probes with integrated silicon nitride waveguides and gratings for optogenetic applications," *Scientific reports*, vol. 6, no. 1, pp. 1–5, 2016.

[17] F. Pisanello, G. Mandelbaum, M. Pisanello, I. A. Oldenburg, L. Sileo, J. E. Markowitz, R. E. Peterson, A. Della Patria, T. M. Haynes, M. S. Emara, *et al.*, "Dynamic illumination of spatially restricted or large brain volumes via a single tapered optical fiber," *Nature neuroscience*, vol. 20, no. 8, pp. 1180–1188, 2017.

[18] B. Li, K. Lee, S. C. Masmanidis, and M. Li, "A nanofabricated optoelectronic probe for manipulating and recording neural dynamics," *Journal of neural engineering*, vol. 15, no. 4, p. 046008, 2018.

[19] B. Ji, Z. Guo, M. Wang, B. Yang, X. Wang, W. Li, and J. Liu, "Flexible polyimide-based hybrid opto-electric neural interface with 16 channels of micro-leds and electrodes," *Microsystems & nanoengineering*, vol. 4, no. 1, pp. 1–11, 2018.

[20] A. Mohanty, Q. Li, M. A. Tadayon, S. P. Roberts, G. R. Bhatt, E. Shim, X. Ji, J. Cardenas, S. A. Miller, A. Kepecs, *et al.*, "Reconfigurable nanophotonic silicon probes for sub-millisecond deep-brain optical stimulation," *Nature biomedical engineering*, vol. 4, no. 2, pp. 223–231, 2020.

[21] D. Poole, A. Mackworth, and R. Goebel, *Computational Intelligence*. Oxford University Press, 1998.

[22] G. Sartor and F. Lagioia, "Le decisioni algoritmiche tra etica e diritto," *Intelligenza artificiale. Il diritto, i diritti, l'etica, Milan*, 2020.

[23] M. U. Scherer, "Regulating artificial intelligence systems: Risks, challenges, competencies, and strategies," *Harv. JL & Tech.*, vol. 29, p. 353, 2015.

[24] Y. N. Harari, *Homo deus: breve storia del futuro*. Giunti, 2017.

[25] U. Hasson, S. A. Nastase, and A. Goldstein, "Direct fit to nature: an evolutionary perspective on biological and artificial neural networks," *Neuron*, vol. 105, no. 3, pp. 416–434, 2020.

[26] A. N. Lupas, J. Pereira, V. Alva, F. Merino, M. Coles, and M. D. Hartmann, "The breakthrough in protein structure prediction," *Biochemical journal*, vol. 478, no. 10, pp. 1885–1890, 2021.

[27] A. W. Senior, R. Evans, J. Jumper, J. Kirkpatrick, L. Sifre, T. Green, C. Qin, A. Žídek, A. W. Nelson, A. Bridgland, *et al.*, "Improved protein structure prediction using potentials from deep learning," *Nature*, vol. 577, no. 7792, pp. 706–710, 2020.

[28] R. Pearce and Y. Zhang, "Deep learning techniques have significantly impacted protein structure prediction and protein design," *Current opinion in structural biology*, vol. 68, pp. 194–207, 2021.

[29] M. A. Lancaster, M. Renner, C.-A. Martin, D. Wenzel, L. S. Bicknell, M. E. Hurles, T. Homfray, J. M. Penninger, A. P. Jackson, and J. A. Knoblich, "Cerebral organoids model human brain development and microcephaly," *Nature*, vol. 501, no. 7467, pp. 373–379, 2013.

[30] "Backup neuromorphic photonics and the brain, unveiling the relationship between brain connectivity and function by integrated photonics." `https://r1.unitn.it/back-up/`. Accessed: 4th January 2021.

[31] J. Yoo and M. Shoaran, "Neural interface systems with on-device computing: machine learning and neuromorphic architectures," *Current opinion in biotechnology*, vol. 72, pp. 95–101, 2021.

[32] N. Wu, S. Wan, S. Su, H. Huang, G. Dou, and L. Sun, "Electrode materials for brain–machine interface: A review," *InfoMat*, vol. 3, no. 11, pp. 1174–1194, 2021.

[33] R. A. Andersen, T. Aflalo, L. Bashford, D. Bjånes, and S. Kellis, "Exploring cognition with brain–machine interfaces," *Annual review of psychology*, vol. 73, pp. 131–158, 2022.

[34] B. Fiani, T. Reardon, B. Ayres, D. Cline, and S. R. Sitto, "An examination of prospective uses and future directions of neuralink: The brain-machine interface," *Cureus*, vol. 13, no. 3, 2021.

[35] B. Braunschweig and M. Ghallab, *Reflections on artificial intelligence for humanity*. Springer, 2021.

[36] "Biodiritto." `https://www.biodiritto.org/`. Accessed: 7th February 2021.

[37] "Bruno kessler center in information and communication technology (fbk-ict irst center)." `https://ict.fbk.eu/`. Accessed: 7th February 2021.

[38] D. Bazzanella, G. Bincoletto, M. Consolandi, M. Fasan, F. Gennari, F. Carmelo La Vattiata, L. Rinaldi, D. Roccaro, and C. Zaccaria, "Artificial and biological neurons: Interdisciplinary issues and future perspectives. white paper," *BioLaw Journal – Rivista di BioDiritto, n. 1*, 2021.

[39] K. Freeman, "Algorithmic injustice: How the wisconsin supreme court failed to protect due process rights in state v. loomis," *North Carolina Journal of Law & Technology*, vol. 18, no. 5, p. 75, 2016.

[40] K. Jebari, "Brain machine interface and human enhancement–an ethical review," *Neuroethics*, vol. 6, no. 3, pp. 617–625, 2013.

[41] S. Reardon, "Can lab-grown brains become conscious?," *Nature*, vol. 586, no. 7831, pp. 658–662, 2020.

[42] K. Daniel, *Thinking, fast and slow*. Farrar, Straus and Giroux, 2011.

[43] "Unitrento fisica - alla scoperta del progetto backup. discover the backup project.." `https://youtu.be/rCeEm-LF6q0`. Accessed: 8th January 2021.

[44] M. Papa, M. C. Bundman, V. Greenberger, and M. Segal, "Morphological analysis of dendritic spine development in primary cultures of hippocampal neurons," *Journal of Neuroscience*, vol. 15, no. 1, pp. 1–11, 1995.

[45] C. Boyer, T. Schikorski, and C. F. Stevens, "Comparison of hippocampal dendritic spines in culture and in brain," *Journal of Neuroscience*, vol. 18, no. 14, pp. 5294–5300, 1998.

[46] C. Sala, "Molecular regulation of dendritic spine shape and function," *Neurosignals*, vol. 11, no. 4, pp. 213–223, 2002.

[47] M. Borczyk, M. A. Śliwińska, A. Caly, T. Bernas, and K. Radwanska, "Neuronal plasticity affects correlation between the size of dendritic spine and its postsynaptic density," *Scientific reports*, vol. 9, no. 1, pp. 1–12, 2019.

[48] E. Pchitskaya and I. Bezprozvanny, "Dendritic spines shape analysis—classification or clusterization? perspective," *Frontiers in Synaptic Neuroscience*, vol. 12, p. 31, 2020.

[49] "Vecteezy." `https://www.vecteezy.com/`. Accessed: 13th February 2021.

[50] C.-P. Richter, A. I. Matic, J. D. Wells, E. D. Jansen, and J. T. Walsh, "Neural stimulation with optical radiation," *Laser & photonics reviews*, vol. 5, no. 1, pp. 68–80, 2011.

[51] L. Fenno, O. Yizhar, and K. Deisseroth, "The development and application of optogenetics," *Annual review of neuroscience*, vol. 34, pp. 389–412, 2011.

[52] A. C Thompson, P. R Stoddart, and E. D. Jansen, "Optical stimulation of neurons," *Current Molecular Imaging (Discontinued)*, vol. 3, no. 2, pp. 162–177, 2014.

[53] G. P. Dugué, W. Akemann, and T. Knöpfel, "A comprehensive concept of optogenetics," *Progress in brain research*, vol. 196, pp. 1–28, 2012.

[54] D. S. Peterka, H. Takahashi, and R. Yuste, "Imaging voltage in neurons," *Neuron*, vol. 69, no. 1, pp. 9–21, 2011.

[55] E. W. Miller, "Small molecule fluorescent voltage indicators for studying membrane potential," *Current opinion in chemical biology*, vol. 33, pp. 74–80, 2016.

[56] J. E. Gonzalez and R. Y. Tsien, "Improved indicators of cell membrane potential that use fluorescence resonance energy transfer," *Chemistry & biology*, vol. 4, no. 4, pp. 269–277, 1997.

[57] K. D. Piatkevich, E. E. Jung, C. Straub, C. Linghu, D. Park, H.-J. Suk, D. R. Hochbaum, D. Goodwin, E. Pnevmatikakis, N. Pak, *et al.*, "A robotic multidimensional directed evolution approach applied to fluorescent voltage reporters," *Nature chemical biology*, vol. 14, no. 4, pp. 352–360, 2018.

[58] D. Smetters, A. Majewska, and R. Yuste, "Detecting action potentials in neuronal populations with calcium imaging," *Methods*, vol. 18, no. 2, pp. 215–221, 1999.

[59] R. Cossart, Y. Ikegaya, and R. Yuste, "Calcium imaging of cortical networks dynamics," *Cell calcium*, vol. 37, no. 5, pp. 451–457, 2005.

[60] W. Gobel and F. Helmchen, "In vivo calcium imaging of neural network function," *Physiology*, vol. 22, no. 6, pp. 358–365, 2007.

[61] C. Grienberger and A. Konnerth, "Imaging calcium in neurons," *Neuron*, vol. 73, no. 5, pp. 862–885, 2012.

[62] E. S. Boyden, F. Zhang, E. Bamberg, G. Nagel, and K. Deisseroth, "Millisecond-timescale, genetically targeted optical control of neural activity," *Nature neuroscience*, vol. 8, no. 9, pp. 1263–1268, 2005.

[63] K. Deisseroth, "Optogenetics," *Nature methods*, vol. 8, no. 1, pp. 26–29, 2011.

[64] S. C. Williams and K. Deisseroth, "Optogenetics," *Proceedings of the National Academy of Sciences*, vol. 110, no. 41, pp. 16287–16287, 2013.

[65] K. Deisseroth, "Controlling the brain with light," *Scientific American*, vol. 303, no. 5, pp. 48–55, 2010.

[66] V. A. Lórenz-Fonfría and J. Heberle, "Channelrhodopsin unchained: structure and mechanism of a light-gated cation channel," *Biochimica et Biophysica Acta (BBA)-Bioenergetics*, vol. 1837, no. 5, pp. 626–642, 2014.

[67] M. R. Warden, J. A. Cardin, and K. Deisseroth, "Optical neural interfaces," *Annual review of biomedical engineering*, vol. 16, pp. 103–129, 2014.

[68] A. Erofeev, E. Gerasimov, A. Lavrova, A. Bolshakova, E. Postnikov, I. Bezprozvanny, and O. L. Vlasova, "Light stimulation parameters determine neuron dynamic characteristics," *Applied Sciences*, vol. 9, no. 18, p. 3673, 2019.

[69] T. Ishizuka, M. Kakuda, R. Araki, and H. Yawo, "Kinetic evaluation of photosensitivity in genetically engineered neurons expressing green algae light-gated channels," *Neuroscience research*, vol. 54, no. 2, pp. 85–94, 2006.

[70] K. Nikolic, N. Grossman, M. S. Grubb, J. Burrone, C. Toumazou, and P. Degenaar, "Photocycles of channelrhodopsin-2," *Photochemistry and photobiology*, vol. 85, no. 1, pp. 400–411, 2009.

[71] C. Bamann, T. Kirsch, G. Nagel, and E. Bamberg, "Spectral characteristics of the photocycle of channelrhodopsin-2 and its implication for channel function," *Journal of molecular biology*, vol. 375, no. 3, pp. 686–694, 2008.

[72] P. Hegemann, S. Ehlenbeck, and D. Gradmann, "Multiple photocycles of channelrhodopsin," *Biophysical journal*, vol. 89, no. 6, pp. 3911–3918, 2005.

[73] N. Grossman, K. Nikolic, M. Grubb, J. Burrone, C. Toumazou, and P. Degenaar, "High-frequency limit of neural stimulation with chr2," in *2011 Annual International Conference of the IEEE Engineering in Medicine and Biology Society*, pp. 4167–4170, IEEE, 2011.

[74] S. Wäldchen, J. Lehmann, T. Klein, S. Van De Linde, and M. Sauer, "Light-induced cell damage in live-cell super-resolution microscopy," *Scientific reports*, vol. 5, no. 1, pp. 1–12, 2015.

[75] J.-Y. Tinevez, J. Dragavon, L. Baba-Aissa, P. Roux, E. Perret, A. Canivet, V. Galy, and S. Shorte, "A quantitative method for measuring phototoxicity of a live cell imaging microscope," *Methods in enzymology*, vol. 506, pp. 291–309, 2012.

[76] O. Yizhar, L. E. Fenno, T. J. Davidson, M. Mogri, and K. Deisseroth, "Optogenetics in neural systems," *Neuron*, vol. 71, no. 1, pp. 9–34, 2011.

[77] J. Y. Lin, "A user's guide to channelrhodopsin variants: features, limitations and future developments," *Experimental physiology*, vol. 96, no. 1, pp. 19–25, 2011.

[78] J. Y. Lin, P. M. Knutsen, A. Muller, D. Kleinfeld, and R. Y. Tsien, "Reachr: a red-shifted variant of channelrhodopsin enables deep transcranial optogenetic excitation," *Nature neuroscience*, vol. 16, no. 10, pp. 1499–1508, 2013.

[79] F. Zhang, M. Prigge, F. Beyrière, S. P. Tsunoda, J. Mattis, O. Yizhar, P. Hegemann, and K. Deisseroth, "Red-shifted optogenetic excitation: a tool for fast neural control derived from volvox carteri," *Nature neuroscience*, vol. 11, no. 6, pp. 631–633, 2008.

[80] N. C. Klapoetke, Y. Murata, S. S. Kim, S. R. Pulver, A. Birdsey-Benson, Y. K. Cho, T. K. Morimoto, A. S. Chuong, E. J. Carpenter, Z. Tian, *et al.*, "Independent optical excitation of distinct neural populations," *Nature methods*, vol. 11, no. 3, pp. 338–346, 2014.

[81] K. Oda, J. Vierock, S. Oishi, S. Rodriguez-Rozada, R. Taniguchi, K. Yamashita, J. S. Wiegert, T. Nishizawa, P. Hegemann, and O. Nureki, "Crys-

tal structure of the red light-activated channelrhodopsin chrimson," *Nature communications*, vol. 9, no. 1, pp. 1–11, 2018.

[82] T. Mager, D. L. de la Morena, V. Senn, J. Schlotte, K. Feldbauer, C. Wrobel, S. Jung, K. Bodensiek, V. Rankovic, L. Browne, *et al.*, "High frequency neural spiking and auditory signaling by ultrafast red-shifted optogenetics," *Nature communications*, vol. 9, no. 1, pp. 1–14, 2018.

[83] W. Afshar Saber, F. M. Gasparoli, M. G. Dirks, F. J. Gunn-Moore, and M. Antkowiak, "All-optical assay to study biological neural networks," *Frontiers in neuroscience*, vol. 12, p. 451, 2018.

[84] B. E. Maimon, K. Sparks, S. Srinivasan, A. N. Zorzos, and H. M. Herr, "Spectrally distinct channelrhodopsins for two-colour optogenetic peripheral nerve stimulation," *Nature biomedical engineering*, vol. 2, no. 7, pp. 485–496, 2018.

[85] A. M. Aravanis, L.-P. Wang, F. Zhang, L. A. Meltzer, M. Z. Mogri, M. B. Schneider, and K. Deisseroth, "An optical neural interface: in vivo control of rodent motor cortex with integrated fiberoptic and optogenetic technology," *Journal of neural engineering*, vol. 4, no. 3, p. S143, 2007.

[86] J. Wang, F. Wagner, M. Diagne, D. A. Borton, J. Zhang, I. Ozden, R. D. Burwell, A. V. Nurmikko, R. van Wagenen, I. Diester, *et al.*, "Corrigendum: Integrated device for combined optical neuromodulation and electrical recording for chronic in vivo applications (2012 j. neural eng. 9," *J. Neural Eng*, vol. 13, no. 039501, p. 039501, 2016.

[87] J. Zhang, F. Laiwalla, J. A. Kim, H. Urabe, R. Van Wagenen, Y.-K. Song, B. W. Connors, F. Zhang, K. Deisseroth, and A. V. Nurmikko, "Integrated device for optical stimulation and spatiotemporal electrical recording of neural activity in light-sensitized brain tissue," *Journal of neural engineering*, vol. 6, no. 5, p. 055007, 2009.

[88] F. Zhang, V. Gradinaru, A. R. Adamantidis, R. Durand, R. D. Airan, L. De Lecea, and K. Deisseroth, "Optogenetic interrogation of neural circuits: technology for probing mammalian brain structures," *Nature protocols*, vol. 5, no. 3, pp. 439–456, 2010.

[89] S. Dufour and Y. De Koninck, "Optrodes for combined optogenetics and electrophysiology in live animals," *Neurophotonics*, vol. 2, no. 3, p. 031205, 2015.

[90] J. A. Cardin, M. Carlén, K. Meletis, U. Knoblich, F. Zhang, K. Deisseroth, L.-H. Tsai, and C. I. Moore, "Targeted optogenetic stimulation and recording of neurons in vivo using cell-type-specific expression of channelrhodopsin-2," *Nature protocols*, vol. 5, no. 2, pp. 247–254, 2010.

[91] C. K. Kim, A. Adhikari, and K. Deisseroth, "Integration of optogenetics with complementary methodologies in systems neuroscience," *Nature Reviews Neuroscience*, vol. 18, no. 4, pp. 222–235, 2017.

[92] M. Welkenhuysen, L. Hoffman, Z. Luo, A. De Proft, C. Van den Haute, V. Baekelandt, Z. Debyser, G. Gielen, R. Puers, and D. Braeken, "An inte-

grated multi-electrode-optrode array for in vitro optogenetics," *Scientific reports*, vol. 6, no. 1, pp. 1–10, 2016.

[93] X. Zhang, F.-C. Yeh, H. Ju, Y. Jiang, G. F. W. Quan, and A. M. VanDongen, "Familiarity detection and memory consolidation in cortical assemblies," *Eneuro*, vol. 7, no. 3, 2020.

[94] S. A. Josselyn, S. Köhler, and P. W. Frankland, "Finding the engram," *Nature Reviews Neuroscience*, vol. 16, no. 9, pp. 521–534, 2015.

[95] R. W. Semon, *The mneme*. G. Allen & Unwin Limited, 1921.

[96] S. A. Josselyn and S. Tonegawa, "Memory engrams: Recalling the past and imagining the future," *Science*, vol. 367, no. 6473, 2020.

[97] D. O. Hebb, *The Organization of Behavior*. New York: Wiley and Sons, 1949.

[98] S. Tonegawa, M. D. Morrissey, and T. Kitamura, "The role of engram cells in the systems consolidation of memory," *Nature Reviews Neuroscience*, vol. 19, no. 8, pp. 485–498, 2018.

[99] M.-m. Poo, M. Pignatelli, T. J. Ryan, S. Tonegawa, T. Bonhoeffer, K. C. Martin, A. Rudenko, L.-H. Tsai, R. W. Tsien, G. Fishell, *et al.*, "What is memory? the present state of the engram," *BMC biology*, vol. 14, no. 1, pp. 1–18, 2016.

[100] M. Bergami, S. Santi, E. Formaggio, C. Cagnoli, C. Verderio, R. Blum, B. Berninger, M. Matteoli, and M. Canossa, "Uptake and recycling of pro-bdnf for transmitter-induced secretion by cortical astrocytes," *The Journal of cell biology*, vol. 183, no. 2, pp. 213–221, 2008.

[101] B. Vignoli, G. Battistini, R. Melani, R. Blum, S. Santi, N. Berardi, and M. Canossa, "Peri-synaptic glia recycles brain-derived neurotrophic factor for ltp stabilization and memory retention," *Neuron*, vol. 92, no. 4, pp. 873–887, 2016.

[102] F. Engert and T. Bonhoeffer, "Dendritic spine changes associated with hippocampal long-term synaptic plasticity," *Nature*, vol. 399, no. 6731, pp. 66–70, 1999.

[103] S.-H. Shi, Y. Hayashi, R. S. Petralia, S. H. Zaman, R. J. Wenthold, K. Svoboda, and R. Malinow, "Rapid spine delivery and redistribution of ampa receptors after synaptic nmda receptor activation," *Science*, vol. 284, no. 5421, pp. 1811–1816, 1999.

[104] M.-B. Moser, M. Trommald, and P. Andersen, "An increase in dendritic spine density on hippocampal ca1 pyramidal cells following spatial learning in adult rats suggests the formation of new synapses," *Proceedings of the National Academy of Sciences*, vol. 91, no. 26, pp. 12673–12675, 1994.

[105] Y. Yang, X.-b. Wang, M. Frerking, and Q. Zhou, "Spine expansion and stabilization associated with long-term potentiation," *Journal of Neuroscience*, vol. 28, no. 22, pp. 5740–5751, 2008.

[106] A. Govindarajan, R. J. Kelleher, and S. Tonegawa, "A clustered plasticity model of long-term memory engrams," *Nature Reviews Neuroscience*, vol. 7, no. 7, pp. 575–583, 2006.

[107] M. Mayford, S. A. Siegelbaum, and E. R. Kandel, "Synapses and memory storage," *Cold Spring Harbor perspectives in biology*, vol. 4, no. 6, p. a005751, 2012.

[108] M. Bosch and Y. Hayashi, "Structural plasticity of dendritic spines," *Current opinion in neurobiology*, vol. 22, no. 3, pp. 383–388, 2012.

[109] M. Matsuzaki, N. Honkura, G. C. Ellis-Davies, and H. Kasai, "Structural basis of long-term potentiation in single dendritic spines," *Nature*, vol. 429, no. 6993, pp. 761–766, 2004.

[110] M. E. Greenberg and E. B. Ziff, "Stimulation of 3t3 cells induces transcription of the c-fos proto-oncogene," *Nature*, vol. 311, no. 5985, pp. 433–438, 1984.

[111] S. Tonegawa, M. Pignatelli, D. S. Roy, and T. J. Ryan, "Memory engram storage and retrieval," *Current opinion in neurobiology*, vol. 35, pp. 101–109, 2015.

[112] L. G. Reijmers, B. L. Perkins, N. Matsuo, and M. Mayford, "Localization of a stable neural correlate of associative memory," *Science*, vol. 317, no. 5842, pp. 1230–1233, 2007.

[113] F. Zhang, L.-P. Wang, E. S. Boyden, and K. Deisseroth, "Channelrhodopsin-2 and optical control of excitable cells," *Nature methods*, vol. 3, no. 10, pp. 785–792, 2006.

[114] S. Nabavi, R. Fox, C. D. Proulx, J. Y. Lin, R. Y. Tsien, and R. Malinow, "Engineering a memory with ltd and ltp," *Nature*, vol. 511, no. 7509, pp. 348–352, 2014.

[115] T. J. Ryan, D. S. Roy, M. Pignatelli, A. Arons, and S. Tonegawa, "Engram cells retain memory under retrograde amnesia," *Science*, vol. 348, no. 6238, pp. 1007–1013, 2015.

[116] A. Hayashi-Takagi, S. Yagishita, M. Nakamura, F. Shirai, Y. I. Wu, A. L. Loshbaugh, B. Kuhlman, K. M. Hahn, and H. Kasai, "Labelling and optical erasure of synaptic memory traces in the motor cortex," *Nature*, vol. 525, no. 7569, pp. 333–338, 2015.

[117] T. J. Ryan, C. O. de San Luis, M. Pezzoli, and S. Sen, "Engram cell connectivity: an evolving substrate for information storage," *Current Opinion in Neurobiology*, vol. 67, pp. 215–227, 2021.

[118] F. Gobbo, L. Marchetti, A. Jacob, B. Pinto, N. Binini, F. P. Bisogni, C. Alia, S. Luin, M. Caleo, T. Fellin, *et al.*, "Activity-dependent expression of channelrhodopsin at neuronal synapses," *Nature communications*, vol. 8, no. 1, pp. 1–14, 2017.

[119] A. J. Silva, Y. Zhou, T. Rogerson, J. Shobe, and J. Balaji, "Molecular and cellular approaches to memory allocation in neural circuits," *Science*, vol. 326, no. 5951, pp. 391–395, 2009.

[120] A. Holtmaat and P. Caroni, "Functional and structural underpinnings of neuronal assembly formation in learning," *Nature neuroscience*, vol. 19, no. 12, pp. 1553–1562, 2016.

[121] R. Chéreau, L. E. Williams, T. Bawa, and A. Holtmaat, "Circuit mechanisms for cortical plasticity and learning," in *Seminars in Cell & Developmental Biology*, Elsevier, 2021.

[122] V. Nikolenko, B. O. Watson, R. Araya, A. Woodruff, D. S. Peterka, and R. Yuste, "Slm microscopy: scanless two-photon imaging and photostimulation using spatial light modulators," *Frontiers in neural circuits*, vol. 2, p. 5, 2008.

[123] N. Grossman, V. Poher, M. S. Grubb, G. T. Kennedy, K. Nikolic, B. McGovern, R. B. Palmini, Z. Gong, E. M. Drakakis, M. A. Neil, *et al.*, "Multi-site optical excitation using chr2 and micro-led array," *Journal of neural engineering*, vol. 7, no. 1, p. 016004, 2010.

[124] P. Zhu, O. Fajardo, J. Shum, Y.-P. Zhang Schärer, and R. W. Friedrich, "High-resolution optical control of spatiotemporal neuronal activity patterns in zebrafish using a digital micromirror device," *Nature protocols*, vol. 7, no. 7, pp. 1410–1425, 2012.

[125] A. Yakushenko, Z. Gong, V. Maybeck, B. Hofmann, E. Gu, M. D. Dawson, A. Offenhäusser, and B. Wolfrum, "On-chip optical stimulation and electrical recording from cells," *Journal of biomedical optics*, vol. 18, no. 11, p. 111402, 2013.

[126] F. Heer, S. Hafizovic, T. Ugniwenko, U. Frey, W. Franks, E. Perriard, J.-C. Perriard, A. Blau, C. Ziegler, and A. Hierlemann, "Single-chip microelectronic system to interface with living cells," *Biosensors and Bioelectronics*, vol. 22, no. 11, pp. 2546–2553, 2007.

[127] S. Hafizovic, F. Heer, T. Ugniwenko, U. Frey, A. Blau, C. Ziegler, and A. Hierlemann, "A cmos-based microelectrode array for interaction with neuronal cultures," *Journal of neuroscience methods*, vol. 164, no. 1, pp. 93–106, 2007.

[128] Y. Jimbo, N. Kasai, K. Torimitsu, T. Tateno, and H. P. Robinson, "A system for mea-based multisite stimulation," *IEEE transactions on biomedical engineering*, vol. 50, no. 2, pp. 241–248, 2003.

[129] S. M. Potter and T. B. DeMarse, "A new approach to neural cell culture for long-term studies," *Journal of neuroscience methods*, vol. 110, no. 1-2, pp. 17–24, 2001.

[130] F. O. Morin, Y. Takamura, and E. Tamiya, "Investigating neuronal activity with planar microelectrode arrays: achievements and new perspectives," *Journal of bioscience and bioengineering*, vol. 100, no. 2, pp. 131–143, 2005.

[131] D. A. Wagenaar, J. Pine, and S. M. Potter, "Effective parameters for stimulation of dissociated cultures using multi-electrode arrays," *Journal of neuroscience methods*, vol. 138, no. 1-2, pp. 27–37, 2004.

[132] Z. Gong, H. Zhang, E. Gu, C. Griffin, M. D. Dawson, V. Poher, G. Kennedy, P. French, and M. Neil, "Matrix-addressable micropixellated ingan light-emitting diodes with uniform emission and increased light output," *IEEE Transactions on Electron Devices*, vol. 54, no. 10, pp. 2650–2658, 2007.

[133] J. Day, J. Li, D. Lie, C. Bradford, J. Lin, and H. Jiang, "Full-scale self-emissive blue and green microdisplays based on gan micro-led arrays," in *Quantum Sensing and Nanophotonic Devices IX*, vol. 8268, p. 82681X, International Society for Optics and Photonics, 2012.

[134] R. G. Hunsperger, *Intergated Optics, Theory and Technology*. Springer, 2009, 6th ed.

[135] R. Scarmozzino, A. Gopinath, R. Pregla, and S. Helfert, "Numerical techniques for modeling guided-wave photonic devices," *IEEE Journal of Selected Topics in Quantum Electronics*, vol. 6, no. 1, pp. 150–162, 2000.

[136] P. Bienstman and R. Baets, "Optical modelling of photonic crystals and vcsels using eigenmode expansion and perfectly matched layers," *Optical and Quantum Electronics*, vol. 33, no. 4, pp. 327–341, 2001.

[137] J. Covey and R. T. Chen, "Efficient perfectly vertical fiber-to-chip grating coupler for silicon horizontal multiple slot waveguides," *Optics express*, vol. 21, no. 9, pp. 10886–10896, 2013.

[138] C. Zaccaria, M. Mancinelli, and L. Pavesi, "A fem enhanced transfer matrix method for optical grating design," *Journal of Lightwave Technology*, vol. 39, no. 11, pp. 3521–3530, 2021.

[139] P. Degenaar, N. Grossman, M. A. Memon, J. Burrone, M. Dawson, E. Drakakis, M. Neil, and K. Nikolic, "Optobionic vision—a new genetically enhanced light on retinal prosthesis," *Journal of neural engineering*, vol. 6, no. 3, p. 035007, 2009.

[140] G. Quaranta, G. Basset, O. J. Martin, and B. Gallinet, "Recent advances in resonant waveguide gratings," *Laser & Photonics Reviews*, vol. 12, no. 9, p. 1800017, 2018.

[141] M. McLamb, Y. Li, S. Park, M. Lata, and T. Hofmann, "Diffraction gratings for uniform light extraction from light guides," in *2019 IEEE 16th International Conference on Smart Cities: Improving Quality of Life Using ICT & IoT and AI (HONET-ICT)*, pp. 220–222, IEEE, 2019.

[142] I. Zielonka and P. Karasiński, "Planar waveguides with diffracion gratings (rewiev paper)," *Molecular and Quantum Acoustics*, vol. 22, pp. 293–302, 2001.

[143] E. Silberstein, P. Lalanne, J.-P. Hugonin, and Q. Cao, "Use of grating theories in integrated optics," *JOSA A*, vol. 18, no. 11, pp. 2865–2875, 2001.

[144] K. Khalid, M. Zafrullah, S. Bilal, and M. Mirza, "Simulation and analysis of gaussian apodized fiber bragg grating strain sensor," *Journal of Optical Technology*, vol. 79, no. 10, pp. 667–673, 2012.

[145] K. Yao, R. Unni, and Y. Zheng, "Intelligent nanophotonics: merging photonics and artificial intelligence at the nanoscale," *Nanophotonics*, vol. 8, no. 3, pp. 339–366, 2019.

[146] X. Chen, C. Li, C. K. Fung, S. M. Lo, and H. K. Tsang, "Apodized waveguide grating couplers for efficient coupling to optical fibers," *IEEE Photonics Technology Letters*, vol. 22, no. 15, pp. 1156–1158, 2010.

[147] A. Patri, X. Jia, M. Mohsin, S. Kéna-Cohen, and C. Caloz, "Compact grating coupler using asymmetric waveguide scatterers," in *Frontiers in Optics*, pp. JW4A–80, Optical Society of America, 2019.

[148] S. Nambiar, P. Sethi, and S. K. Selvaraja, "Grating-assisted fiber to chip coupling for soi photonic circuits," *Applied Sciences*, vol. 8, no. 7, p. 1142, 2018.

[149] Y. Tang, Z. Wang, L. Wosinski, U. Westergren, and S. He, "Highly efficient nonuniform grating coupler for silicon-on-insulator nanophotonic circuits," *Optics letters*, vol. 35, no. 8, pp. 1290–1292, 2010.

[150] D. Taillaert, F. Van Laere, M. Ayre, W. Bogaerts, D. Van Thourhout, P. Bienstman, and R. Baets, "Grating couplers for coupling between optical fibers and nanophotonic waveguides," *Japanese Journal of Applied Physics*, vol. 45, no. 8R, p. 6071, 2006.

[151] W. S. Zaoui, A. Kunze, W. Vogel, M. Berroth, J. Butschke, F. Letzkus, and J. Burghartz, "Bridging the gap between optical fibers and silicon photonic integrated circuits," *Optics express*, vol. 22, no. 2, pp. 1277–1286, 2014.

[152] D. Melati, Y. Grinberg, M. K. Dezfouli, S. Janz, P. Cheben, J. H. Schmid, A. Sánchez-Postigo, and D.-X. Xu, "Mapping the global design space of nanophotonic components using machine learning pattern recognition," *Nature communications*, vol. 10, no. 1, pp. 1–9, 2019.

[153] T. Grosges, A. Vial, and D. Barchiesi, "Models of near-field spectroscopic studies: comparison between finite-element and finite-difference methods," *Optics Express*, vol. 13, no. 21, pp. 8483–8497, 2005.

[154] J. Čtyrokỳ, S. Helfert, R. Pregla, P. Bienstman, R. Baets, R. De Ridder, R. Stoffer, G. Klaasse, J. Petráček, P. Lalanne, *et al.*, "Bragg waveguide grating as a 1d photonic band gap structure: Cost 268 modelling task," *Optical and Quantum Electronics*, vol. 34, no. 5, pp. 455–470, 2002.

[155] J. C. Bansal, P. K. Singh, and N. R. Pal, *Evolutionary and swarm intelligence algorithms*. Springer, 2019.

[156] Y. Ma, Y. Zhang, S. Yang, A. Novack, R. Ding, A. E.-J. Lim, G.-Q. Lo, T. Baehr-Jones, and M. Hochberg, "Ultralow loss single layer submicron silicon waveguide crossing for soi optical interconnect," *Optics express*, vol. 21, no. 24, pp. 29374–29382, 2013.

[157] T. Watanabe, M. Ayata, U. Koch, Y. Fedoryshyn, and J. Leuthold, "Perpendicular grating coupler based on a blazed antiback-reflection structure," *Journal of Lightwave Technology*, vol. 35, no. 21, pp. 4663–4669, 2017.

[158] B. E. Saleh and M. C. Teich, *Fundamentals of photonics*. john Wiley & sons, 2019.

[159] L. B. Soldano and E. C. Pennings, "Optical multi-mode interference devices based on self-imaging: principles and applications," *Journal of lightwave technology*, vol. 13, no. 4, pp. 615–627, 1995.

[160] R. M. Paredes, J. C. Etzler, L. T. Watts, W. Zheng, and J. D. Lechleiter, "Chemical calcium indicators," *Methods*, vol. 46, no. 3, pp. 143–151, 2008.

[161] I. Micu, A. Ridsdale, L. Zhang, J. Woulfe, J. McClintock, C. A. Brantner, S. B. Andrews, and P. K. Stys, "Real-time measurement of free ca 2+ changes in cns myelin by two-photon microscopy," *Nature medicine*, vol. 13, no. 7, pp. 874–879, 2007.

[162] L. E. García-Chacón, K. T. Nguyen, G. David, and E. F. Barrett, "Extrusion of ca2+ from mouse motor terminal mitochondria via a na+–ca2+ exchanger increases post-tetanic evoked release," *The Journal of physiology*, vol. 574, no. 3, pp. 663–675, 2006.

[163] S. BOLSOVER, O. IBRAHIM, N. O'LUANAIGH, H. WILLIAMS, and S. COCKCROFT, "Use of fluorescent ca2+ dyes with green fluorescent protein and its variants: problems and solutions," *Biochemical Journal*, vol. 356, no. 2, pp. 345–352, 2001.

[164] W. Wang, C. K. Kim, and A. Y. Ting, "Molecular tools for imaging and recording neuronal activity," *Nature chemical biology*, vol. 15, no. 2, pp. 101–110, 2019.

[165] F. Radstake, E. Raaijmakers, R. Luttge, S. Zinger, and J.-P. Frimat, "Calima: The semi-automated open-source calcium imaging analyzer," *Computer methods and programs in biomedicine*, vol. 179, p. 104991, 2019.

[166] Z. Sun and T. C. Südhof, "A simple ca2+-imaging approach to neural network analyses in cultured neurons," *Journal of Neuroscience Methods*, vol. 349, p. 109041, 2021.

[167] E. A. Mukamel, A. Nimmerjahn, and M. J. Schnitzer, "Automated analysis of cellular signals from large-scale calcium imaging data," *Neuron*, vol. 63, no. 6, pp. 747–760, 2009.

[168] A. E. Carpenter, T. R. Jones, M. R. Lamprecht, C. Clarke, I. H. Kang, O. Friman, D. A. Guertin, J. H. Chang, R. A. Lindquist, J. Moffat, *et al.*, "Cellprofiler: image analysis software for identifying and quantifying cell phenotypes," *Genome biology*, vol. 7, no. 10, pp. 1–11, 2006.

[169] M. R. Lamprecht, D. M. Sabatini, and A. E. Carpenter, "Cellprofiler™: free, versatile software for automated biological image analysis," *Biotechniques*, vol. 42, no. 1, pp. 71–75, 2007.

[170] T. P. Patel, K. Man, B. L. Firestein, and D. F. Meaney, "Automated quantification of neuronal networks and single-cell calcium dynamics using calcium imaging," *Journal of neuroscience methods*, vol. 243, pp. 26–38, 2015.

[171] C. A. Schneider, W. S. Rasband, and K. W. Eliceiri, "Nih image to imagej: 25 years of image analysis," *Nature methods*, vol. 9, no. 7, pp. 671–675, 2012.

[172] M. J. Jang and Y. Nam, "Neuroca: integrated framework for systematic analysis of spatiotemporal neuronal activity patterns from large-scale optical recording data," *Neurophotonics*, vol. 2, no. 3, p. 035003, 2015.

[173] P. Kaifosh, J. D. Zaremba, N. B. Danielson, and A. Losonczy, "Sima: Python software for analysis of dynamic fluorescence imaging data," *Frontiers in neuroinformatics*, vol. 8, p. 80, 2014.

[174] M. Rubinov and O. Sporns, "Complex network measures of brain connectivity: uses and interpretations," *Neuroimage*, vol. 52, no. 3, pp. 1059–1069, 2010.

[175] O. Steward and P. F. Worley, "Selective targeting of newly synthesized arc mrna to active synapses requires nmda receptor activation," *Neuron*, vol. 30, no. 1, pp. 227–240, 2001.

[176] N. C. Pégard, A. R. Mardinly, I. A. Oldenburg, S. Sridharan, L. Waller, and H. Adesnik, "Three-dimensional scanless holographic optogenetics with temporal focusing (3d-shot)," *Nature communications*, vol. 8, no. 1, pp. 1–14, 2017.